UNIVERSITY OF CALIFORNIA
RIVERSIDE

Magneto-Thermal Transport in Metal and Semiconductor Thin Film

A Dissertation submitted in partial satisfaction
of the requirements for the degree of

Doctor of Philosophy

in

Mechanical Engineering

by

Anand Katailiha

September 2020

Dissertation Committee:
Dr. Sandeep Kumar, Chairperson
Dr. Luat T. Vuong
Dr. Chen W. Li

The Dissertation of Anand Katailiha is approved:

Committee Chairperson

University of California, Riverside

Acknowledgement

I am forever grateful to my advisor, Dr. Sandeep Kumar, for supporting me through my journey towards the PhD degree. I am thankful to my colleagues with whom I collaborated on many exciting research projects. I am also thankful for the years of technical support from Dr. Ward P. Beyermann (Physics) and cleanroom staff at the Center for Nanoscale Science and Engineering, UCR.

This dissertation contains texts, data, and figures from the following published articles –

- **Anand Katailiha**, Paul C. Lou and Sandeep Kumar, "*Magneto Thermal Transport Behavior in Freestanding $Ni_{80}Fe_{20}$/Au Bilayer Thin Films*", Solid State Communications, 2020, 307, 113811.
- Paul C. Lou, **Anand Katailiha**, Ravindra G. Bhardwaj, Tonmoy Bhowmick, W. P. Beyermann, Roger K. Lake and Sandeep Kumar, "*Large Spin Hall Effect in Si at Room Temperature*", Physical Review B, 2020, 101, 094435.

ABSTRACT OF THE DISSERTATION

Magneto-Thermal Transport in Metal and Semiconductor Thin Film

by

Anand Katailiha

Doctor of Philosophy, Graduate Program in Mechanical Engineering
University of California, Riverside, September 2020
Dr. Sandeep Kumar, Chairperson

Spin polarization, when induced in a non-ferromagnetic material, can change the underlying material behavior especially if the spin diffusion length is of the same order as the sample dimension, for example thickness. We demonstrate thermal hysteretic behavior induced by spin polarization in $Ni_{80}Fe_{20}$ (10 nm)/Au (100 nm) bilayer freestanding sample. The thermal hysteresis behavior is uncovered using magneto thermal characterization based on self-heating 3ω (three omega) method. The third harmonic voltage shows diverging behavior and thermal hysteresis during cooling and heating of the sample under an applied magnetic field, which is attributed to the spin accumulation. We demonstrate that the spin accumulation and thermal hysteresis in Au occurs due to ferromagnetic proximity polarization from $Ni_{80}Fe_{20}$ layer. The observed hysteresis behavior is also attributed to freestanding thin film structure and absence of substrate effects leading to longer spin diffusion length. These results in Au thin films may provide scientific direction

to study spin dependent behavior in widely studied diamagnetic and paramagnetic materials. In addition, layered thin film structures of normal metals and ferromagnetic metals can be used to achieve magnetocaloric effect for magnetic refrigeration without using complex and rare earth magnetic materials.

Silicon (Si) is a prominent material for electronics but not a preferred one for spintronics due to its inefficiency in generation and detection of spin current large enough to be utilized for commercial device applications. The culprit is the weak spin-orbit coupling in Si. We present an experimental proof of crystallographic direction dependent spin polarization using strain gradient and spin-phonon coupling, and thermal spin current generation using spin-phonon interactions in Si thin films in spite of it having an insignificant intrinsic spin-orbit coupling. We find that strain gradient acts as an external switch that breaks the symmetry of spin relaxation behavior and modify the spin-phonon interactions. The spin-phonon interactions lead to a phonon-driven redistribution of spin potential and spin current. The phonon-driven spin current gives rise to a phononic spin-Nernst effect in Si due to interlayer coupling with $Ni_{80}Fe_{20}$ thin film. The coefficient of spin-Nernst magneto-thermopower of the Si (45.4 μV/K) is estimated to be an order of magnitude larger than heavy metals such as tungsten (W). The primary heat carrier in Si are phonons and resulting spin-Nernst effect is expected to arise due to spin dependent electron-phonon scattering, which is also supported by spin-Hall magnetoresistance and Hall resistance measurement. Observation of phononic spin-Nernst effect puts a spotlight back on Si for spintronics and spin caloritronics applications.

Contents

List of Figures ix

List of Tables xv

Chapter 1 Introduction 1

1.1 Spin Injection 2

1.2 Spin Hall Effect 4

1.3 Spin Hall Magnetoresistance 6

1.4 Planar Nernst Effect 7

1.5 Spin Nernst Effect 16

1.6 Aim and Objectives 24

Chapter 2 Magneto-thermal transport behavior in freestanding $Ni_{80}Fe_{20}$/Au bilayer thin films 26

2.1 Introduction 26

2.2 Method 27

2.3 Results 35

2.4 Discussion 40

2.5 Conclusion 47

Chapter 3 Crystallographic Direction Dependent Spin Polarization in Silicon 48

3.1 Introduction 48

3.2 Method 49

3.3 Result 53

3.4 Discussion 60

3.5 Conclusion 61

Chapter 4 Spin Nernst Effect in Silicon 63

4.1 Introduction 63

4.2 Method 64

4.3 Results 69

4.4 Discussion 86

4.5 Conclusion 87
Chapter 5 Spin Phonon Coupling in Silicon 89
Chapter 6 Summary & Future Work 96
6.1 Summary 96
6.2 Future Work 98
References 100

List of Figures

Figure 1.1. (a) Schematic of non-local spin injection in a FM/NM/FM metallic system, and (b) up spin and down spin electrochemical potential combines to produce voltage at parallel (V_P) and antiparallel (V_{AP}) state. The spin degeneracy in NM layer comes from the spin proximity effect due to the FM metal in contact with it (not shown). Image taken from Y. Niimi et al [22]. 4

Figure 1.2. Band diagram of F and N at the F/N/F interface showing the split in degeneracy in N and detection of the diffused spins in N as function of orientation of detector F. Image taken from Y. Niimi et al [22]. 4

Figure 1.3. Principles of (a) SHE and (b) ISHE by Y. Niimi et al [22]. 6

Figure 1.4. Schematic representation of SMR measurement in F/N bilayer structure when the magnetization 'M' of the F layer is oriented (a) parallel and (b) orthogonal to the spin polarization vector at the F/N interface. Image taken from H. Nakayama et al [27]..... 7

Figure 1.5. Schematic for various thermomagnetic effects in thin ferromagnetic conductor. 9

Figure 1.6. Schematic of AMR theory used to derive PNE equation. 11

Figure 1.7. Hall bar setup for PNE measurement. Image taken from Y. Pu et al [36]. 14

Figure 1.8. PNE measurement setup from Py/Pt bilayer thin film structure. Image taken from D. Meier et al [37]. 15

Figure 1.9. Setup for PNE measurement using Si-N thermal isolation platform. Image taken from A. D. Avery et al [34]..... 16

Figure 1.10. Schematic of the Spin Nernst effect where ∇T is the applied thermal gradient and j_S is the transverse spin current generated. 17

Figure 1.11. The SNMR method. $J_{S,T}$ is the thermally generated current in HM due to ΔT_x; J_S^{ref} and J_S^{abs} are reflected and absorbed spin current from and in to FM layer, respectively. J_S^{ref} is contributing to longitudinal (ΔV_{xx}) via ISHE. Image taken from D. J. Kim et al [44]. 18

Figure 1.12. Experimental setup for SNE measurement using an isolated heater. Image taken from S. Meyer et al [46]. 22

Figure 1.13. Schematic of SNE measurement in CoFeB/W(Pt) bilayer structure with laser heating source for generation of thermal gradient. Image taken from D. J. Kim et al [44]. 23

Figure 2.1. Fabrication process of four-terminal freestanding Pd/$Ni_{80}Fe_{20}$/Au/Cr device. 30

Figure 2.2. The scanning electron micrograph showing the experimental setup with freestanding sample having Pd (1 nm)/$Ni_{80}Fe_{20}$ (10 nm)/Au (100 nm)/Cr (10 nm). Scale bar is 100 μm. 34

Figure 2.3. Schematic showing the non-local spin injection and spin-Hall effect, which will lead to spin accumulation in Au thin film; J_C is charge current, J_S is spin current and λSD is spin diffusion length of Au. 34

Figure 2.4. The $V_{3\omega}$ response as a function of heating current showing cubic relationship. 35

Figure 2.5. (a) MR at 300 K, and (b) the $V_{3\omega}$ response as a function of magnetic field (z-direction) at 300 K. Arrows in (a) & (b) indicate the direction of field sweep. 36

Figure 2.6. (a) resistance and (b) the $V_{3\omega}$ response as a function of temperature between 300 K and 5 K at 0.3 K/min and 5 mA of heating current applied across the sample and zero applied magnetic field showing hysteresis in cooling and heating thermal cycle attributed to the thermal drift. 37

Figure 2.7. (a) The resistance and (b) the $V_{3\omega}$ response as a function of temperature between 300 K and 50 K at 0.3 K/min and 3 mA of heating current and applied magnetic field of 1T along z-axis. 38

Figure 2.8. (a) the $V_{3\omega}$ response as a function of temperature cycled between 300 K and 200 K at applied magnetic field of 1 T (black) for 12 cycles, 2 T (red) for 4 cycles and 0.5 T (blue) for 4 cycles, and (b) The resistance as a function of temperature cycled between 300 K and 200 K showing the thermal drift for 20 cycles between 300 K and 200 K. Resistance values during cooling and heating are same during thermal cycling indicating absence of thermal hysteresis. Temperature sweep rate: 1 K/min for (a) & (b). 40

Figure 2.9. (a) The resistance and (b) voltage response when the temperature is swept, from 400 K to 10 K to 150 K to 50 K to 400 K, at 0.2 K/min and 4.5 mA of heating current applied across the sample and zero applied magnetic field showing hysteresis in repeated cooling and heating thermal cycle attributed to the thermal drift. 42

Figure 2.10. (a) The resistance, and (b) voltage response when the temperature is swept, from 400 K to 10 K and back at 0.4 K/min and 10 μA of heating current applied across the sample and no applied magnetic field. 42

Figure 2.11. Magnetic domains in $Ni_{80}Fe_{20}$ thin film (a) when no magnetic field is applied resulting in randomized intrinsic moment in individual domains, and (b) when large magnetic field is applied which aligns the spins in all the domains along its direction. .. 43

Figure 2.12. Angle dependent magneto resistance (ADMR) or spin Hall magneto resistance (SMR) responses of the $Ni_{80}Fe_{20}$/Au device at 1 T and at (a) 300 K showing no SMR response, and (b) 25 K showing weak SMR response. 45

Figure 2.13. The measurement of resistance (Ω, black) and $V_{3\omega}$ (μV, red) response as a function of temperature from 300 K to 50 K showing a bump in $V_{3\omega}$ response at ~240 K. 46

Figure 2.14. Schematic showing the mechanism of ferromagnetic proximity polarization and spin accumulation at the Ni80Fe20/Au bilayer interface. 47

Figure 3.1. Flexoelectric charge polarization in a crystal due to strain gradient. 49

Figure 3.2. Orientation of the crystallography devices on silicon (100) wafer with 0˚ device aligned along <110> direction followed by devices oriented 15˚, 30˚ and 45˚ w.r.t <110>. 50

Figure 3.3. Fabrication procedure of SOI wafer device for crystallography experiment. 51

Figure 3.4. Device schematic and experimental setup for crystallographic direction dependent measurements in the yz-plane. The strain gradient due to thermal expansion and buckling and the resulting strain gradient from them is also shown. C denotes compression and T denotes tension. 52

Figure 3.5. The buckling of Si beam due to residual stresses. 54

Figure 3.6. (a) High resolution transmission electron micrograph showing the thin film structure at the Si interface and the estimated strain in <110> direction, and (b) The intensity profile along <110> direction used to identify the strain. 55

Figure 3.7. The EDS elemental mapping showing (a) the elemental distribution of Si, O, Ni, Fe and C across the $Ni_{80}Fe_{20}$/MgO/p-Si heterostructure, and (b) elemental distribution of Ni. The C layer is used for protection during FIB sample preparation. 55

Figure 3.8. Band structure of Si (a) for 4% tensile strain applied along <100> and inset showing the energy splitting at the peak of valence band, and (b) for 4% compressive strain applied along <100>. 56

Figure 3.9. The band structure of Si for (a) 4% tensile strain applied along <110>. Inset showing the energy splitting at the peak of valence band, (b) 4% compressive strain along <110>, (b) the valence band maxima at 4% compressive strain along <110> direction.. 57

Figure 3.10. Band structure of Si under 2% applied compressive strain along <100>. ... 57

Figure 3.11. The magnetoresistance for an applied out of plane magnetic field for current applied (a) along <110> direction or along the flat of the Si (100) wafer, (b) at 15^{o} to the <110> direction, (c) at 30^{o} to the <110> direction and (d) along <100> direction. Arrows showing saturation magnetization and possible canted states and its transition as a function of orientation. 59

Figure 3.12. The magneto-thermal transport characterization of p-Si thin film sample. (a) a representative scanning electron microscope image showing the schematic of experimental setup for SNE measurement and the angle dependent magneto thermal transport measurement in *yx*-plane for an applied magnetic field of 1 T at Hall junctions (b) J2, (c) J3 and (d) J4 showing SNE, PNE and SNE responses respectively. Red line is curve fit. 62

Figure 4.1. Scheme of the hypothesis showing the spin-Nernst effect behavior due to spin-phonon interactions for the temperature gradient along *x*-axis. 64

Figure 4.2. Fabrication procedure of SOI hall bar device for SNE experiment. 67

Figure 4.3. (a) & (b) SEM micrographs that proves the existence of a freestanding device structure. Scale bar is 2 μm in (a). 68

Figure 4.4. A representative scanning electron microscope image showing the structure of the experimental device, its dimensions, and experimental scheme. Scale bar is 20 μm. 68

Figure 4.5. The schematic of angle-dependent magneto-thermal transport characterization. (a) Schematic showing the heating (I) junction J1 and measurement ($V2\omega$) at junctions J2, J3 and J4. (b) Schematic showing the heating junction J4 and measurement at junctions J1, J2 and J3. 69

Figure 4.6. The angle-dependent magneto-thermal transport measurement and the line fit (red) at junctions J2, J3 and J4 in the yx-plane at an applied magnetic field of 1 T when junction J1 is heated, giving rise to $+\nabla \mathrm{T}x$. 71

Figure 4.7. The angle-dependent magneto-thermal transport measurement and the line fit (red) at junctions J1, J2 and J3 in the yx-plane at an applied magnetic field of 1 T when junction J4 is heated, giving rise to $-\nabla T_x$. 71

Figure 4.8. The net angle-dependent transverse $V2\omega$ response arising from the in $Ni_{80}Fe_{20}$(25 nm)/MgO (1.8 nm)/ SiO_2 (native)/p-Si (2 μm) sample in the yx-plane at an applied magnetic field of 1 T (a) when junction J1 is heated and (b) when junction J4 is heated. 72

Figure 4.9. The angle dependent transverse thermal response behavior in $Ni_{80}Fe_{20}$ (25 nm)/SiO_2 (25 nm)/p-Si (2 μm) control sample showing the PNE behavior when heating the J1 junction and response measurement at J2 and J3. 72

Figure 4.10. The angle dependent transverse thermal response behavior in $Ni_{80}Fe_{20}$ (25 nm)/SiO_2 (25 nm)/p-Si (2 μm) control sample showing the PNE behavior when heating the J1 junction and response measurement at J2 and J3. 73

Figure 4.11. The angle dependent transverse thermal response behavior in 2 μm p-Si control sample showing the ordinary Nernst effect behavior when J3 was heated and response was measured at J2..... 73

Figure 4.12. (a) The expected temperature distribution across the length of the specimen estimated using COMSOL simulation at 2 mA of current and (b) longitudinal temperature profile for an applied heating current of 2 mA. 76

Figure 4.13. The infra-red thermal imaging microscope image showing the temperature profile (a) for 2 mA of longitudinal current in the p-Si hall bar sample, and (b) 2 mA of longitudinal current in a $Ni_{80}Fe_{20}$ (25 nm)/MgO (1.8 nm)/p-Si (2 μm) composite sample. 76

Figure 4.14. (a) The angle dependent longitudinal magneto-thermopower response in yx-plane at 1 T, 4 T and 8 T in the composite p-Si sample for junctions (a) J2, (b) J3, (c) J23, and (d) J34..... 78

Figure 4.15. Hall effect measurement w.r.t applied out of plane magnetic field and as a function of applied current having a magnitude of 0.5 mA, 5 mA and 10 mA. 80

Figure 4.16. Hall effect measurement w.r.t applied out of plane magnetic field for junctions J2 and J3. Inside showing the schematic of longitudinal spin gradient. 81

Figure 4.17. For Pd(1 nm)/$Ni_{80}Fe_{20}$ (25 nm)/MgO(1.8 nm)/SiO_2 (native)/p-Si (2 μm) composite sample the in-plane thermal conductivity measured using self-heating 3ω-method as a function of out of plane magnetic field of 3 T to -3. 83

Figure 4.18. For Pd(1 nm)/$Ni_{80}Fe_{20}$ (25 nm)/MgO(1.8 nm)/SiO_2 (native)/p-Si (2 μm) composite sample (a) the angular dependence of resistance for an applied magnetic field of 4T in out of plane showing spin-Hall magnetoresistance behavior, where red line is data fit, and (b) The out of plane anisotropic magnetoresistance (AMR) in 25 nm Ni80Fe20 thin film measured by angular rotation in zy-plane which is opposite to the symmetry of SMR in (a). 84

Figure 4.19. Non-local (R_{nl}) and longitudinal (R_{xx}) resistance measurement as a function of temperature (a) in p-Si (2 μm) and (b) in MgO (10 nm)/p-Si (μm) samples. Schematic of non-local and longitudinal resistance measurement setup in (a). 85

Figure 5.1. (a) Angle dependent magnetoresistance modulation in yz plane at 300K in Pt/p-Si sample, (b) diamond cubic crystal structure of Si showing the hidden spin polarization. 92

Figure 5.2. Angle dependent longitudinal resistance in Py/p-Si sample showing the AMR and GMR behavior, (b) Crystallographic ADMR modulation of the Py/p-Si sample..... 93

Figure 5.3. Optical image showing two device structure corresponding to sample orientation along <110> and <100> direction in p-Si layer for Py/p-Si. 94

Figure 5.4. For Py/p-Si sample: crystallographic direction dependent (a) magnetoresistance and (b) longitudinal V2ω response as a function of out of plane magnetic field for a current applied along <110> direction and <100> direction of the p-Si layer. (c) & (d) <111> cross sectional planes for [110] & [100] directions, respectively. $d\epsilon/dz$ is the strain gradient.95

List of Tables

Table 4.1. The magnitude of the angular modulation in the transverse $V2\omega$ response for direction-dependent thermal transport and the resulting symmetry behavior of the $V2\omega$ 74

Table 4.2. The anomalous Hall resistance and Hall coefficients for up-spin and down-spin charge carrier in the composite p-Si sample as a function of current. 80

Table 4.3. The Hall slope, resistance and carrier concentration estimated for positive and negative magnetic fields at junctions J2 and J3. 82

Chapter 1 Introduction

Free electrons and other elementary particles possess an intrinsic angular momentum called spin [1]. It is of two types: $+\frac{1}{2}$ (or 'up') spin and $-\frac{1}{2}$ (or 'down') spin. From the reason behind splitting of spectral lines to a phenomenon called giant magneto resistance (GMR) effect [2, 3], spin, especially of electrons, has played a tremendous role over last century in developing science and technology. One such example is Spintronics where the information, that is transferred by the charge (or charge current) of the electron in traditional electronics, is replaced by its spin (or spin current, which is a flow of unequal number of up and down spins). This has proved to be an efficient substitute for the limitation of electronics technology researchers of today know. Although spintronics is at nascent stage, its promise to solve current technological challenges is overwhelming. For instance, one wide application of spintronics technology that is currently being used is in the read/write heads of the hard drives [4] or other memory devices which enabled storing digital data in a smaller area and manipulating it at much faster and efficient way. Other applications are spin based logic devices, spin hall effect transistor, magnetic field sensor, magneto resistive random-access memory etc. [5, 6]

Spin caloritronics [7-12], a subset of spintronics which arises from the magneto-thermal interaction of spintronics and thermoelectricity, is the study of electron's spin coupled with heat currents and the resulting effects from it for device applications. Spin transport across interfaces between ferromagnetic (FM) and non-magnetic (NM) materials is of particular interest for spin caloritronics applications as the interface between them

breaks the symmetry of the lattice, giving rise to interesting new phenomena such as thermally induced spin injection [13], non-local spin accumulation, interfacial Rashba effect [14-16] etc. The field of spin caloritronics is significant in advancing technologies mainly due to the reason that thermal excitation can produce extreme spin flow. Dedicated research into spin caloritronics began with the observation of the spin-Seebeck effect in 2008 [17] followed by many other important discoveries.

1.1 Spin Injection

In recent years, electrical spin injection and detection has grown into a lively area of research in the field of spintronics. Spin injection into a paramagnetic material is usually achieved by means of a ferromagnetic source, whereas the induced spin accumulation or associated spin currents are detected by means of a second ferromagnet or the reciprocal spin Hall effect [18]. The study of spin transport across interface of FM/NM metals is of particular importance because the spin accumulation and injection in to the NM metal could open a wide array of possibilities [13]. One such outcome would be to induce change in properties of a NM material at the microscopic level [19, 20], thus turning a NM material into a transient magnetic material. This could open a variety of applications such as magnetic refrigeration and magnetic cooling applications without any use of complex or rare earth magnetic materials, as well as spin-based logic and/or memory devices.

Pure spin current consists of only spin whereas a spin polarized current consists of both charge and spin. Spin injection is a method to inject spins into non-magnetic metals from a ferromagnet attached to it which is then subsequently measured by another ferromagnet which is also attached to it. One of the first implementation of spin injection

was the GMR effect. After that spin injection was used as the central mechanism for tunnel magnetoresistance (TMR), spin-orbit torque (SOT) for spin-based memory applications etc. One method to generate pure spin current in NM metal via a FM/NM metal interface is the non-local spin injection [13, 21, 22]. Figure 1.1 (a) shows the schematic of non-local spin injection in a lateral spin valve geometry comprising of F/ N/ F metal system where the first F metal is the injector and the second one is the detector with a N metal, having weak spin orbit coupling, connecting the two [22]. When a current I_C is applied through F (injector) and N, as shown in Figure 1.1 (a), spin accumulation builds up at the first F/N interface in order to have up-spin and down-spin chemical potentials to stay continuous due to ohmic nature of the contacts. This causes a split in degeneracy in the N as shown in Figure 1.2. The difference in the spin-dependent chemical potential is known as spin accumulation and is given by $\delta\mu$ as shown in Figure 1.1 (b). Due to proximity effect the accumulated spins diffuse into the NM, thus the pure spin current I_S flows ~1 μm to the other side of the N and decays over characteristic length called as spin diffusion length λ_N [Figures 1.1 (a) and (b)]. The spins can be detected using F (detector) oriented either parallel or antiparallel to its magnetization direction and given by distinct voltage signal ΔV_S. Similarly, spin injection into a paramagnetic material can also be achieved by means of a ferromagnetic source.

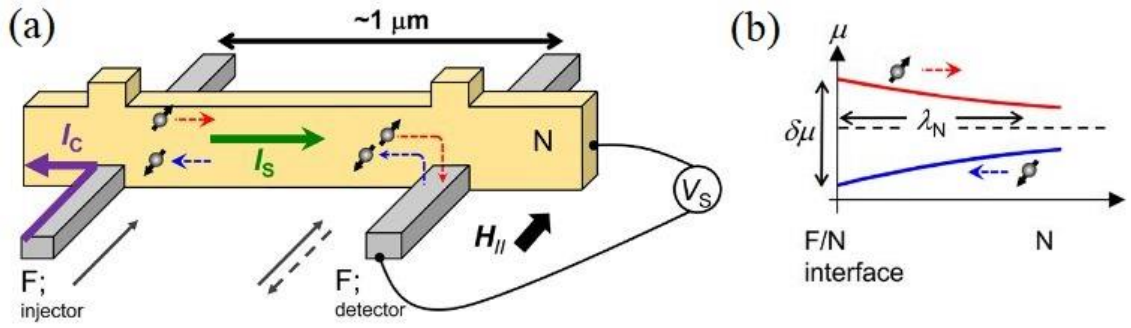

Figure 1.1. (a) Schematic of non-local spin injection in a FM/NM/FM metallic system, and (b) up spin and down spin electrochemical potential combines to produce voltage at parallel (V_P) and antiparallel (V_{AP}) state. The spin degeneracy in NM layer comes from the spin proximity effect due to the FM metal in contact with it (not shown). Image taken from Y. Niimi et al [22].

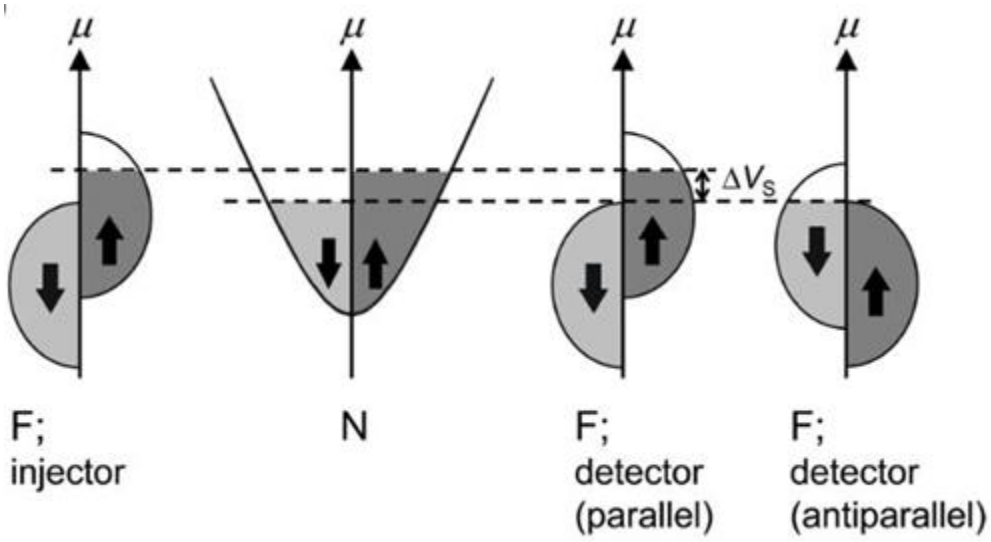

Figure 1.2. Band diagram of F and N at the F/N/F interface showing the split in degeneracy in N and detection of the diffused spins in N as function of orientation of detector F. Image taken from Y. Niimi et al [22].

1.2 Spin Hall Effect

Spintronics is considered to be an energy efficient alternative to modern electronics. To realize spintronics devices, spin current with large spin polarization needs to be achieved. One well-known way of generating and detecting spin current is the spin Hall

effects (SHE) [23-25]. SHE is the spin analogous to the Hall effect, which was discovered in 1879 by Edwin Hall. In a conductor when a current and magnetic field are applied orthogonal to each other, an electric field is induced in the conductor transverse to the direction of applied current. This is Hall effect. Edwin Hall later discovered what is called as the anomalous Hall effect (AHE) where current applied along the length of a ferromagnetic conductor will induce transverse current which is spin polarized. Later it was found that it deflects majority and minority spin electrons to either side of the conductor. SHE is very similar to AHE. In SHE, when a charge current (I_C) is passed through a non-magnetic conductor that has high spin orbit coupling, an asymmetric deflection of the electrons is occurred in the transverse direction depending on their spin orientation [22] (Figure 1.2a) creating a spin field, and therefore a spin current (I_S). SHE was first predicted by Dyakonov and Perel in 1971 [23]. Greater the magnitude of spin orbit coupling in the material, greater is the generation of spin current because of the SHE. The inverse of SHE, called inverse spin Hall effect (ISHE), is the conversion of the spin current into a measurable charge current by the same principle and method and creating potential field transverse to the spin flux (Figure 1.2b) [22, 24]. Spin Hall effects are denoted mathematically by

$$I_S = \theta_{SHE}.I_C \times S \tag{1.1}$$

$$I_C = \theta_{ISHE}.I_S \times S \tag{1.2}$$

where I_S is spin current, I_C is charge current, S is spin polarization vector and $\theta_{SHE/ISHE}$ is the spin-Hall angle, which is a measure of conversion efficiency between spin and charge currents and is defined as the ratio of spin conductivity to charge conductivity ($\theta_{SH} = \sigma_S/\sigma_C$).

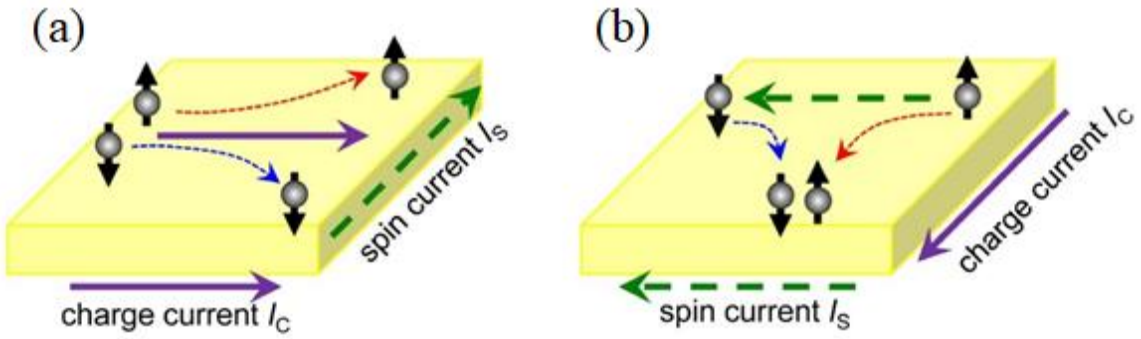

Figure 1.3. Principles of (a) SHE and (b) ISHE by Y. Niimi et al [22].

1.3 Spin Hall Magnetoresistance

One of the widely accepted way of characterizing spin current is the spin hall magneto resistance (SMR) [26, 27]. The SMR arises due to resistance modulation from spin current being reflected or absorbed at the ferromagnetic/non-magnetic interface under the angular rotation of applied magnetic field. When a longitudinal current J_e' is passed in a normal metal (N)/ferromagnet insulator (F) bilayer, spin polarization at the F/N interface occurs due to the spin Hall effect as shown in Figure 1.3 (a) [27]. This causes a net transverse spin flow J_S. With the help of external magnetic field, when the magnetization (M) of the FMI is oriented parallel or antiparallel to the spin polarization (M||σ) at the FMI/NM interface, spins will get reflected back (J_S^{back}) to the NM which will then convert back to charge current due to ISHE as shown in Figure 1.3 (a) resulting in very little spin current (J_S^{abs}) actually reach the ferromagnet layer. But when M is oriented perpendicular to the spin polarization (M⊥σ), it will get absorbed by the FMI via spin transfer torque and the resistance of the bilayer will increase thus causing resistance modulation.

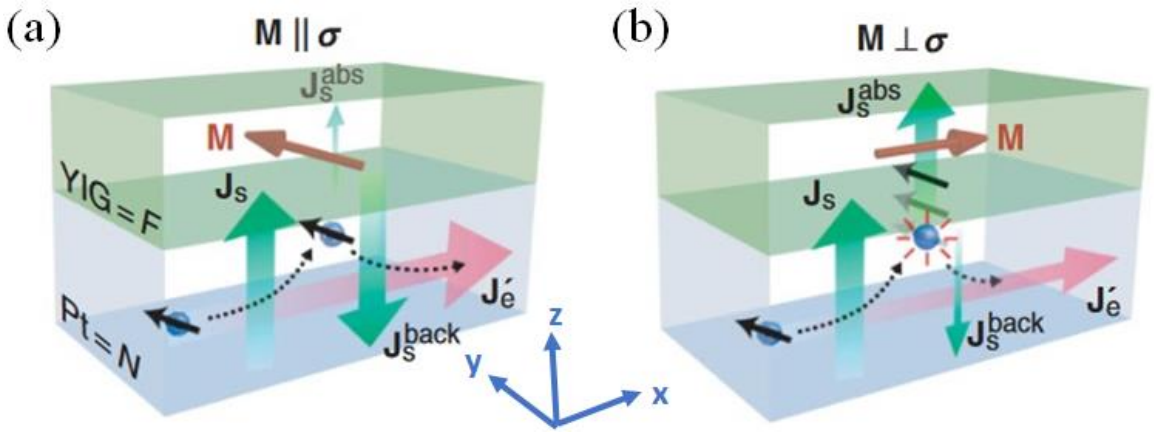

Figure 1.4. Schematic representation of SMR measurement in F/N bilayer structure when the magnetization 'M' of the F layer is oriented (a) parallel and (b) orthogonal to the spin polarization vector at the F/N interface. Image taken from H. Nakayama et al [27].

1.4 Planar Nernst Effect

Analogous to electrically induced spin current, thermally induced spin current generation and its detection have also attracted a lot of interest in spintronics application and is conveniently termed as spin caloritronics, which is the field of science that investigates coupling of spin and heat and observation of the resulting thermomagnetic effects. Thermomagnetic effects are produced when the electric and thermal properties of conductors and semiconductors are influenced by an external field under temperature gradients. The applied field acts upon the moving charge carriers (electrons in conductors whereas electron/holes in semiconductors) and their associated heat flux by modifying its path through the material. As a result, perpendicular components of the electric current and heat flux appear with respect to the applied magnetic field. To define thermomagnetic effects a simple relation is drawn between the magnetic field intensity or magnetization, and the temperature gradient. This relation depends on the direction vector along which the measurement is made. Thermomagnetic effects can be measured parallel or perpendicular

to the applied temperature gradient and is dubbed as longitudinal and transverse effects, respectively. One example of a thermomagnetic effect is the Nernst-Ettingshausen effect where an electric field E is generated in a semiconductor or metal conductor if it has a temperature gradient and a superimposed magnetic field perpendicular to it. The induced field has both longitudinal and transverse components. The Righi-Leduc effect, Anomalous Nernst-Ettingshausen effect etc. are also examples of thermomagnetic effects.

When a thin ferromagnetic metal film, for example – $Ni_{80}Fe_{20}$, is subjected to an applied thermal gradient, spin Seebeck effect (SSE) [17] can occur where an in-plane temperature gradient, ∇T_x, generates a spin current which can be detected as an electromotive force, $\vec{E}_{ISHE} = \theta_{ISHE}\,\vec{J}_S \times \vec{s}$, via the ISHE using a material with high spin orbit coupling (such as Pt) attached to it as shown in Figure 1.4. Here, $\vec{E}_{ISHE}$ is acting orthogonal to the spin current $\vec{J}_S$ and the spin polarization vector $\vec{s}$, which depends on magnetization of FM material and is aligned to the external magnetic field. θ_{ISHE} is the inverse spin hall coefficient which tells about the efficiency of spin current to charge current conversion. SSE is believed to be magnon driven in magnetic [28, 29] and phonon mediated in non-magnetic [30] materials. The $\vec{E}_{ISHE}$ signal will be proportional to the difference in temperature across the sample and will change its sign depending on the Pt position from the hot to the cold side of the FM film. The sign change can also be observed by changing the direction of applied magnetic field due to $\vec{J}_S \times \vec{s}$. This leads to a $\cos\theta$ symmetry of the $\vec{E}_{ISHE}$ voltage, where θ is the angle between the in plane magnetic field and the x-direction as depicted in Figure 1.4.

The spin current $\vec{J}_S$ travels perpendicular to the in plane thermal gradient and into the Pt film and converts to a transverse voltage. This configuration is known as transverse SSE (t-SSE) [30, 31]. In contrast, an applied out of plane temperature gradient (∇T_z) (Figure 1.4) will have spin current flow parallel to it and into Pt. This configuration is known as longitudinal SSE (l-SSE) [32, 33]. The ISHE voltage from t-SSE and l-SSE configurations may be influenced by parasitic effects such as anomalous Nernst effect (ANE), where an out of plane magnetic field in conjunction with the in plane magnetic field will produce transverse voltage which perpendicular to both, $\vec{E}_{ANE} = \delta_{ANE}\, \nabla T \times \vec{M}$. Hence, $\vec{E}_{ANE}$ is the cross product of thermal gradient and magnetization of FM material and acts in the direction perpendicular to both. δ_{ANE} is the ANE coefficient. The $\vec{E}_{ANE}$ is proportional to the temperature gradient and its sign changes with magnetization under large magnetic field and a $\cos\theta$ symmetry can be observed through the rotation of an in-plane magnetic field, where θ is the angle between $\vec{M}$ and ∇T_x. The symmetry of SSE and ANE cause difficulty in distinguishing between them from the measured transverse voltage.

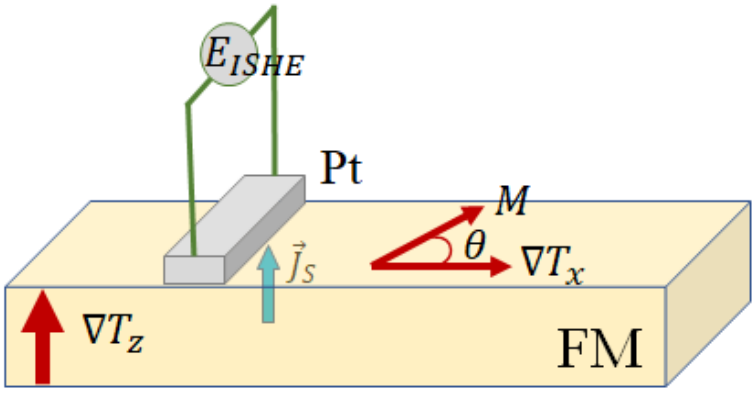

Figure 1.5. Schematic for various thermomagnetic effects in thin ferromagnetic conductor.

Apart from SSE and ANE, planar Nernst effect (PNE) [34-40] can be observed in a conducting FM film by an in-plane temperature gradient. PNE is a thermal counterpart of the planar Hall effect (PHE) in ferromagnetic metals. PNE occurs because of spin-dependent scattering of charge carriers creating a transverse response. According to PNE (Figure 1.4), when a temperature gradient (∇T_x) is applied, a voltage in the transverse direction is induced which is dependent on the direction of the in plane magnetization ($\vec{M}$) of the ferromagnetic metal with respect to ∇T_x. The equation for the PNE can be derived from the anisotropic magneto resistance (AMR) theory [39] since the mechanism of both the phenomena comes from the same origin: spin orbit coupling. According to AMR, resistance across a ferromagnetic conductor is high (low) when the applied current is parallel (perpendicular) to the saturated magnetization direction. In a ferromagnetic conductor longitudinal electric field E_x, due to longitudinal current $|\vec{J_x}| = J_x$, will depend on its parallel ($E_\parallel$) and perpendicular ($E_\perp$) components with respect to the magnetization direction $\vec{M}$ as shown in Figure 1.5. These components are given by the multiplication of current J_x, the resistivity ρ along the components and the angle θ between $\vec{M}$ and J_x [39].

$$E_\perp = J_x \, \rho_\perp \sin\theta \tag{1.3}$$

$$E_\parallel = J_x \, \rho_\parallel \cos\theta \tag{1.4}$$

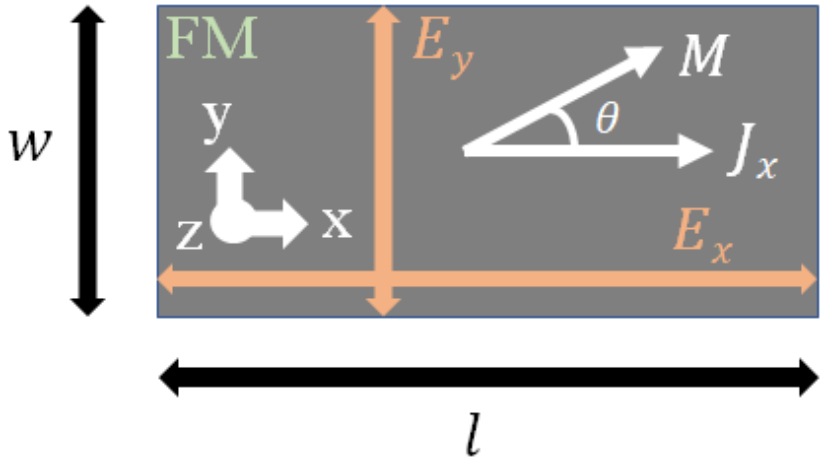

Figure 1.6. Schematic of AMR theory used to derive PNE equation.

The PNE occurs due to spin dependent scattering coming from spin orbit interactions even as in the AMR effect. Among the known mechanisms through which the spin orbit interactions occurs are [41] – First, the intrinsic deflection mechanism, which is dependent on the band structure of the material and comes from the Berry phase; second is the Side jump scattering mechanism, which comes from deflection of electrons in opposite directions due to the opposite electric field experienced before and after the site of an impurity; third is the skew scattering mechanism which originates from impurity scattering due to effective spin orbit coupling.

X-components of equations (1.3) and (1.4) will give –

$$E_{\perp,x} = E_{\perp} \sin\theta = J_x \rho_{\perp} \sin^2\theta \tag{1.5}$$

$$E_{\parallel,x} = E_{\parallel} \cos\theta = J_x \rho_{\parallel} \cos^2\theta \tag{1.6}$$

Therefore, the net electric field in the x-direction will be –

$$E_x = E_{\perp} + E_{\parallel} \tag{1.7}$$

hence,

$$E_x = J_x\,(\rho_\perp \sin^2\theta + \rho_\parallel \cos^2\theta) \tag{1.8}$$

Using $\sin^2\theta = 1 - \cos^2\theta$ and subsequent rearrangement, equation (1.8) can be written as

$$E_x = J_x\,[\rho_\perp + (\rho_\parallel - \rho_\perp)\cos^2\theta] \tag{1.9}$$

For the electric field in the y-direction, a similar consideration for the y-component of $E_\parallel$ and $E_\perp$ will give the expression for electric field transverse to J_x as –

$$E_y = J_x\,(\rho_\parallel - \rho_\perp)\sin\theta\cos\theta \tag{1.10}$$

$$E_y = J_x\,\left(\frac{\rho_\parallel - \rho_\perp}{2}\right)\sin 2\theta \tag{1.11}$$

Equation (1.10) represents AMR behavior while equation (1.11) represents the transverse AMR or the planar Hall effect (PHE) behavior. In the same FM system when the current density (J_x) is replaced with the temperature gradient $\nabla T_x = \frac{\partial T}{\partial x}$, then thermoelectric force will drive the electric current through the sample. Thus, the current-driven effects in Figure 1.5 will have thermal equivalent terms. The electric field in longitudinal and transverse directions in this case will be given by –

$$E_x = \nabla T_x\,[S_\perp + (S_\parallel - S_\perp)\cos^2\theta] \tag{1.12}$$

and

$$E_y = \nabla T_x\,\left(\frac{S_\parallel - S_\perp}{2}\right)\sin 2\theta \tag{1.13}$$

where $S_\parallel$ and $S_\perp$ are the Seebeck coefficients parallel and perpendicular with respect to magnetization of the FM. Equation (1.12) represents the thermal analog of the AMR behavior known as anisotropic magneto thermopower (AMTP) while equation (1.13) represents the transverse AMTP or the planar Nernst effect (PNE) behavior. If the temperature gradient is uniform across the longitudinal direction, then equation (1.13) can

be written as [35] $E_{y,PNE} = \frac{V_{PNE}}{w}$, $\partial T = \Delta T$, and $\partial x = l$; where l and w are effective lengths for longitudinal thermal gradient and thermal voltage generation in the sample, respectively. Therefore,

$$V_{PNE} = \alpha_{PNE} \frac{\Delta T}{l} w \tag{1.14}$$

where $\alpha_{PNE} = \frac{1}{2}(S_{\parallel} - S_{\perp}) \sin 2\theta$ is the planar Nernst coefficient. The SSE and ANE has $\cos\theta$ whereas the PNE has $\sin 2\theta$ symmetry. These two symmetries can be separated by undertaking angular dependence transverse voltage measurement of the sample.

Multiple experimental setups to measure the PNE in ferromagnetic semiconductor and metal films have been reported. One of the early works on PNE involved a method to measure the response from a hall bar sample that is patterned out of epitaxial dilute magnetic semiconductor $Ga_{1-x}Mn_xAs$ ferromagnetic semiconductor thin films as shown in Figure 1.6, with lateral and longitudinal dimensions of 100 μm - 1 mm and ~10 mm respectively [36]. A step heating method was employed to introduce the temperature gradient (∇T) in the x-direction, which can be measured by attaching thermocouple to the voltage leads V_x. Large magnetic field (H) aligns the magnetization of the ferromagnetic semiconductor parallel to it and rotates in the plane of the sample making an angle Φ_H with the ∇T. The transverse voltage (V_y) is then measured across the transverse electrode arms of the hall bar.

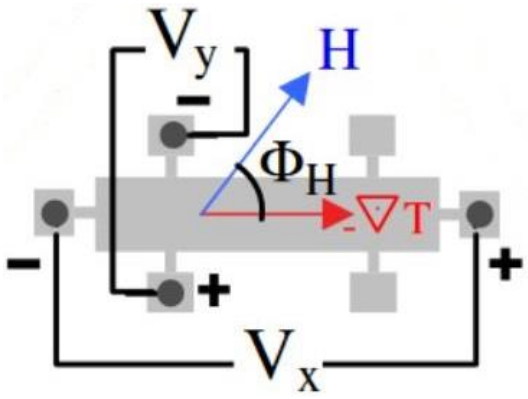

Figure 1.7. Hall bar setup for PNE measurement. Image taken from Y. Pu et al [36].

PNE voltage is also showed to be measured via a heavy metal thin film attached to a ferromagnetic conductor which is subjected to a thermal gradient [37]. This experimental method employed a 20 nm thick and 15 mm^2 permalloy (Py) film on MgO and Sapphire substrates. A 10 nm thin, 100 μm wide Pt film was deposited on one end of the sample as shown in Figure 1.7. The thin film sample on substrate was held using a copper block with copper plates to clamp the film-free substrate edge. The temperature gradient (∇T_x) was monitored using thermocouples placed on the two ends of the sample. In addition, Au contact tip at one end of the Pt voltage lead was independently heated, to generate an out of plane temperature gradient (∇T_z), with a 1 kΩ resistor (R) which is electrically insulated from the tip. Large external magnetic field $\vec{H}$ was applied in the plane of the film making an angle α with the x-direction. In this setup, the applied temperature gradient across the Py film would induce the spin Seebeck effect (SSE). The SSE will generate pure spin current in the Py film which would travel into the Pt film in z-direction and convert into a voltage output via the inverse spin hall effect (ISHE) which can be measured as a transverse voltage (V) across the 100 μm wide Pt strip (Figure 1.7).

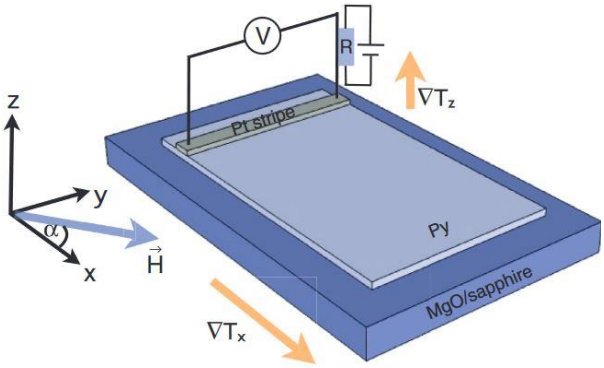

Figure 1.8. PNE measurement setup from Py/Pt bilayer thin film structure. Image taken from D. Meier et al [37].

Substrate effects play a major role in the in-plane thermal transport in a thin film structure [42]. In 2012, Avery et al reported a PNE measurement setup which consisted of thin FM films on a microfabricated freestanding Silicon Nitride based thermal isolation platform that approach the zero-substrate condition [34]. The platform consisted of two 'islands'(leads) connected by a 'bridge' which is 500 nm thick Si-N membrane. The membrane reduces thermal conduction through the substrate by three orders, hence confining the heat flow in the plane of the film only. The island consisted of a Pt heater and thermometer configuration. A 35×800 μm^2, 20 nm thin ferromagnetic metal (Ni and Py) films were deposited on the bridge that also makes a connection at the islands as shown in Figure 1.8. To measure the thermo electric response generated in the ferromagnetic sample, two transverse Pt strips were deposited at the bridge-island joints as shown. Applying current to the Pt heater creates temperature gradient ∇T across the FM film bridge. Transverse (PNE) voltages can then be observed in the Pt strip via inverse spin Hall effect (V_{ISHE}). In in-plane magnetic field (H), V_{ISHE}, when measured as a function of angle

(∅) between magnetization direction and applied thermal gradient will produce a $\sin 2\emptyset$ symmetry. The observed voltage will change sign when measured at 'hot' or 'cold' island.

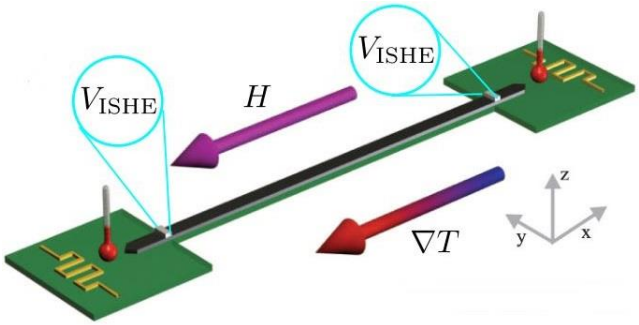

Figure 1.9. Setup for PNE measurement using Si-N thermal isolation platform. Image taken from A. D. Avery et al [34].

1.5 Spin Nernst Effect

In a non-magnetic heavy metal (HM) with high spin orbit coupling, when a longitudinal charge current is applied, a transverse spin current is created via spin Hall effect (SHE) which is expressed by –

$$J_s = \theta_{SH} J_c \times s \tag{1.15}$$

Where J_s is the spin current created; J_c is the applied charge current; θ_{SH} is the charge to spin conversion coefficient called as spin hall angle and s is the spin polarization vector.

Spin Nernst effect (SNE) is the thermal analog of the SHE. In SNE, when a temperature gradient (heat current) is applied in a HM, a transverse spin current is created as shown in Figure 1.9. Like SHE, SNE was also predicted first and then was experimentally observed in heavy metals [43-45] followed by other works . SNE can be expressed as [46]-

$$J_s^{SNE} = \theta_{SN} J_h \times s \tag{1.16}$$

where, J_s^{SNE} is the spin current created due to SNE, θ_{SN} is the spin Nernst angle (analogous to spin Hall angle) and J_h is the heat current applied.

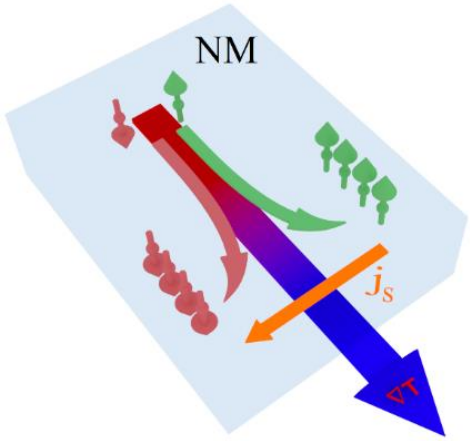

Figure 1.10. Schematic of the Spin Nernst effect where ∇T is the applied thermal gradient and j_s is the transverse spin current generated.

Spin current can be characterized by using a ferromagnetic material along with the normal metal, for example in a FM/HM bilayer structure, where the generated transverse spin current in HM can be absorbed into or reflected from the FM interface resulting in modulation in the longitudinal resistance of the bilayer. This is accomplished by spin Hall magnetoresistance (SMR) method [26]. In SMR when the magnetization (M) of the ferromagnetic layer is parallel to the spin polarization (s) at the FM/HM interface, spin current will be reflected back into the NM and due to ISHE, the reflected spin current will convert back to charge current. Whereas, when the M is orthogonal to S, spin current will get absorbed into the FM via spin transfer torque hence increasing the resistance of the bilayer.

Similar to SMR, resistance modulation in FM/HM bilayer under temperature gradient can characterize the thermally generated spin current or the SNE which can be

termed as spin Nernst magneto resistance (SNMR) as shown in Figure 1.10. SNMR originates due to combination of two effects [44, 46]: first, the creation of spin current due to thermal gradient that is given by θ_{SN} and second, the reflected spin current from the FM/HM interface will be converted back to charge current that is given by θ_{SH}. Therefore, the magnitude of SNMR depends on the product of θ_{SN} and θ_{SH} whereas, it is determined by θ_{SH}^2 in case of SMR [26]. One important characteristic of SMR/SNMR is that, just as the transverse component of SMR is determined as planar Hall effect (PHE), transverse SNMR signal is regarded as planar Nernst effect (PNE).

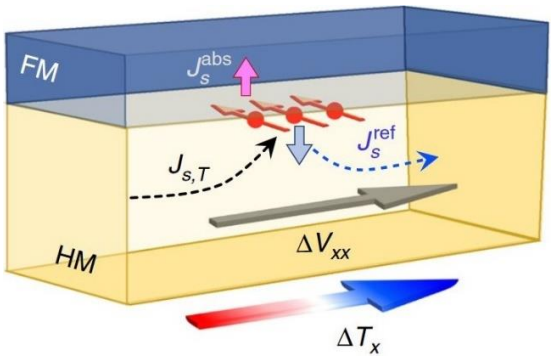

Figure 1.11. The SNMR method. $J_{S,T}$ is the thermally generated current in HM due to ΔT_x; J_S^{ref} and J_S^{abs} are reflected and absorbed spin current from and in to FM layer, respectively. J_S^{ref} is contributing to longitudinal (ΔV_{xx}) via ISHE. Image taken from D. J. Kim et al [44].

SNMR characterization model is similar to SMR with the spin current due to spin Hall effect is replaced by the thermal spin current generation term, electric field measured in the longitudinal and transverse directions are replaced by the respective thermoelectric voltages (ΔV), and the resistivity of the bilayer is replaced by the thermoelectric Seebeck coefficient (S). Let us consider a FM/HM metallic bilayer structure that is consistent in the xy plane and the normal to its interface is in the z-direction. Ohm's Law for metals with

high spin-orbit coupling can be expressed in a matrix form which relates thermodynamic driving forces and currents linearly with Sommerfeld approximation given by [46] –

$$\begin{pmatrix} J_c \\ J_h \\ J_{s,x} \\ J_{s.y} \\ J_{s,z} \end{pmatrix} = \sigma \begin{pmatrix} 1 & ST & \theta_{SH}x \times & \theta_{SH}y \times & \theta_{SH}z \times \\ ST & L_0T^2 & ST\theta_{SN}x \times & ST\theta_{SN}y \times & ST\theta_{SN}z \times \\ \theta_{SH}x \times & ST\theta_{SN}x \times & 1 & 0 & 0 \\ \theta_{SH}y \times & ST\theta_{SN}y \times & 0 & 1 & 0 \\ \theta_{SH}z \times & ST\theta_{SN}z \times & 0 & 0 & 1 \end{pmatrix} \begin{pmatrix} \nabla\mu_0/e \\ -\nabla T/T \\ \nabla\mu_{sx}/2e \\ \nabla\mu_{sy}/2e \\ \nabla\mu_{sz}/2e \end{pmatrix} \quad (1.17)$$

where μ_0 is the spin chemical potential, μ_s is the spin accumulation and ∇T is the temperature gradient. These relate to the charge, spin and heat currents via a tensor that contains electrical conductivity σ, Seebeck coefficient S, Lorenz number L_0, spin Hall and spin Nernst angles. Using the spin diffusion equation in the normal metal and applying quantum mechanical boundary conditions to it, an equation for spin accumulation at the interface (z-direction) can be obtained which is used to determine the spin current in the z-direction which includes the imaginary (G_i) and real (G_r) parts of the spin-mix conductance G of the FM/HM interface. This spin current diffuses into charge current via the inverse spin Hall effect (ISHE) in the x (long.) and y (trans.) directions given by –

$$\frac{J_{c,long.}(z)}{J_{c0}} = 1 + \theta_{SH}\theta_{SN}\left[\frac{\cosh\frac{2z-t_N}{2\lambda}}{\cosh\frac{t_N}{2\lambda}} + (1-m_y^2)\frac{2\lambda G_r \tanh\frac{t_N}{2\lambda}}{\sigma+2\lambda G_r \coth\frac{t_N}{\lambda}}\frac{\sinh\frac{z-t_N}{\lambda}}{\sinh\frac{t_N}{\lambda}}\right] \quad (1.18)$$

$$\frac{J_{c,trans.}(z)}{J_{c0}} = \theta_{SH}\theta_{SN}\left[m_x m_y\left[\frac{2\lambda G_r \tanh\frac{t_N}{2\lambda}}{\sigma+2\lambda G_r \coth\frac{t_N}{\lambda}}\frac{\sinh\frac{z-t_N}{\lambda}}{\sinh\frac{t_N}{\lambda}}\right] - m_z\left[\frac{2\lambda G_i \tanh\frac{t_N}{2\lambda}}{\sigma+2\lambda G_i \coth\frac{t_N}{\lambda}}\frac{\sinh\frac{z-t_N}{\lambda}}{\sinh\frac{t_N}{\lambda}}\right]\right] \quad (1.19)$$

where $J_{c,long.}$ and $J_{c,trans.}$ are the longitudinal and transverse charge current, respectively; J_{c0} is the charge current at the interface of FM/HM bilayer when $G = 0$; t_N is the thickness of HM layer; λ is the spin diffusion length in HM layer; m_x, m_y, m_z are magnetization

vector along x, y and z directions, respectively. The electric fields due to the charge current in equations (1.18) and (1.19) are given by –

$$E_{long.} = \left[1 + \theta_{SH}\theta_{SN}\left[\frac{\cosh\frac{2z-t_N}{2\lambda}}{\cosh\frac{t_N}{2\lambda}} + (1-m_y^2)\frac{2\lambda G_r \tanh\frac{t_N}{2\lambda}}{\sigma+2\lambda G_r \coth\frac{t_N}{\lambda}}\frac{\sinh\frac{z-t_N}{\lambda}}{\sinh\frac{t_N}{\lambda}}\right]\right] S\nabla T_x \tag{1.20}$$

$$E_{trans.} = \theta_{SH}\theta_{SN}\left\{m_x m_y\left[\frac{2\lambda G_r \tanh\frac{t_N}{2\lambda}}{\sigma+2\lambda G_r \coth\frac{t_N}{\lambda}}\frac{\sinh\frac{z-t_N}{\lambda}}{\sinh\frac{t_N}{\lambda}}\right] - m_z\left[\frac{2\lambda G_i \tanh\frac{t_N}{2\lambda}}{\sigma+2\lambda G_i \coth\frac{t_N}{\lambda}}\frac{\sinh\frac{z-t_N}{\lambda}}{\sinh\frac{t_N}{\lambda}}\right]\right\} S\nabla T_x \tag{1.21}$$

where ∇T_x is the temperature gradient in the x-direction. The mean electric field from equations (1.20) and (1.21) calculated over film thickness t_N will be given by –

$$\overline{E_x} = \left[S + \Delta S_0 + \Delta S_1(1-m_y^2)\right]\nabla T_x \tag{1.22}$$

$$\overline{E_y} = \left(\Delta S_1 m_x m_y - \Delta S_2 m_z\right)\nabla T_x \tag{1.23}$$

where,

$$\Delta S_0 = S\theta_{SH}\theta_{SN}\frac{2\lambda}{t_N}\tanh\frac{t_N}{2\lambda} \tag{1.24}$$

$$\Delta S_1 = -S\theta_{SH}\theta_{SN}\frac{\lambda}{t_N}\frac{2\lambda G_r \tanh^2\frac{t_N}{2\lambda}}{\sigma+2\lambda G_r \coth\frac{t_N}{\lambda}} \tag{1.25}$$

$$\Delta S_2 = -S\theta_{SH}\theta_{SN}\frac{\lambda}{t_N}\frac{2\lambda G_i \tanh^2\frac{t_N}{2\lambda}}{\sigma+2\lambda G_i \coth\frac{t_N}{\lambda}} \tag{1.26}$$

Electric field is given by potential difference developed over a distance. Equations (1.22) and (1.23) can, therefore, be written as the longitudinal ($\Delta V_{long.}$) and transverse ($\Delta V_{trans.}$) voltages caused by longitudinal and transverse SNMR -

$$\frac{\Delta V_{long.}}{l_V} = -\left[S + \Delta S_0 + \Delta S_1\left(1-m_y^2\right)\right]\frac{\Delta T_x}{l_T} \tag{1.27}$$

$$\frac{\Delta V_{trans.}}{l_V} = -\left[\Delta S_1 m_x m_y + \Delta S_2 m_z\right]\frac{\Delta T_x}{l_T} \tag{1.28}$$

where ΔV is the potential difference, ΔT_x is the temperature difference across the ends of the bilayer. l_V and l_T are the effect lengths for the thermal voltage generation and longitudinal thermal gradient, respectively. From equation (1.27) it is evident that the longitudinal SNMR voltage depends on the magnetization direction in y-direction (or m_y^2) and proportional to $\sin^2\theta$ and its magnitude can be determined by ΔS_1. From equation (1.28), in absence of out of plane magnetization (m_z), the transverse SNMR voltage will depend on $m_x m_y$ and proportional to $\sin 2\theta$ which is also the symmetry of planar Nernst effect and its magnitude will also be determined by ΔS_1.

SNE has been observed in W/CoFeB/MgO [43], CoFeB/W(Pt) [44], Pt/Ni [45] and Pt/YIG [46] systems providing spin Nernst angles for the heavy metal which is comparable to that of spin Hall angles. One of the first experimental setups to detect SNE consisted of 4.1 nm Pt / 40 nm YIG bilayer thin film structure. YIG was epitaxially grown on $Gd_3Ga_5O_{12}$ substrate. Pt was laser deposited on YIG and the bilayer was patterned into a Hall bar as shown in Figure 1.11 [46]. The thermal gradient needed to generate spin current in HM was introduced by providing power (P_{heater}) to an on-chip Pt/YIG heater source close to the sample. The far end of the sample is connected to the heat sink thereby generating the temperature gradient ($-\nabla T$) across the length of the sample in x-direction. Large external magnetic field (1T) was applied which aligned the magnetization of YIG along its direction. The sample was scanned in xy, yz and xz plane and the resulting longitudinal thermal voltages ($V_{thermal}$) were recorded which gives the spin-Nernst magneto thermopower (SMT) in the bilayer. These voltage measurements depend on the relative orientation of the polarization of spins that were accumulated at the Pt/YIG interface

defined by the SNMR. Since the spin polarization is along the y-axis at the Pt/YIG interface, when the magnetization is along y-direction, the spins at the interface will be reflected back into Pt and convert into charge current via ISHE and contribute to the increase in $V_{thermal}$, whereas magnetization in either x or z-directions will cause ferrimagnet to act as a spin sink hence absorbing the spins from the interface and decreasing the $V_{thermal}$.

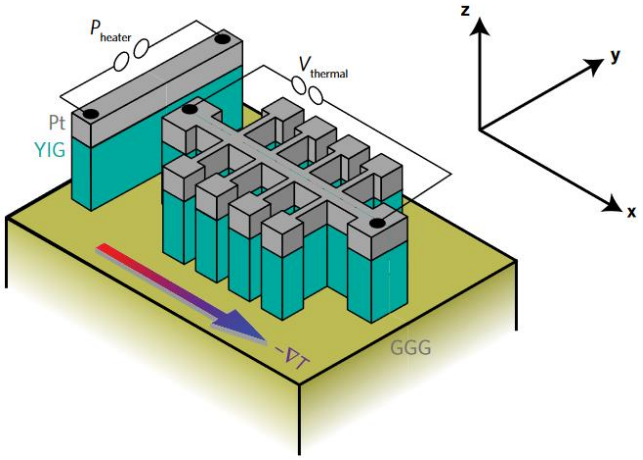

Figure 1.12. Experimental setup for SNE measurement using an isolated heater. Image taken from S. Meyer et al [46].

Another experimental setup to measure SNE explores the non-contact heating method to generate thermal gradient in CoFeB/W(Pt) bilayer thin film using mW laser heating source. The resulting spin current is characterized by measuring the variation in the transverse Hall resistance [44]. This method isolates the transverse SNMR response from the sample. 2 nm CoFeB / 3 nm W (3nm Pt) samples were prepared, along with other control samples, via magnetron sputtering on silicon oxide substrate. The bar-shaped sample measured 10 μm×1 mm in size. A 55 mW laser was shined on the sample to generate thermal gradient. The thermoelectric Hall voltage was then measured under angular rotation on saturating magnetic field as shown in Figure 1.12. The laser spot was

positioned at different locations on the sample film as indicated by light blue, dark blue, black, magenta and red in Figure 1.12 creating ΔT_x and ΔT_z temperature difference in the sample depending on the position of the laser spot. For example, laser heating at the center only had ΔT_z in the sample and as the laser spot moved closer to the edge of the sample, ΔT_z started to diminish and ΔT_x became larger. The Hall response from ΔT_z at the center showed response attributed to longitudinal spin Seebeck effect and anomalous Nernst effect by showing the $\cos\theta$ symmetry. Whereas, the Hall response from ΔT_x at the corner showed response attributed to $m_x m_y$ or the $\sin 2\theta$ symmetry which is also the symmetry for the PNE. The transverse SNMR measured depended on SNE-induced spin current and its conversion into charge voltage via the ISHE, the sign of the transverse SNMR, and equivalently the sign of the PNE corresponding to the SNE, were determined by the product of the spin Hall angle (θ_{SH}) and spin Nernst angle (θ_{SN}). This dependence on Hall and Nernst angles is not valid for SMR measurement since the magnitude of SMR is independent of the sign of θ_{SH} ($\propto \theta_{SH}^2$).

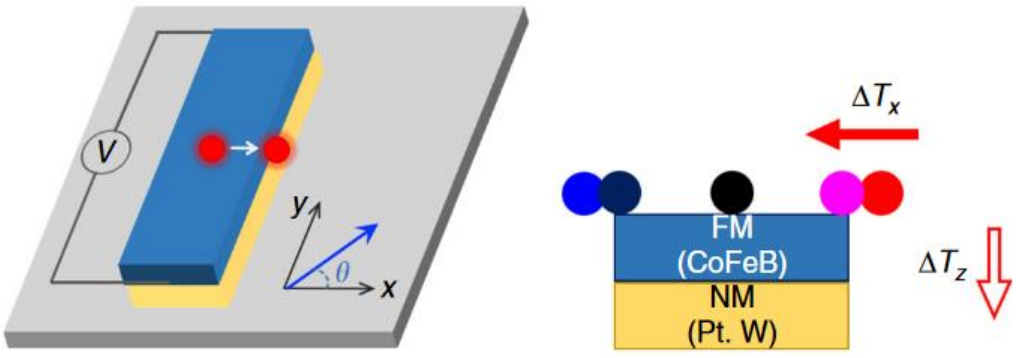

Figure 1.13. Schematic of SNE measurement in CoFeB/W(Pt) bilayer structure with laser heating source for generation of thermal gradient. Image taken from D. J. Kim et al [44].

1.6 Aim and Objectives

The aim of my dissertation research is to investigate magneto-thermal transport in thin metallic and semiconductor films.

Spin polarization, when induced in a non-ferromagnetic material, such as gold (Au), can change the underlying material behavior especially if the spin diffusion length is of the same order as the sample dimension such as thickness. By utilizing methods and procedures detailed in Chapter 2, we experimentally demonstrate the thermal hysteretic behavior induced by spin polarization in $Ni_{80}Fe_{20}$ (10 nm)/Au (100 nm) bilayer freestanding sample. The field induced thermal hysteresis behavior was uncovered using magneto thermal characterization based on self-heating three omega method described in Chapter 2.

Spin polarization occurs in materials with high spin orbit coupling. It can also occur in systems with broken structural inversion symmetry of bulk inversion symmetry. centrosymmetric materials, structural inversion symmetry can be induced using strain gradient. In Chapter 3 we show inhomogeneous strain gradient induced spin polarization is p-Si. The root of this effect is coming from interlayer spin dependent interactions.

Silicon's weak intrinsic spin-orbit coupling is a critical bottleneck towards realization of silicon based spintronics. Ongoing efforts are focused on engineering silicon into a material worthy of efficient spin generation and detection. In Chapter 4, we present an experimental proof of thermal spin current generation using phononic thermal transport in thin film silicon in spite of its insignificant intrinsic spin-orbit coupling. The phonon-driven spin current gives rise to a phononic spin-Nernst effect due to interlayer coupling with

$Ni_{80}Fe_{20}$ thin film. In Chapter 5, we present our understanding of the probable mechanism of the spin phonon coupling in silicon. We attempt to uncover the hidden spin polarization in Si via angle dependent magnetoresistance measurement and look at the different crystal planes and directions in the diamond cubic Si in order to explain the direction dependent spin polarization in p-Si.

Chapter 2 Magneto-thermal transport behavior in freestanding $Ni_{80}Fe_{20}$/Au bilayer thin films

2.1 Introduction

Spintronics is an energy efficient alternative to modern electronics. To realize spintronics devices, spin current with large spin polarization needs to be achieved. Researchers often assume that fundamental behavior of the spin current carrying material, usually non-ferromagnetic, does not change due to spin polarization. However, a normal metal in proximity to ferromagnetic or superconducting metals can exhibit underlying material behavior unexpected of normal metal [47-50]. Recently, There has been experimental studies that report spin dependent behavior in p-Si [51, 52] and n-Si [53]. The reason for such a behavior in Si was that, under certain conditions, spin diffusion length in Si is amplified resulting in interesting phenomena to uncover such as spin polarization, negative magnetoresistance and antiferromagnetic phase transition. It is therefore hypothesized that ferromagnetic proximity mediated transport behavior can be observed in any material if the spin diffusion length is of the same order as the critical dimension.

Gold (Au) is an important material for electronics. Its main applications are in connectors and contacts, wire bonding, soldering and even hybrid circuits [54]. Recently, it was shown that a normal metal, such as Au, can be magnetized [50]. They showed that in a ferromagnet/superconductor/gold thin film layers, under specific environment, gold can become magnetic via long-range spin transfer from the superconductor [50]. Moreover,

Au nanoparticles have been reported to exhibit magnetism [55-57]. These findings open up possibilities to explore Au for spintronics application. The spin diffusion length of Au at room temperature is reported to be 9.5 nm [58] - ~35 nm[59] and can rise to ~98 nm [59, 60] at low temperatures. For a non-local spin valve geometry, the critical dimension will be length. The critical dimension for a bilayer, having ferromagnetic spin source and normal metal layers, will be thickness of the sample. We hypothesized that the ferromagnetic ($Ni_{80}Fe_{20}$) proximity polarization in Au thin films having thickness between 35 nm - 1 μm can induce large spin accumulation leading to changes in transport behavior.

2.2 Method

Device Design

A simple four-point probe or the four-terminal configuration was chosen for the experiments which comprises of four electrodes [61, 62]. Its operation is simple and is relatively easier to fabricate with minimum fabrication steps. Also, it eliminates contact resistances and can be fabricated in large scale. Moreover, this configuration can be made freestanding which broadens its utility. In this design current is passed through the outer two probes or terminals and resulting voltage difference, which carries useful information about the material embedded in it, is measured from the inner pair.

Device Fabrication

A micro electro mechanical system (MEMS) based platform with freestanding specimen was developed to investigate magneto-thermal transport in $Ni_{80}Fe_{20}$/Au bilayer thin film. Devices were made from commercially available 4" (100mm) wide, 300 μm thick double side polished (DSP) prime silicon wafer. As shown in Figure 2.1 (a), first, a new

wafer was rinsed with acetone, then isopropyl alcohol (IPA) and then water to wash out any contaminants present on the surface of the wafer. After drying the wafer, 300 nm silicon dioxide (SiO_2) was deposited on it as a sacrificial layer using plasma enhanced chemical vapor deposition (PECVD) followed by re-cleaning and drying the wafer (Figure 2.1 (b)). AZ-5214 resist was then spin coated on the wafer, and after the baking step an image reversal lithographic pattern was formed using UV lithography. Image reversal is a technique to use positive photoresist to do negative lithography [63]. I first patterned the device specimen area. After developing the wafer in 1:4 AZ-400K:water solvent, only the masked area dissolved in the developer exposing the SiO_2, whereas the unmasked area stayed as a layer of resist on the SiO_2 wafer as shown in Figure 2.1 (c). After this, specimen materials were deposited using e-beam evaporation. A 10 nm of Chromium (Cr) was first deposited to act as an adhesion promoter between the SiO_2 and the 100nm of Au which was deposited right after Cr. Then, 10 nm of $Ni_{80}Fe_{20}$ was deposited and finally a 1 nm of palladium (Pd) protective layer to prevent $Ni_{80}Fe_{20}$ oxidation as shown in (Figure 2.1 (d)). The resist on the wafer was completely stripped by immersing the wafer in an acetone bath for 3-4 hours, followed by IPA and water rinse. This step produced a sharp pattern of device specimen on the wafer while the surrounding space is free from resist. A second spin coating step, using the same resist, and the baking procedure was carried out. After careful alignment of electrode mask and wafer, four electrodes were then patterned onto the device specimen via image reversal technique. This followed another lithographic development process and a second e-beam evaporation step where 100 nm of aluminum (Al) was deposited. A second dip in the acetone bath stripped the resist and Al from unmwanted

areas of the wafer and a complete four-terminal device is fabricated. Multiple devices were patterned on the wafer simultaneously covering the entire surface.

To make the device freestanding, Si was first etched from underneath. UV photolithography was used to pattern 'windows' or openings for dry etcher to etch out the Si underneath the device specimen area. To do this, SPR 220 resist was first spin coated on the backside of the device wafer. After baking on a hot plate, the wafer was mounted on the mask aligner for backside alignment and was subsequently patterned with the etch openings right underneath the device specimen area. After development, Si was exposed right underneath the device whereas the rest of the area was protected by the resist. Device wafer was then mounted on a carrier wafer and placed in a deep reactive ion etcher (DRIE) system which etched out the 300 μm Si exposing the SiO_2 sacrificial layer as shown in Figure 2.1 (e). The remaining resist was stripped, and the device wafer was released from the carrier wafer. Individual devices were taken out from the device wafer and subjected to hydrofluoric vapor etching (HFVE), through the back of the device, which etched out the sacrificial SiO_2 layer underneath the specimen, rendering the device specimen free-standing (Figure 2.1 (f)). It needs to be clarified that while 10 nm Cr is deposited as an adhesion layer, its final thickness may be significantly reduced to HFVE.

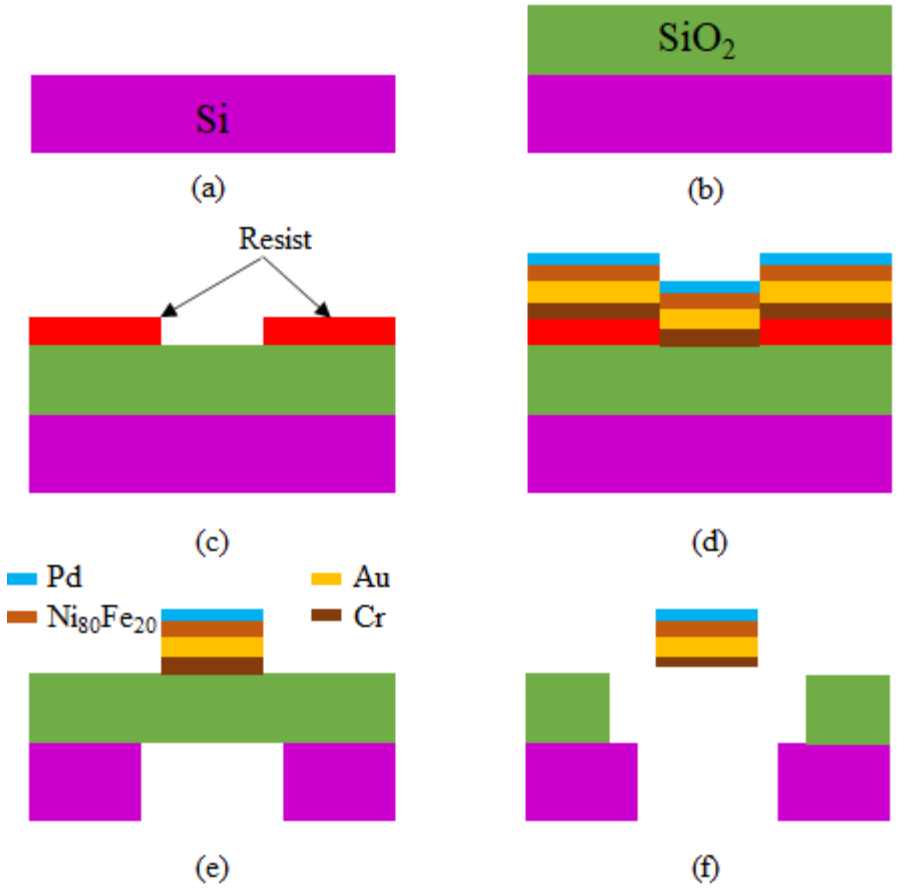

Figure 2.1. Fabrication process of four-terminal freestanding Pd/$Ni_{80}Fe_{20}$/Au/Cr device.

Transport Characterization

Quantum Design's physical property measurement system (PPMS) was used to undertake magneto-thermal transport characterization. This system can produce magnetic field up to 14 T with temperature limits from 400 K down to 1.7 K at pressure down to 1.25×10^{-4} Torr. It also has the functionality of rotating the sample under the influence of external field which is crucial to characterize the family of Hall and Nernst effects. Current was applied using a Keithley source meter and corresponding voltages were obtained via Stanford Research System's 830 lock-in amplifiers.

Thermal transport in our $Ni_{80}Fe_{20}$/Au device was electrically detected via the three omega (3ω) method. This method relates thermal fluctuations, caused by alternating current, with the thermal properties of the system to which current is applied. The 3ω theory given by Chris Dames [64] is as follows: "*the electrical current at angular frequency ω causes joule heating at DC and 2ω. Because the response in the thermal domain is linear, this 2ω heating causes temperature fluctuations also at 2ω, with an amplitude and phase that depends on the thermal properties of the system. This perturbs the heater's electrical resistance at 2ω, which when multiplied by the driving current at ω finally causes a small voltage signal across the heater at a frequency 3ω*."

In a device joule heating occurs in a device with applied alternating current given by –

$$I(t) = I_0 \sin(\omega t) \tag{2.1}$$

where I_0 is the root mean squared amplitude of applied current. ω is the frequency of applied alternating current, and t is the time. This current will cause thermal fluctuation given by –

$$\Delta(x,t) = T(x)\sin(2\omega t + \delta) \tag{2.2}$$

where $\Delta(x,t)$ is the temperature fluctuation in space and time, $T(x)$ is the spatial temperature fluctuation amplitude and δ is the phase angle. This thermal fluctuation will cause resistance fluctuation given by –

$$R(x,t) = R_0 + R'T(x)\sin(2\omega t + \delta) \tag{2.3}$$

$$R(x,t) = R_0 + R'\Delta(x,t) \tag{2.4}$$

where R_0 is the resistance calculated at current I_0 and at temperature T_0. R' is the derivative of R_0 with respect to temperature at T_0, $(\frac{dR_0}{dT})_{T_0}$. Multiplying equations (2.1) and (2.3), we get voltage –

$$V = I(t) \times R(x,t) \tag{2.5}$$

or

$$V = I_0 \sin(\omega t) \times [R_0 + R'\Delta(x,t)] \tag{2.6}$$

In third harmonic, equation (2.4) would reduce to

$$V_{3\omega} = \frac{1}{2} I_0 R_0 T(x) \tag{2.7}$$

The equation for $V_{3\omega}$ for thin films can be found in the solution of one-dimensional heat equation given by [65]

$$\rho C_p \frac{\partial}{\partial T} T(x,t) - \kappa \frac{\partial^2}{\partial x^2} T(x,t) = \frac{I_0^2 sin^2 \omega t}{LA} [R_0 + R'\Delta(x,t)] \tag{2.8}$$

where ρ, C_p, κ, L & A are mass density, specific heat, thermal conductivity, length of sample between the voltage terminals and cross-sectional area of the thin film sample, respectively. In a suspended thin film structure, by applying parabolic temperature distribution and appropriate boundary conditions, equation (2.6) reduces to

$$V_{3\omega} \approx \frac{4 I_0^3 R R' L}{\pi^4 A \kappa \sqrt{1+(2\omega\gamma)^2}} \tag{2.9}$$

where γ is the thermal time constant and is related with the heat capacity $\left(C_p = \frac{\pi^2 \gamma \kappa}{\rho L^2}\right)$. The $V_{3\omega}$ is a function of both thermal conductivity and heat capacity. The thermal conductivity can be expressed in terms of the third harmonic voltage $V_{3\omega}$ in the low frequency limit $(\omega\gamma \to 0)$ by [65] –

$$\kappa \approx \frac{4I^3 R_o R' L}{\pi^4 V_{3\omega} S} \tag{2.10}$$

The heat capacity and thermal conductivity can thus be considered as a function of resistance and $V_{3\omega}$ response

$$\left(f\left(\kappa, C_p\right) = \frac{R}{V_{3\omega}}\right) \tag{2.11}$$

To ensure parabolic temperature profile along the specimen, device was fabricated to be freestanding to eliminate conductive heat losses and performed experiments in high vacuum environment to reduce convective heat losses. Equation (2.11) was used to study changes in thermal transport as a function of magnetic field and temperature. I demonstrate thermal hysteresis behavior in freestanding $Ni_{80}Fe_{20}$ (10 nm)/Au (100 nm) bilayer sample using magneto-thermal transport characterization. The experimental setup is shown in Figure 2.2. The applied electric current from the outer two probes (electrodes) causes a longitudinal (parabolic) temperature gradient T(x). T_0 is the far field (sink) temperature which can be equated to the cryostat/substrate temperature. The voltages were recorded from the inner two probes. The current across the sample will lead to spin polarization of Au due to, primarily, non-local spin injection [21, 66, 67] or ferromagnetic proximity polarization [47, 48]. The spin polarized Au layer will be equal to the spin diffusion length in Au as shown in Figure 2.3. The spin accumulation can also occur due to spin-Hall effect (SHE) as shown in Figure 2.3. The change in transport behavior due to spin polarization can be studied using the 3ω method as a function of magnetic field and temperature.

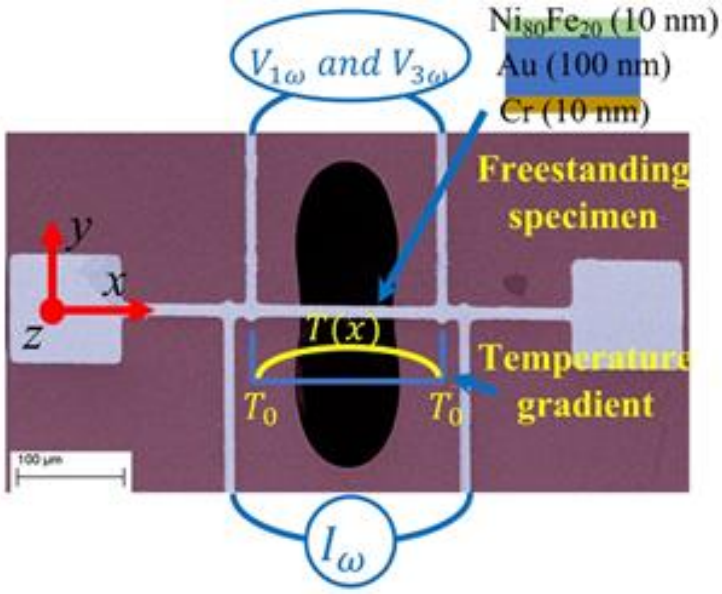

Figure 2.2. The scanning electron micrograph showing the experimental setup with freestanding sample having Pd (1 nm)/$Ni_{80}Fe_{20}$ (10 nm)/Au (100 nm)/Cr (10 nm). Scale bar is 100 µm.

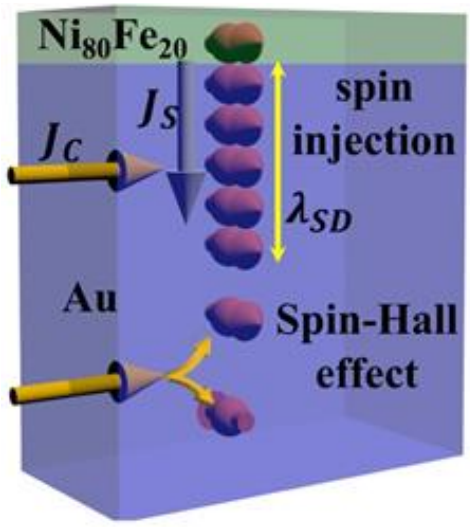

Figure 2.3. Schematic showing the non-local spin injection and spin-Hall effect, which will lead to spin accumulation in Au thin film; J_C is charge current, J_S is spin current and λ_{SD} is spin diffusion length of Au.

2.3 Results

For magneto-electro-thermal characterization, $V_{3\omega}$ response was first measured as a function of applied heating current from 1 mA to 5 mA. The $V_{3\omega}$ response demonstrated a clear cubic relationship with the heating current as shown in Figure 2.4, which is essential for the thermal characterization. Once the cubic relationship was ascertained, $R_{1\omega}$ and $V_{3\omega}$ responses were acquired as a function of magnetic field from 2 T to -2 T applied out of plane (z-direction). The applied magnetic field had no influence on the resistance of the sample at 300 K, which can be seen as flat magnetoresistance (MR) behavior in Figure 2.5 (a) even when the field polarity is reversed. Since the sample was metallic, it must obey Wiedemann Franz law ($\sigma \propto \kappa_{el}$ [68], where σ is the electrical conductivity and κ_{el} is electronic thermal conductivity) and thus, no change in electrical conductivity implies no change in thermal conductivity too, which means magnetic field dependent $V_{3\omega}$ response should also exhibit no change ($V_{3\omega}$ is related with κ according to equation (2.10)). However, the $V_{3\omega}$ response was observed to be weakly dependent on the applied magnetic field as shown in Figure 2.5 (b).

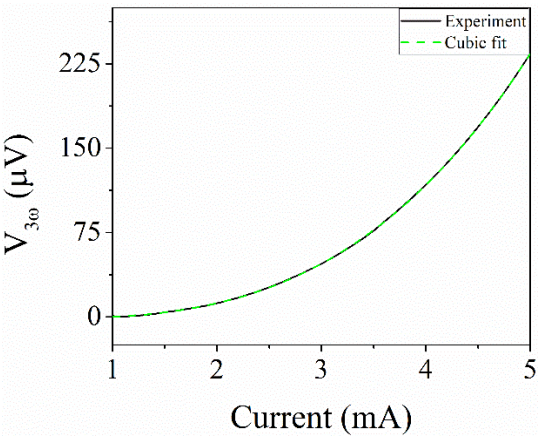

Figure 2.4. The $V_{3\omega}$ response as a function of heating current showing cubic relationship.

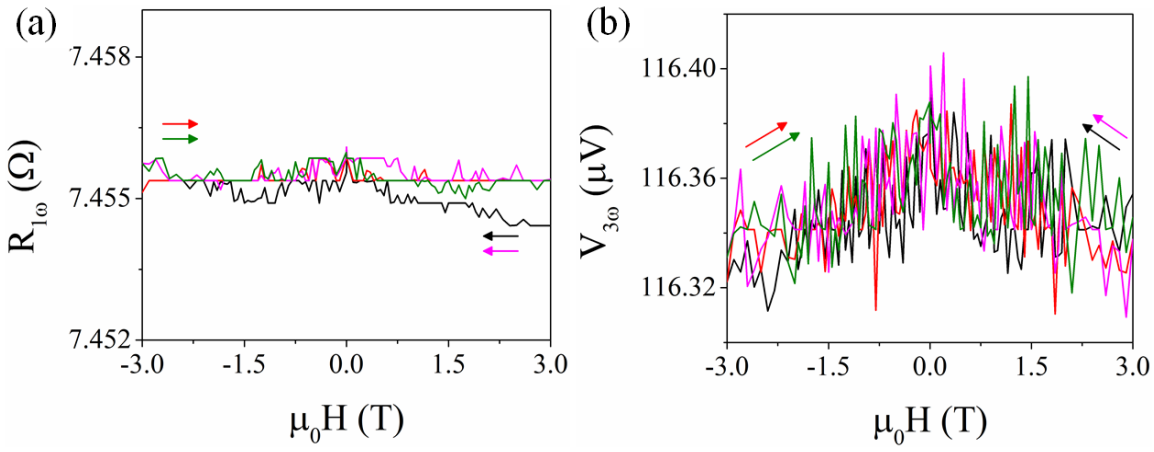

Figure 2.5. (a) MR at 300 K, and (b) the $V_{3\omega}$ response as a function of magnetic field (z-direction) at 300 K. Arrows in (a) & (b) indicate the direction of field sweep.

To uncover the temperature dependent thermal transport behavior, the $R_{1\omega}$ and $V_{3\omega}$ responses were measured as a function of temperature from 300 K to 5 K on a second device. The measurements were carried out at 5 mA of heating current, no magnetic field, and 0.3 K/min of heating and cooling rate. The $R_{1\omega}$ measurement showed thermal hysteresis behavior as shown in Figure 2.6 (a), which can be attributed to the thermal drift originating from the measuring instrument. Similar thermal hysteretic behavior can also be seen in the $V_{3\omega}$ response as shown in Figure 2.6 (b). Then, $R_{1\omega}$ and $V_{3\omega}$ responses were measured as a function of temperature from 300 K to 50 K under an applied out of plane (z-direction) magnetic field of 1 T. But this time heating current was reduced to 3 mA and cooling/heating rate to 0.3 K/min to reduce the thermal drift which then also reduced thermal drift in the $R_{1\omega}$ as shown in Figure 2.7 (a). This measurement was carried out on a third device to ensure the repeatability of experimental results. The slope of the resistance as a function of temperature is measured to be 0.01357 Ω/K and the difference between the heating and cooling resistance is measured to be ~0.005 Ω. Using this information, the

thermal drift was estimated to be ~0.4 K, which is low. Unlike the resistance measurement, the $V_{3\omega}$ response showed a significant thermal hysteresis under applied magnetic field, which could not be attributed to instrumental thermal drift since the $V_{3\omega}$ value at the end of heating is lower than any value during cooling (Figure 2.7 (b)). Two diverging valleys were observed during cooling (u, 238.2 K) and heating (v, 275.25 K). These valleys occurred at different temperatures as shown in Figure 2.7 (b). Under the influence of magnetic field (1 T along z-direction), the temperature dependent behavior was similar to the field-sweep measurement (Figure 2.5 (a) and (b)) i.e. resistance doesn't change at the start and end of the temperature cycle and $V_{3\omega}$ response dropped significantly while coming back to room temperature.

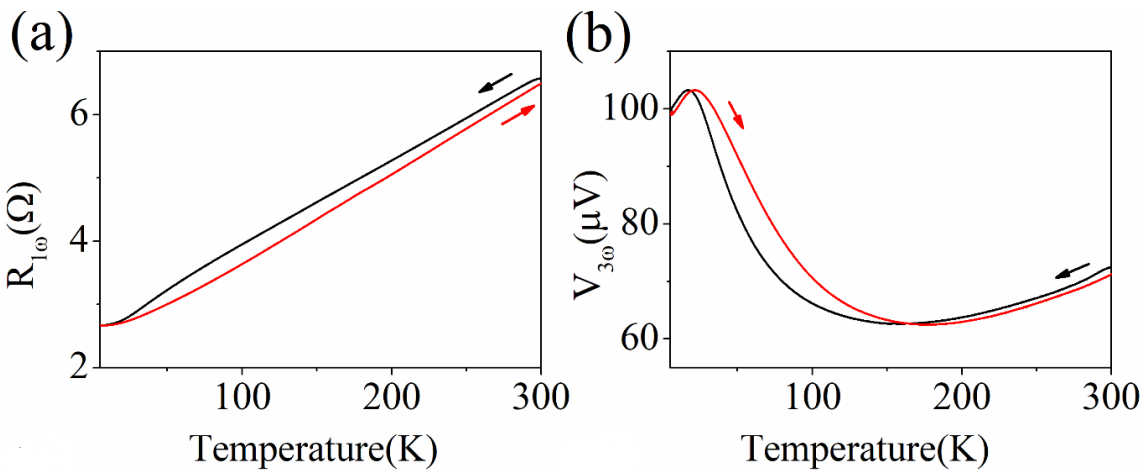

Figure 2.6. (a) resistance and (b) the $V_{3\omega}$ response as a function of temperature between 300 K and 5 K at 0.3 K/min and 5 mA of heating current applied across the sample and zero applied magnetic field showing hysteresis in cooling and heating thermal cycle attributed to the thermal drift.

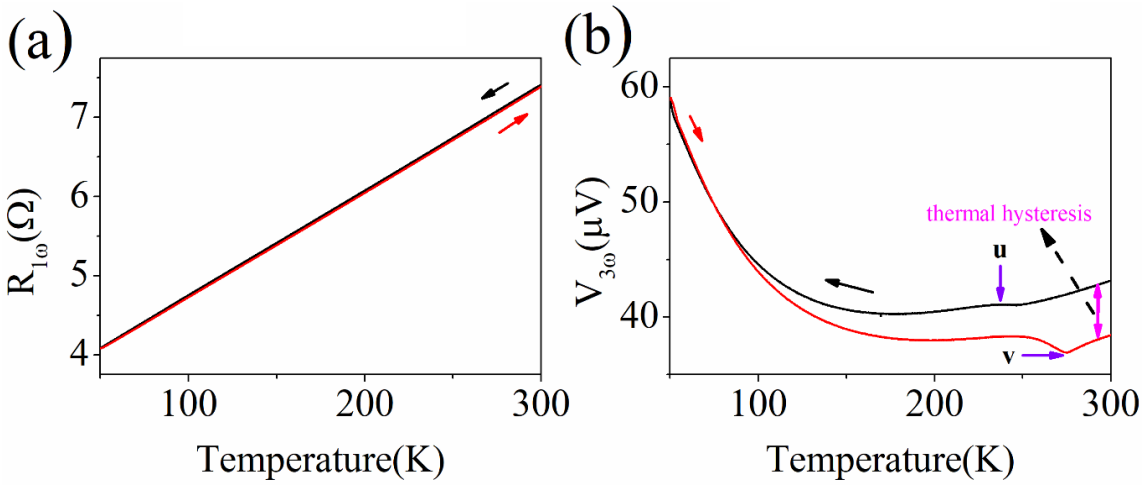

Figure 2.7. (a) The resistance and (b) the $V_{3\omega}$ response as a function of temperature between 300 K and 50 K at 0.3 K/min and 3 mA of heating current and applied magnetic field of 1T along z-axis.

To understand the $V_{3\omega}$ response, equation (2.10) was analyzed. Using Fourier's equation for thermal conduction, we can write –

$$\kappa \approx \frac{4I^3 R_o R' L}{\pi^4 V_{3\omega} S} = \frac{(I^2 R_o) L}{S}\left(\frac{4IR'}{\pi^4 V_{3\omega}}\right) = \frac{\dot{Q} L}{S}\left(\frac{1}{\Delta T}\right) \tag{2.12}$$

$$\Delta T = \frac{\pi^4 V_{3\omega}}{4IR'} \tag{2.13}$$

where, ΔT is the temperature gradient which is proportional to the $V_{3\omega}$ response. The equation for temperature gradient is similar in form to the equation for temperature gradient given in original 3ω method for cross-plane thermal conductivity by D. Cahill [69]. From the equation (2.13), it can be stated that the temperature gradient in Figure 2.7(b) was reduced during one cycle of cooling and heating. The valleys (u and v) can be interpreted as a magnetocaloric effect, which leads to the thermal hysteresis behavior similar to magnetocaloric effects [70, 71]. However, this behavior is not a traditional thermal hysteresis behavior due to magnetocaloric effect [70, 72-75] since only temperature

gradient (ΔT) is reduced and not the actual temperature. This could be an emergent (not intrinsic) magnetocaloric effect due to combined effect of $Ni_{80}Fe_{20}$ and Au layers.

As stated earlier, the thermal hysteresis can be considered as a reduction in temperature gradient using equation (2.13). To further understand the emergent behavior as well as the valleys in the temperature dependent behavior, $R_{1\omega}$ and $V_{3\omega}$ responses were recorded cyclically under cooling and heating between 300 K and 200 K at cooling/heating rate of 1 K/min. This higher cooling/heating rate may induce thermal drift, which can be quantified. $V_{3\omega}$ responses were acquired for 12 cycles of cooling and heating at an applied out of plane magnetic field of 1 T. During this measurement, the $V_{3\omega}$ response dropped after every cycle of cooling and heating as shown in Figure 2.8 (a). To uncover the effect of magnetic field, measurement was carried out for four cycles each at 2 T (red line) and at 0.5 T (blue line). 0.5 T was applied in the plane (y-direction) to reveal any dependence on field direction. These measurements also exhibited similar reduction in the $V_{3\omega}$ response shown in Figure 2.7 (b). During this measurement (20 cycles), the $V_{3\omega}$ response dropped from ~42.5 μV (point r) to ~32.2 μV (point s) as shown in Figure 2.8 (a) while resistance values were stable as shown in Figure 2.8 (b). Using this resistance data, the instrumental thermal drift was estimated to be ~10.12 K whereas the thermal hysteresis in the $V_{3\omega}$ response was much larger. One important observation in Figure 2.8 (a) is that the magnitude and direction of the magnetic field did not have significant effect on the $V_{3\omega}$ response behavior and the drop in the $V_{3\omega}$ response after each cycle was primarily a temperature dependent phenomenon but in the presence of magnetic field. The reduction in the $V_{3\omega}$ response cratered after 20 cycles and further reduction during each thermal cycle

of cooling and heating was insignificant. The cooling transition behavior was completely suppressed but heating transition could be observed after 20 thermal cycles. The thermal hysteresis [70, 72-75] behavior can arise due to magnetocaloric effect as stated earlier in addition to spin-crossover due to spin accumulation [76].

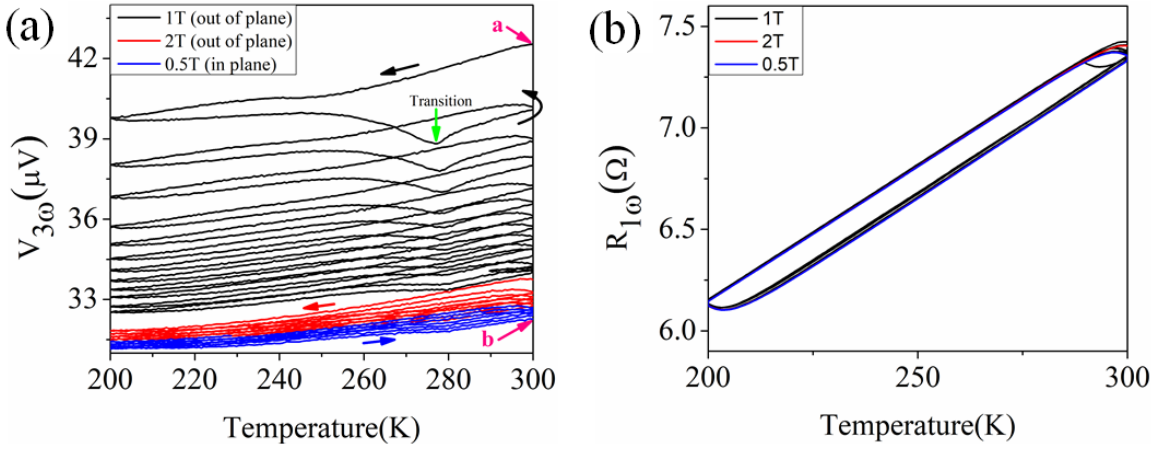

Figure 2.8. (a) the $V_{3\omega}$ response as a function of temperature cycled between 300 K and 200 K at applied magnetic field of 1 T (black) for 12 cycles, 2 T (red) for 4 cycles and 0.5 T (blue) for 4 cycles, and (b) The resistance as a function of temperature cycled between 300 K and 200 K showing the thermal drift for 20 cycles between 300 K and 200 K. Resistance values during cooling and heating are same during thermal cycling indicating absence of thermal hysteresis. Temperature sweep rate: 1 K/min for (a) & (b).

2.4 Discussion

$R_{1\omega}$ and $V_{3\omega}$ responses in our sample at high current (5 mA), in Figure 2.6 (a) & (b), showed hysteretic behavior due to instrumental thermal drift. To ascertain it, temperature sweep measurements at 0.2 K/min were acquired at high current of 4.5 mA and no applied magnetic field. $R_{1\omega}$ and $V_{3\omega}$ responses were recorded as shown in Figure 2.9 (a) & (b), respectively. The temperature was swept in the order 400 K → 10 K → 150 K → 50 K → 400 K to observe hysteresis in the sample under repeated heating and cooling cycles. The thermal hysteresis responses for $R_{1\omega}$ and $V_{3\omega}$ were very similar to the responses

as shown in Figure 2.6 (a) & (b). Changing the temperature sweep rate from 0.4 K/min (in Figure 2.6) to 0.2 K/min showed that the thermal drift is independent of cooling/heating rate and occurs due to the large heating current. Upon decreasing the current to 10 μA, the $R_{1\omega}$ showed very low drift when the temperature was swept from 400 K to 10 K and back at 0.4 K/min, as shown in Figure 2.10 (a). The $V_{3\omega}$ behavior, on the other hand, stayed flat with noise [Figure 2.10 (b)] indicating that it is insensitive to low currents. This result showed that the thermal drift is proportional to heating current applied in the system, and the drift is more pronounced at lower temperature range. In Figure 2.9 (b), in the absence of externally applied magnetic field the higher (235 K – 275 K range) temperature transition in the $V_{3\omega}$ response do not exist since the intrinsic moments (spins) of individual magnetic domains would be randomized in the magnetic $Ni_{80}Fe_{20}$ layer as shown in Figure 2.11 (a). Upon applying large, saturating fields the spins in all the domains would orient themselves in the applied field's direction [Figure 2.11 (b)] thus inducing the spin accumulation in the nonmagnetic Au film which resulted in the thermal hysteresis behavior as shown in Figure 2.7 (b).

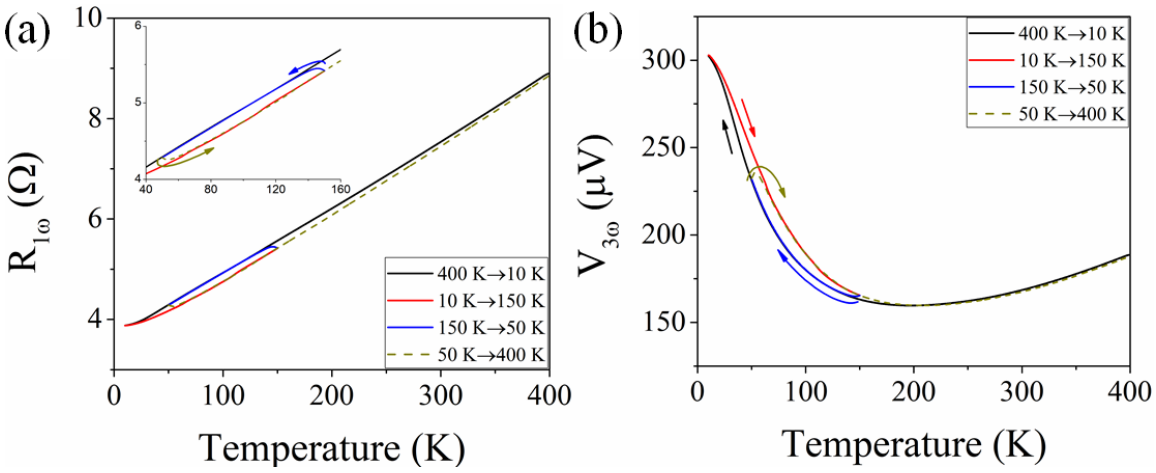

Figure 2.9. (a) The resistance and (b) voltage response when the temperature is swept, from 400 K to 10 K to 150 K to 50 K to 400 K, at 0.2 K/min and 4.5 mA of heating current applied across the sample and zero applied magnetic field showing hysteresis in repeated cooling and heating thermal cycle attributed to the thermal drift.

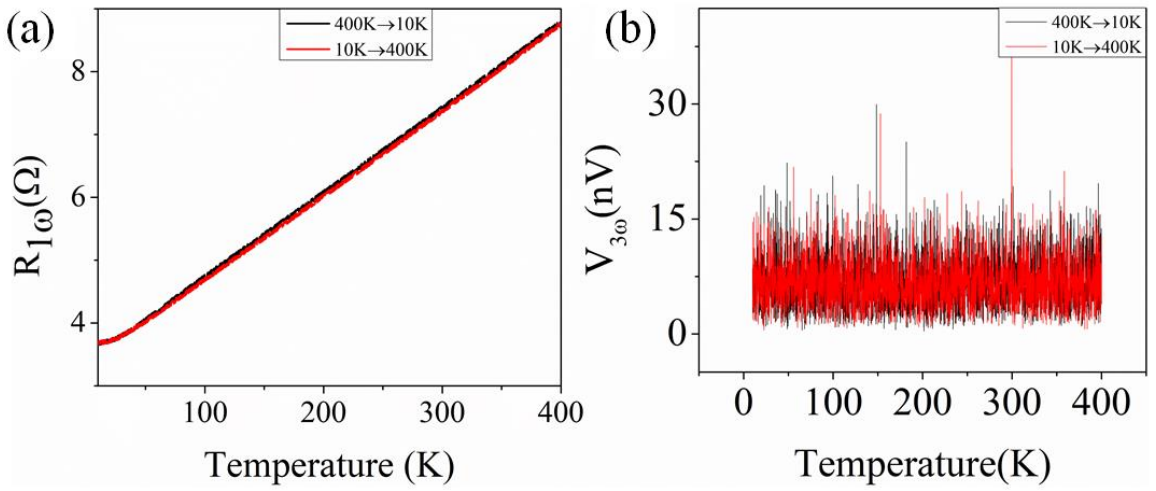

Figure 2.10. (a) The resistance, and (b) voltage response when the temperature is swept, from 400 K to 10 K and back at 0.4 K/min and 10 μA of heating current applied across the sample and no applied magnetic field.

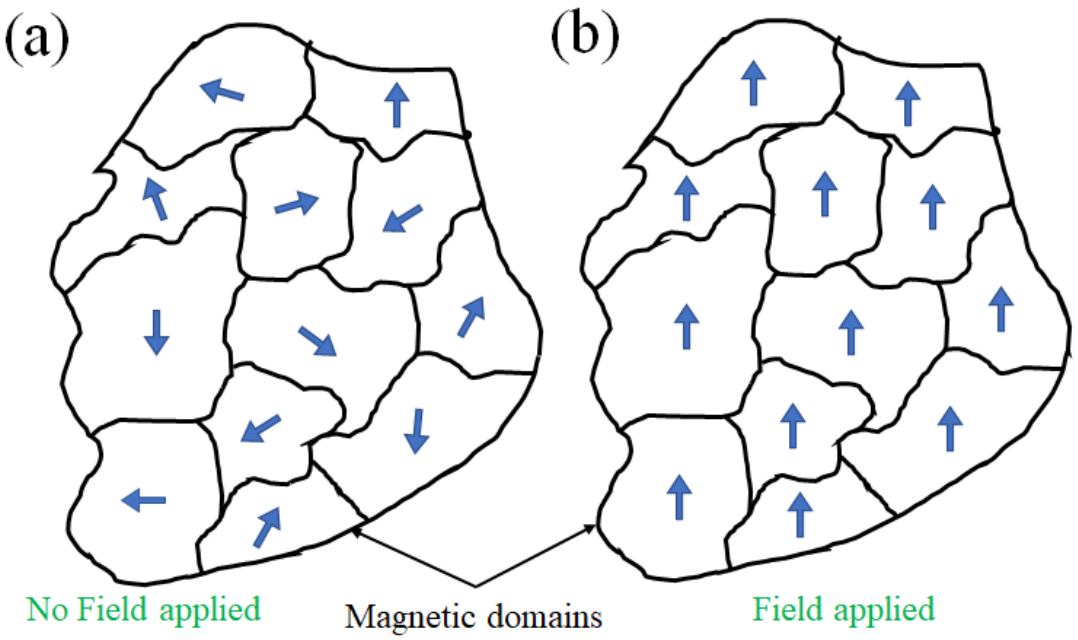

Figure 2.11. Magnetic domains in $Ni_{80}Fe_{20}$ thin film (a) when no magnetic field is applied resulting in randomized intrinsic moment in individual domains, and (b) when large magnetic field is applied which aligns the spins in all the domains along its direction.

Obtained experimental results were surprising and unexpected to arise from the Au thin films only. While nanoscale Au thin films (<15 nm) and Au nanoparticles have been reported to exhibit magnetism at low temperatures (below 4 K) [50, 57, 77-81], there is no reported study of high temperature behavior similar to this study. As mentioned earlier, the observed magneto-thermal transport behavior can arise in Au thin films due to spin polarization since the spin diffusion length is of the same order as the thickness of the sample. The enhancement in spin accumulation due to confinement has been reported for Permalloy/Au thin film structures [82], which has been used to study spin transport [83, 84]. Spin accumulation mediated magnetization in Au thin films has also been observed [85]. There are multiple mechanisms that can lead to spin accumulation in the Au layer. These include Rashba-Edelstein effect [86], spin-Hall effect and ferromagnetic proximity

polarization. Both Rashba-Edelstein effect and spin-Hall effect can be uncovered using angle dependent magnetoresistance (ADMR) [87]. The ADMR measurement in zy-plane at 300 K and 1 T did not show any angle dependent behavior (Figure 2.10 (a)), which eliminates both Rashba-Edelstein effect and spin-Hall effect as an underlying mechanism for spin accumulation. However, it needs to be noted that a weak spin-Hall magnetoresistance (SMR) response was observed in the sample at 25 K (Figure 2.10 (b)), but this will not affect the high temperature thermal hysteresis behavior. In addition, the current density in the measurements was relatively small ($2.7 \times 10^5 \frac{A}{cm^2}$). As a consequence, Rashba-Edelstein effect is not expected to give rise to significant spin accumulation.

This led us to hypothesize that ferromagnetic metal layer is the underlying cause of spin accumulation. This spin accumulation from $Ni_{80}Fe_{20}$ layer would not arise when there is no magnetic field applied, as shown in Figure 2.6 (a) & (b), because the magnetic moments are randomized in this state and, as a result, the net magnetization is negligible. A non-zero net magnetization required for spin accumulation in Au results only upon application of external magnetic field. The hybridization at Au and $Ni_{80}Fe_{20}$ interface may lead to proximity induced magnetization without the need of a current or thermal gradient. To ascertain it, we undertook a thermal cycling experiment where current was only applied to measure the $V_{3\omega}$ response at the start and at the end. During the cooling (300 K to 200 K) and heating (200 K to 300 K) of the sample, the applied current was switched off. In this measurement, the $V_{3\omega}$ response was same before and after thermal cycling unlike the

thermal hysteresis behavior shown in Figure 2.7 (b) and 2.8 (a). This led to the conclusion that interfacial hybridization was not the underlying cause of thermal hysteresis.

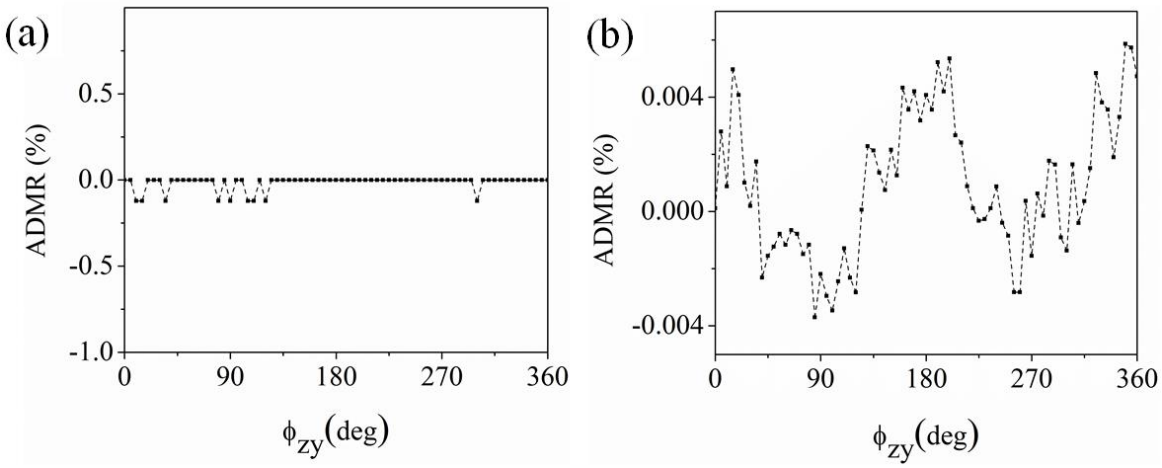

Figure 2.12. Angle dependent magneto resistance (ADMR) or spin Hall magneto resistance (SMR) responses of the $Ni_{80}Fe_{20}$/Au device at 1 T and at (a) 300 K showing no SMR response, and (b) 25 K showing weak SMR response.

The ferromagnetic layer can also influence the behavior due to ferromagnetic proximity polarization, which will include spin injection as shown in Figure 2.3. In order to ascertain the contribution from $Ni_{80}Fe_{20}$ layer to the observed thermal hysteresis behavior, a $Ni_{80}Fe_{20}$ thin film control sample was fabricated on the suspended oxide layer. The control sample on suspended oxide removed the substrate effects. The sample could not be made freestanding since HF chemically etches the $Ni_{80}Fe_{20}$ thin film. Resistance and the $V_{3\omega}$ responses were recorded as a function of temperature from 300 K to 50 K as shown in Figure 2.11. The control $Ni_{80}Fe_{20}$ sample has higher resistance than expected, which can be attributed to oxidation of the sample. However, the $V_{3\omega}$ response showed a diverging behavior at ~240 K similar to Au bilayer sample (point u in Figure 2.7 (b)). This control experiment clearly showed that the likely origin of the thermal hysteresis behavior is

$Ni_{80}Fe_{20}$ thin film, which means that ferromagnetic proximity polarization due to spin injection is the underlying mechanism as shown in Figure 2.12. The thermal hysteresis behavior can be considered as a magnetocaloric effect. The magnetocaloric effect has been proposed in ferromagnetic/paramagnetic heterostructures. This behavior arises due to interactions between ferromagnetic layer effecting the magnetic moment in paramagnetic metal [88]. The experimental results obtained supports this mechanism. The magnetocaloric effect leads to successive reduction in $V_{3\omega}$ response. This effect can be attributed to the freestanding thin film structure as well since the substrate mediated thermalization of phonons is absent.

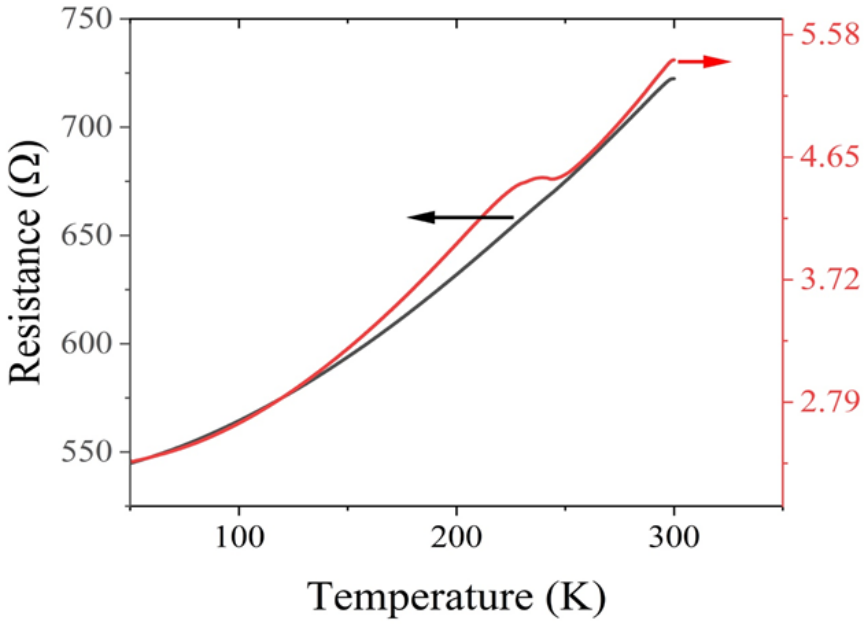

Figure 2.13. The measurement of resistance (Ω, black) and $V_{3\omega}$ (μV, red) response as a function of temperature from 300 K to 50 K showing a bump in $V_{3\omega}$ response at ~240 K.

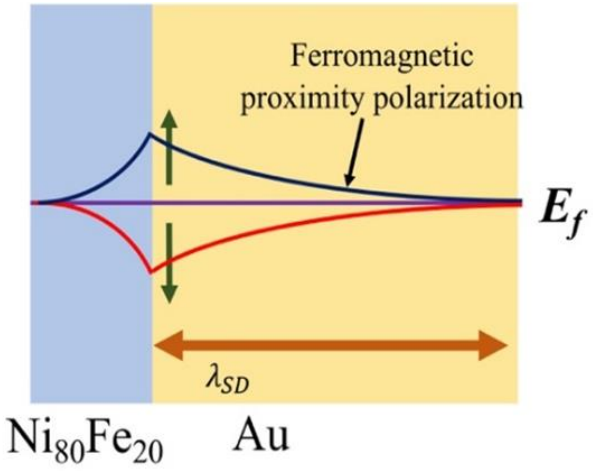

Figure 2.14. Schematic showing the mechanism of ferromagnetic proximity polarization and spin accumulation at the Ni80Fe20/Au bilayer interface.

2.5 Conclusion

We show experimental measurement of magneto-thermal transport behavior in the $Ni_{80}Fe_{20}$ (10 nm)/Au (100 nm) bilayer freestanding sample. The thermal transport behavior was uncovered using self-heating 3ω-method based magneto thermal characterization. The third harmonic voltage showed diverging behavior and thermal hysteresis during cooling and heating under an applied magnetic field. The thermal hysteresis was attributed to ferromagnetic proximity polarization and weak magnetocaloric effect in $Ni_{80}Fe_{20}$ thin films. The observed behavior can also be attributed to absence of substrate effects leading to longer spin diffusion length and spin lifetimes. These experimental results in Au thin films may provide scientific direction to study spin dependent behavior in widely studied diamagnetic and paramagnetic materials. In addition, layered thin films structures of normal metals/ferromagnetic metals can be used to achieve magnetocaloric effect without using complex and rare earth magnetic materials.

Chapter 3 Crystallographic Direction Dependent Spin Polarization in Silicon

3.1 Introduction

Silicon is a semiconductor material predominantly used in electronics due to its high abundance, low cost and versatility. It is the most widely exploited material for electronic device applications. After the beginning of spintronics device research it was therefore obvious to explore the silicon based spintronics [89]. It was found that Si is not an effective material for controlling spins after a discovery in 2012 which exposed that it has a weak intrinsic spin orbit coupling with a spin Hall angle of 0.0001 [90]. However, it was proposed to be used as a spin channel [91]. In other words, Si is inefficient in generation and detection of a spin current, which is the key element in realization of spintronic devices. Therefore, discovering ways to enhance spin polarization in Si is crucial for advancement of Si spintronics research.

The spin polarization due to spin-Hall effect (SHE) [92, 93] and its reciprocal arises in materials with large intrinsic spin-orbit coupling (SOC). However, large SOC can also arise due to broken inversion symmetry. In case of centrosymmetric materials, the symmetry can be altered using inhomogeneous strain [93-97]. The broken symmetry in centrosymmetric materials may give rise to flexoelectric polarization due to a strain gradient as shown in Figure 3.1 [98]. Flexoelectric polarization is the charge separation caused due to inhomogeneous strain. Recently, the flexoelectric effect [99-102] due to a

strain gradient has been experimentally observed in centrosymmetric Si [103], which provides a foundation for this study. Based on the flexoelectric coefficient reported for Si [104], the strain and strain gradient mediated spin-dependent interaction may lead to spin polarization in Si. Traditionally, strain gradient experiments involve bending thin films on soft substrates [103]. Alternatively, a freestanding beam will buckle automatically due to residual stresses. The stresses and, as a consequence, the buckling can be controlled using thermal expansion. Within this framework, we perform experimental measurement of crystallographic direction dependent spin polarization in p-doped Si free-standing thin films using magnetoresistance (MR) and longitudinal $V_{2\omega}$ behavior in the presence of applied magnetic field.

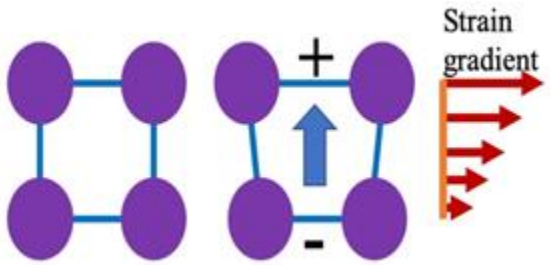

Figure 3.1. Flexoelectric charge polarization in a crystal due to strain gradient.

3.2 Method

Device Design

A four-terminal device configuration was selected for the experiments. Devices were designed such that the current channels are oriented along the four crystallographic directions of the Si (100) wafer starting at <110> direction (or 0˚) and ending at <100> direction (or 45˚) with increments of 15˚ as shown in Figure 3.2.

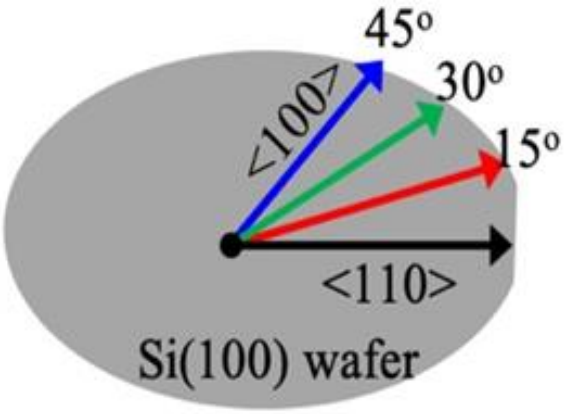

Figure 3.2. Orientation of the crystallography devices on silicon (100) wafer with 0˚ device aligned along <110> direction followed by devices oriented 15˚, 30˚ and 45˚ w.r.t <110>.

Device Fabrication

A set of freestanding devices were made from 4" (100mm) silicon on insulator (SOI) wafer. An SOI wafer is composed of a SiO_2 layer, called the box layer, sandwiched between two Si layers known as the device layer (on the top) and the handle layer (at the bottom) as shown in Figure 3.3 (a). An SOI wafer with 2 μm device (p-Si in this study) layer, 300 μm undoped handle layer and 1 μm SiO_2 box layer was used for this study.

General cleaning and resist stripping procedures, similar to four-terminal device fabrication (Section 2.2), were followed. An SOI wafer was cleaned, and spin coated with S 1813 resist. Crystallography device sample structure was patterned on the wafer by UV lithography. The p-Si from the device layer surrounding the sample was exposed after development of the positive resist as shown in Figure 3.3 (b). Patterned SOI wafer was then mounted on a carrier wafer via a thermal release tape and placed inside the DRIE system to etch out the 2 μm device layer, hence exposing the SiO_2 box layer underneath it as shown in Figure 3.3 (c), followed by stripping the resist from the wafer by dipping it in acetone

bath and rinsing with IPA and water (Figure 3.3 (d)). The box layer was removed with the help of HFVE to make the p-Si layer freestanding as shown in Figure 3.3 (e). The wafer was then placed inside a sputter chamber where Argon ion milling was first performed for 15 minutes to get rid of the native SiO_2 on the p-Si layer. The Argon mill was followed by deposition of 1 nm of MgO layer (to eliminate Ni or Fe diffusion into p-Si and act as an efficient spin tunnel) and 25 nm of $Ni_{80}Fe_{20}$ layer (Figure 3.3 (f)). The 1 µm oxide layer electrical isolated the electrodes, and the p-Si was doped with Boron. The length of the sample was 600 µm. Applied current is oriented at 0˚ for <110> directions all the way to 45˚ for <100>.

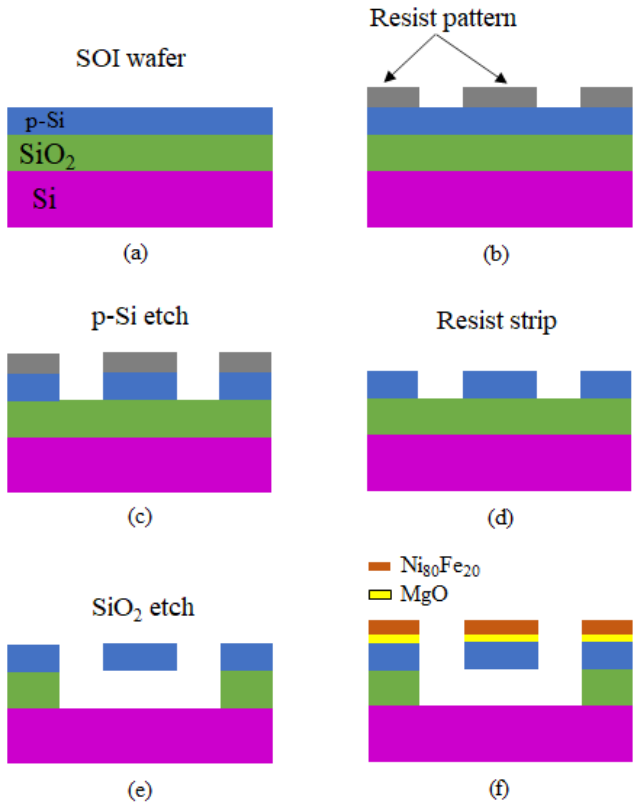

Figure 3.3. Fabrication procedure of SOI wafer device for crystallography experiment.

There are two contributions to the strain and strain gradient in a freestanding thin film: residual thermal expansion strain due to the thin film processing and buckling strain due to the removal of the substrate. The strain profile in the specimen will be superposition of a uniform normal strain due to thermal expansion and a strain gradient due to buckling as shown in Figure 3.4. We hypothesized that in presence of strain gradient, crystallographic direction dependent applied current would alter the spin dependent interactions between $Ni_{80}Fe_{20}$ and p-Si and lead to spin polarization.

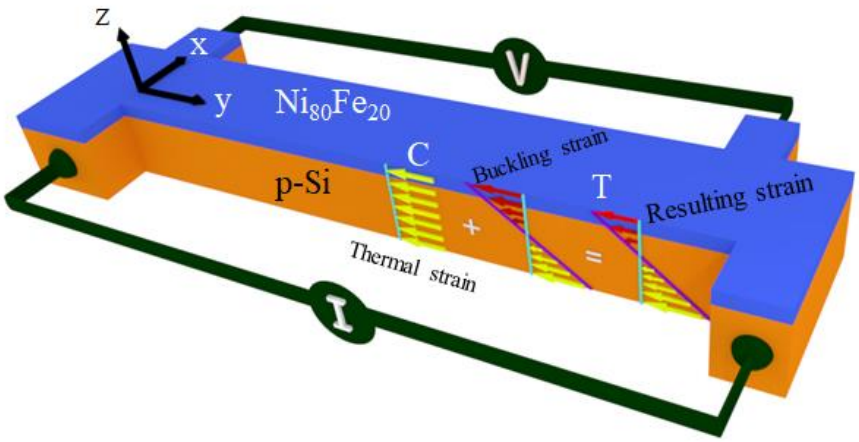

Figure 3.4. Device schematic and experimental setup for crystallographic direction dependent measurements in the yz-plane. The strain gradient due to thermal expansion and buckling and the resulting strain gradient from them is also shown. C denotes compression and T denotes tension.

Transport Characterization

Experiments on the crystallography devices were performed in Quantum Design's Physical Properties Measurement System (PPMS). The MR and $V_{2\omega}$ studies were measured by applying an alternating current (AC) using Keithley 6221 current source through the

outer two electrodes and using Stanford Research Systems SR830 lock-in amplifier to acquire the responses generating through the inner two electrodes.

3.3 Result

To estimate strain in the Si near the interface, buckling deformation was first measured on the 600 μm long Si beam and residual stresses was estimated. At this sample length, the strain and strain gradient would be large enough to quantify. When Si beam was made freestanding, the control specimen buckled due to residual stress as shown in Figure 3.5. This buckling of the beam clearly corroborated the existence of a strain gradient. The deflection was measured to be 8.73 μm. The buckling in the plane of thin film requires large stresses (~>4 GPa). The Si device layer in Si on insulator (SOI) wafers do not have such large residual stresses. The in-plane buckling arose due to the HFVE process used to make the specimen freestanding. As the oxide was etched laterally (along width), the stress relaxation lead to in-plane buckling since thin oxide layer (along the width direction) did not allow out of plane deformation. The buckled beam is the proof of strain gradient in our sample.

The high-resolution transmission electron microscope (HRTEM) was used to study the interfaces and strain in the thin film. MgO and then $Ni_{80}Fe_{20}$ thin film layers were deposited on Si beam for HRTEM to estimate strain. A tensile strain of 4% near the interface was estimated as shown in Figure 3.6 (a). The intensity profile along <110> direction was plotted as shown as shown in Figure 3.6 (b). Using Gaussian fit, each peak was identified followed by peak to peak distance and average over multiple measurements

were carried out. This analysis was carried out near the interface and away from the interface. This calculated stress is less than the fracture stress of single crystal Si. While the strain was estimated for very small region of the thin film, the symmetry of the beam bending helped in estimating the strain gradient. It is noted that the HRTEM sample preparation may release some of the stresses leading to underestimation of strain. The HRTEM image also shows the presence of a native oxide (~3.7 nm) in spite of Ar milling. However, the oxygen deficient native oxide will have dangling bonds and pinholes that allow spin dependent electron tunneling and indirect exchange interactions required for transport studies. To verify Ni or Fe diffusion into Si layer, energy -dispersive X-ray Spectroscopy (EDS) analysis and elemental mapping were obtained in the STEM as shown in Figure 3.7 (a) and (b). The resulting data did not show existence of any measurable Ni or Fe diffusion in Si layer. Elemental map of O corresponds to SiO_2 insulator layer that isolates the device Si layer from handle Si layer.

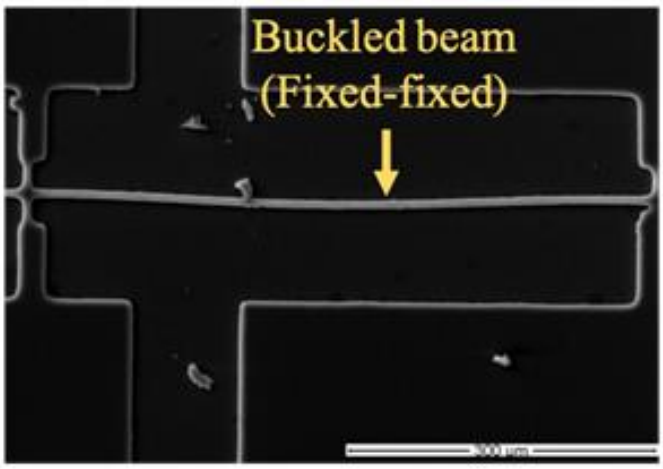

Figure 3.5. The buckling of Si beam due to residual stresses.

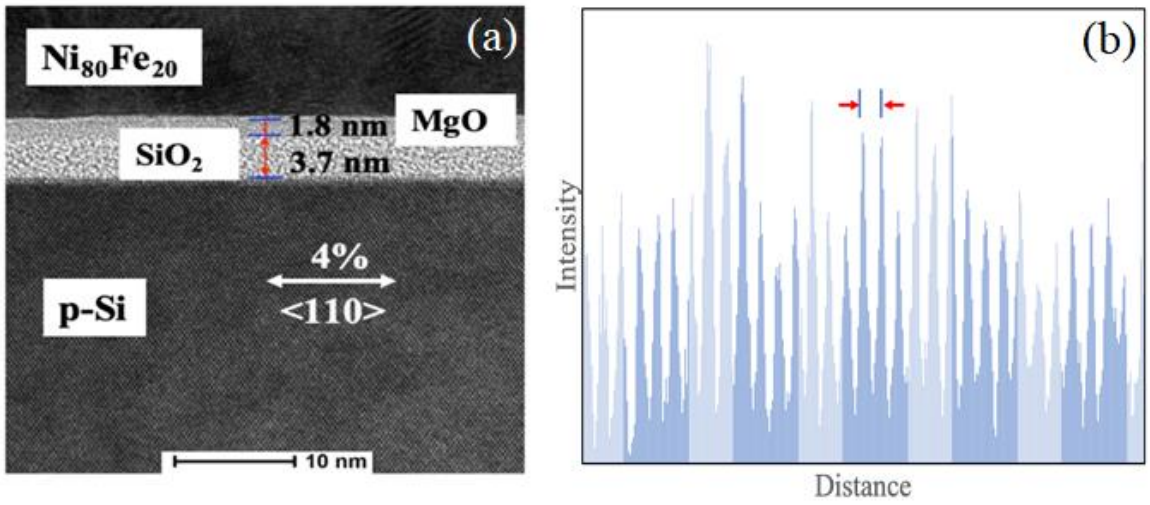

Figure 3.6. (a) High resolution transmission electron micrograph showing the thin film structure at the Si interface and the estimated strain in <110> direction, and (b) The intensity profile along <110> direction used to identify the strain.

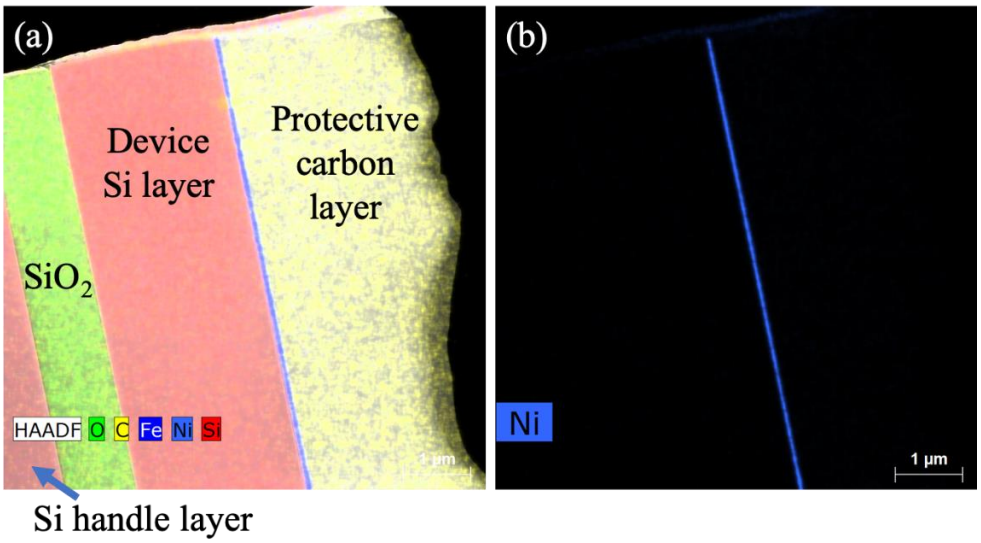

Figure 3.7. The EDS elemental mapping showing (a) the elemental distribution of Si, O, Ni, Fe and C across the $Ni_{80}Fe_{20}$/MgO/p-Si heterostructure, and (b) elemental distribution of Ni. The C layer is used for protection during FIB sample preparation.

The next step was to understand the effect of the ~4% tensile strain near the interface. To observe the effect of applied strain on Si band structure, ab initio calculations

of bulk silicon were carried out using density functional theory (DFT) with a projector augmented wave method [105] and the Perdew-Burke-Ernzerhof (PBE) type generalized gradient approximation [106, 107], as implemented in the Vienna ab initio simulation package (VASP) [108, 109]. Strain was applied along <001> and <110> directions. The Monkhorst-Pack [110] scheme was used for the integration of the Brillouin zone with a k-mesh of 14 Å~ 14 Å~ 14 for the bulk structures. The energy cutoff of the plane wave basis is 300 eV. All of the electronic band structure calculations included spin-orbit coupling. The applied strain lifted the degeneracy of the valence band maxima resulting in a strain mediated valence band splitting. A 4% tensile strain applied along <001> direction led to an energy splitting of 317.3 meV in the valence band as shown in Figure 3.8 (a) and for compressive strain, the splitting increased to 412 meV as shown in Figure 3.8 (b). Similarly, along <110>, an applied 4% tensile or compressive strain led to valence band splitting of ~520 meV or 600 meV respectively as shown in Figure 3.9 (a-c). Applied strain has a significantly larger effect on the valence bands than on the conduction bands as shown in Figures 3.8 (b) and 3.10.

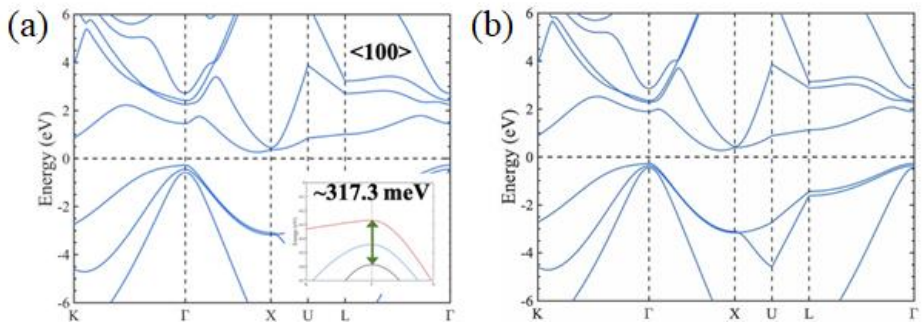

Figure 3.8. Band structure of Si (a) for 4% tensile strain applied along <100> and inset showing the energy splitting at the peak of valence band, and (b) for 4% compressive strain applied along <100>.

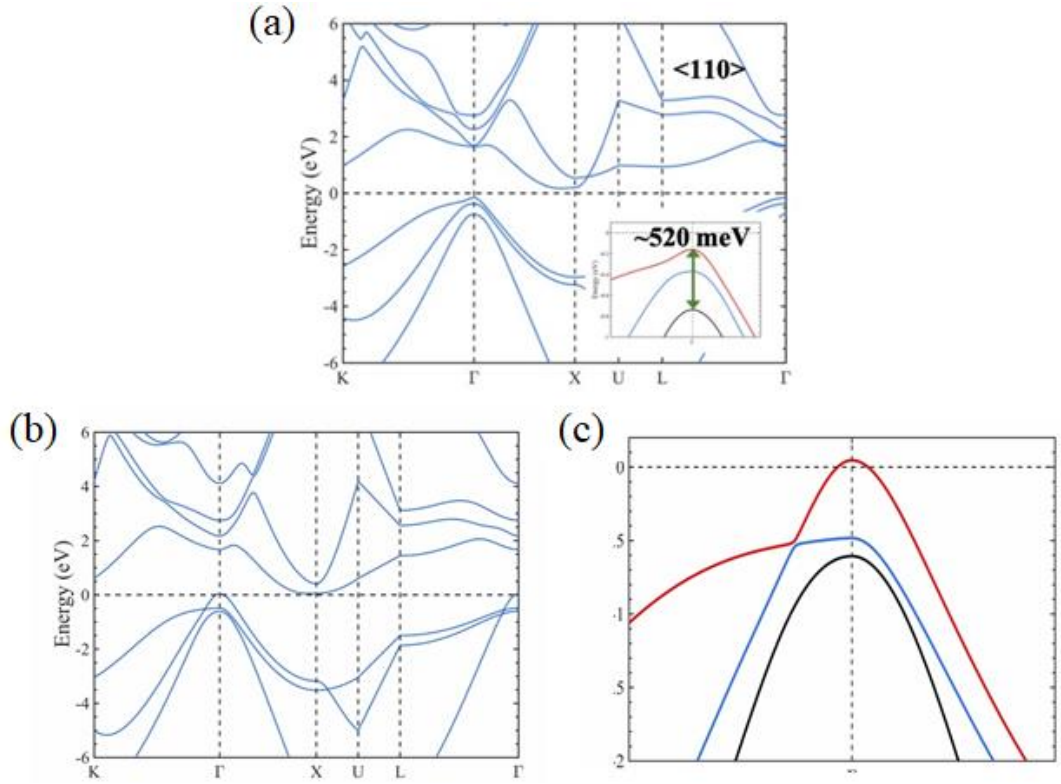

Figure 3.9. The band structure of Si for (a) 4% tensile strain applied along <110>. Inset showing the energy splitting at the peak of valence band, (b) 4% compressive strain along <110>, (b) the valence band maxima at 4% compressive strain along <110> direction.

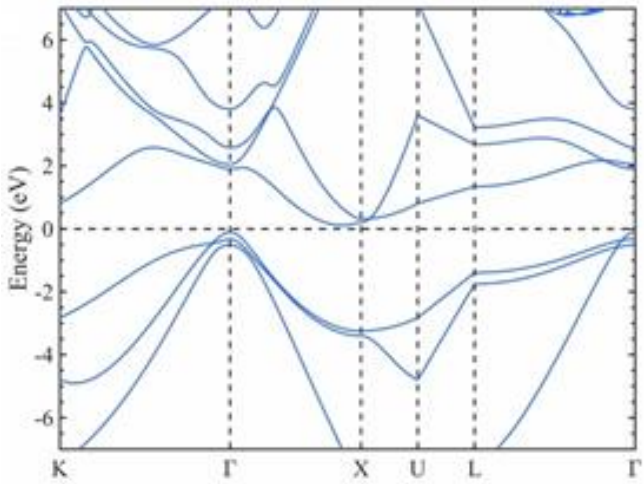

Figure 3.10. Band structure of Si under 2% applied compressive strain along <100>.

From DFT simulations, it was observed that the valence band splitting due to strain in the <110> direction was different from that due to strain in the <100> direction. The symmetry of <110> strained Si will be lower than the <100> strained Si [111], which would give rise to a crystallographic direction dependent behavior. To ascertain this, a set of $Ni_{80}Fe_{20}$ (25 nm) / MgO (1 nm) / p-Si (2µm) multilayer structures were fabricated with the longitudinal direction of the Si layer lying along <110>, and at 15^o, 30^o and 45^o with respect to <110> as shown in Figure 3.2. Magnetoresistance (MR) measurements were performed to uncover the crystallography direction dependent spin polarization as shown in Figure 3.11 (a-d). 0.5 mA of current was applied along the Si channel at 5 hz when the field was swept from 3T to -3T at 300K. The negative MR for the Si channel oriented along <110> has two kinks due to changes in slope indicated by the arrows as shown in Figure 3.11 (a).

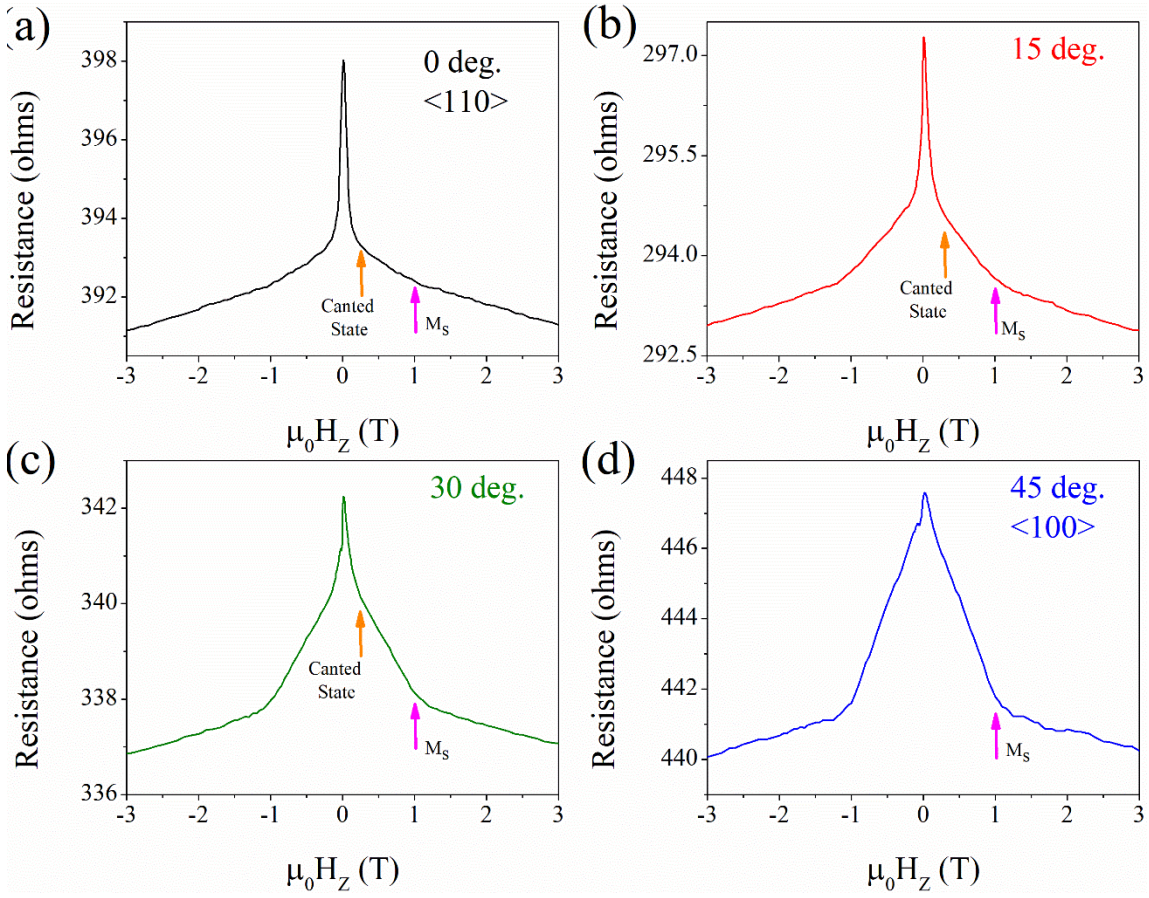

Figure 3.11. The magnetoresistance for an applied out of plane magnetic field for current applied (a) along <110> direction or along the flat of the Si (100) wafer, (b) at 15º to the <110> direction, (c) at 30º to the <110> direction and (d) along <100> direction. Arrows showing saturation magnetization and possible canted states and its transition as a function of orientation.

The kink at higher magnetic field (~1.1 T) corresponds to the change in slope at the saturation magnetization (M_s). The kink at low field (~0.2 T) is not expected for a $Ni_{80}Fe_{20}$ thin film hard axis magnetization. This kink could only arise due to spin dependent tunneling across the oxide barrier. The low field kink gradually shifted towards zero-field for 15˚ and 30˚ samples (Figure 3.11 (b) & (c), respectively) and it disappeared for measurement along <100> direction or at 45 degrees from <110>, as shown is Figure 3.11

(d), which indicated the changes in the spin dependent interactions between the $Ni_{80}Fe_{20}$ and the Si layers. The negative MR behavior arises from polycrystalline $Ni_{80}Fe_{20}$ thin film and the observed correlation of the MR with the Si layer crystallographic direction will not arise if there are no spin dependent tunneling and interactions between $Ni_{80}Fe_{20}$ and Si. This measurement gives proof that exchange interactions were taking place in spite of thick oxide layer (MgO). We have demonstrated that the spin dependent interactions are function of crystallographic direction of p-Si layer.

3.4 Discussion

There are various mechanisms that can give rise to spin polarization in Si. From experimental magnetoresistance measurements, we demonstrate that inhomogeneous strain is the macroscopic cause of the direction dependent spin polarization in p-doped Si. Microscopically, inhomogeneous strain can be thought of as a pathway for the $Ni_{80}Fe_{20}$ and p-Si to interact with each other which can give rise to the observed low-field kinks in the magnetoresistance behavior. Recently, Lou et al.[112] demonstrated spin-phonon interactions leading to a change in thermal conductivity in both p-Si and n-Si [51, 53]. While the charge carriers in p- and n-doped Si are different, the thermal transport is phonon mediated in both cases. IT can be speculated that spin dependent electron-phonon scattering may also give rise to the observed spin polarization behavior. In order to uncover the mechanistic origin of the behavior, we measured the transverse spin-Nernst effect (SNE) in p-Si [113, 114] shown in Figure 3.13 (a-d). While the magneto-thermal transport measurement showed transverse SNE behavior in the measurements, experimental results are inconclusive. A dedicated study on SNE in our system will be on the next chapter.

However, these measurements do indicate the existence of interlayer spin-phonon coupling. In heavy metals, mechanistic reason for both phenomena such as SHE and SNE is large SOC [115]. However, that is not true for Si where thermal transport is mediated by phonons as opposed to charge carriers. Microscopically, spin dependent interactions with phonons cause crystallography dependent spin polarization. And, an inverse microscopic behavior occurs during thermal transport where phonons have spin dependent interactions with charge carrier and give rise to transverse spin current or SNE. Hence, a strain mediated spin dependent coupling between phonon and charge carrier is proposed to be the microscopic mechanism for spin polarization observed in this study.

3.5 Conclusion

This study presents an experimental evidence of inhomogeneous strain mediated spin-phonon coupling in centrosymmetric non-magnetic material [116]. The spin-dependent interactions and resulting spin polarization may be applicable to all diamond cubic semiconductors (GaAs, Ge, InSb etc.) under inhomogeneous strain. Manufacturing processes for strain engineering already exist not only for Si but also for other semiconductors. Topological behavior can also arise from the inhomogeneous strain fields, which may also open simple materials systems for topological materials research irrespective of intrinsic spin-orbit coupling. In addition to proposed experimental studies, theoretical models that describe the spin-phonon coupling in centrosymmetric materials and resulting behavior also need to be developed. This work provides a starting point for such future studies.

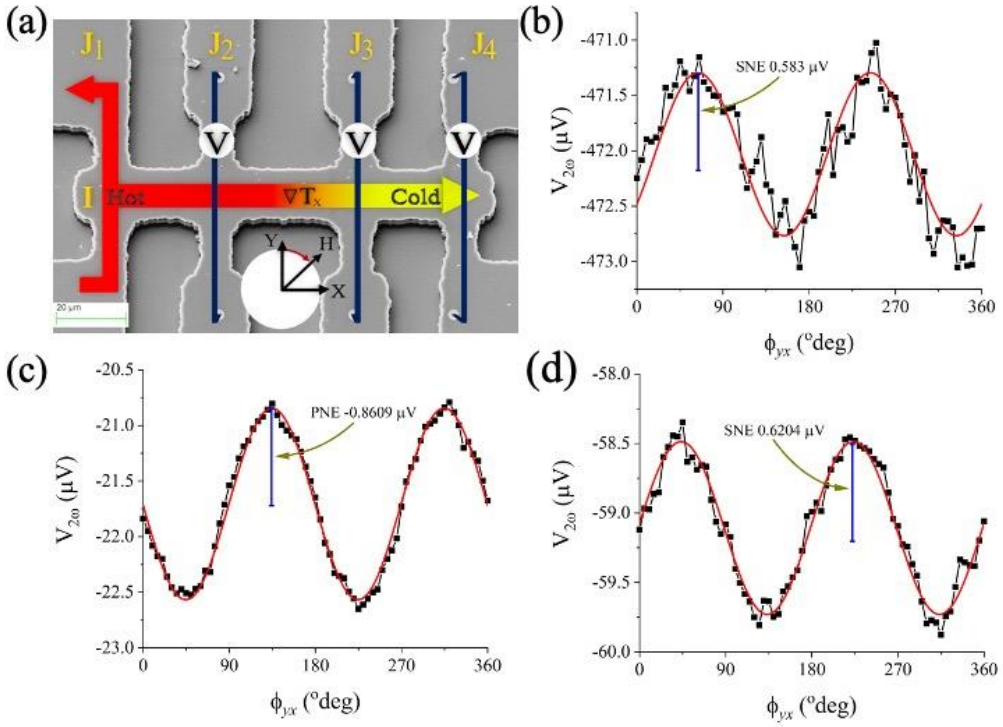

Figure 3.12. The magneto-thermal transport characterization of p-Si thin film sample. (a) a representative scanning electron microscope image showing the schematic of experimental setup for SNE measurement and the angle dependent magneto thermal transport measurement in *yx*-plane for an applied magnetic field of 1 T at Hall junctions (b) J2, (c) J3 and (d) J4 showing SNE, PNE and SNE responses respectively. Red line is curve fit.

Chapter 4 Spin Nernst Effect in Silicon

4.1 Introduction

Recent experiments have demonstrated a new method for spin current generation through spin Nernst effect (SNE) [115, 117-119], which is a thermal analog of the spin Hall effect (SHE). SNE creates a transverse spin current relative to the temperature gradient without the presence of an applied magnetic field. The SNE has been experimentally reported in materials with large intrinsic spin orbit coupling such as Pt, W and Ta, which arises due to spin dependent scattering in electronic transport. In contrast to electrons, phonons are neutral quasi-particles and usually do not carry angular momentum, especially in non-magnetic materials. However, phonons have been proposed to contribute towards transverse spin current due to phonon skew scattering [120]. Analogous to SHE and SNE, phonon Hall effect has been proposed and experimentally reported in paramagnetic dielectrics and magnetic solids [121-123], which may arise due to phonon Berry curvature or magnon-phonon coupling. We hypothesized an alternate mechanism where spin dependent electron-phonon coupling in non-magnetic materials would give rise to spin redistribution and transverse spin current. In such a case, phonon transport will give rise to phononic SNE as shown in Figure 4.1. However, no experimental evidence of phononic SNE has been reported so far. Recently, Lou et al. [124] experimentally demonstrated anisotropic magneto-thermal transport behavior at room temperature in p-Si due to spin-phonon coupling [125]. The spin-phonon coupling is an essential requirement for observation of phononic SNE. In a recent work, Lou et al. [126] demonstrated large SHE

[53, 127] behavior in Si at room temperature, which was attributed to spin-phonon coupling and strain gradient. It reported the spin-Hall angle to be an order of magnitude larger than Pt and of the same order as topological insulator surface states. This was the motivation to undertake a magneto-thermal transport characterization method to uncover spin dependent thermal transport in Si. This study reports observation of phononic SNE in freestanding $Ni_{80}Fe_{20}$/MgO/p-Si thin film structure. The hypothesis of the study was that the phonon transport in Si would lead to transverse spin current due to spin-phonon interactions as shown in Figure 4.1.

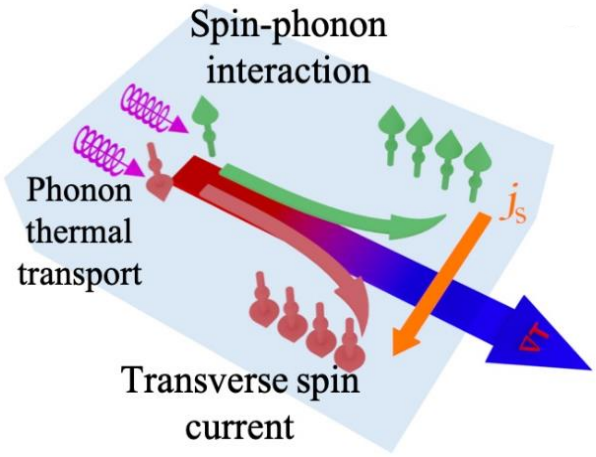

Figure 4.1. Scheme of the hypothesis showing the spin-Nernst effect behavior due to spin-phonon interactions for the temperature gradient along *x*-axis.

4.2 Method

Spin transport phenomena are often demonstrated in bilayer structures composed of a heavy metal (HM) and a ferromagnet (FM) where the heavy metal generates a transverse spin current, either through charge or temperature gradient. The rotation of the applied magnetic field leads to modulation in resistance and thermopower for charge and thermal transport, respectively. Spin-dependent transport can be studied in either

longitudinal or transverse measurement configuration. Transverse magneto-thermal transport measurement configuration was chosen for this study because it captured contributions from the planar Nernst effect (voltage) response arising from the ferromagnetic ($Ni_{80}Fe_{20}$ in this study) layer in addition to SNE from the non-magnetic layer (p-Si in this study) since both have $\sin 2\theta$ symmetry ($\propto m_x m_y$, where m_x and m_y are magnetization vectors along x and y-axis, respectively). Longitudinal anisotropic magneto thermopower and thermal effects, because of anisotropic magnetoresistance, may also play a role and both have a symmetry behavior of $\sin^2\theta$ [39]. There is no known method of characterizing SNE other than via measuring voltages. Spin current in silicon can be characterized by so called Hanle effect [128] that produce a decay of the net spin accumulation due to spin precession in a magnetic field perpendicular to the electron spins in the Si.

Device Design

The Hall bar design with independent junctions was chosen to conduct the experiments because it comprises of a specimen with four electrodes placed transversely across the length of the specimen which would give us the freedom to apply the current and measure the transverse signals at different locations to prove our hypothesis. Thus, in this design, depending on the object of the experiment, by applying current source and placing a voltmeter in certain electrodes, family of Hall and Nernst effects can be measured, such as ordinary Hall effect (OHE), anomalous Hall effect (AHE), planar Nernst effect, anisotropic magneto-thermopower, spin Nernst effect, and non-local resistance. This configuration can also be made freestanding if heat loss to the sink needs to be eliminated.

Device Fabrication

The freestanding Hall bar device composed of Pd (1 nm)/ $Ni_{80}Fe_{20}$(25 nm)/MgO (1.8 nm)/ SiO_2 (native)/p-Si (2 μm) was fabricated using standard cleanroom techniques. Figures 4.2 (a-f) illustrates the general fabrication procedures resulting in freestanding specimen. Commercially acquired silicon-on-insulator (SOI) wafer was used to fabricate the Hall bar. General cleaning and resist stripping procedures, similar to four-terminal device fabrication (Section 2.2), were followed. An SOI wafer (Figure 4.2 (a)) was cleaned, and spin coated with S 1813 resist. Full Hall bar device structure was patterned on the wafer by UV lithography. Si from the device layer surrounding the Hall bar was exposed after development of the positive resist as shown in Figure 4.2 (b). Patterned SOI wafer was then mounted on a carrier wafer and placed inside the DRIE system to etch out the 2 μm device layer, hence exposing the SiO_2 box layer as shown in Figure 4.2 (c), followed by stripping the resist from the wafer by dipping it in acetone bath and rinsing with IPA and water (Figure 4.2 (d)). The box layer was removed with the help of HFVE to make the p-Si layer freestanding as shown in Figure 4.2 (e). Evidence of freestanding sample is shown in Figures 4.3 (a) & (b). The SEM micrograph shows the oxide layer underneath the sample area etched using HFVE in Figure 4.3 (a). The etch contrast in the freestanding sample area and undercut at electrodes and connecting arms, shown in Figure 4.3 (b), further confirms the existence of freestanding device because the undercut in oxide layer is essential for making the sample freestanding. The wafer was then placed inside a sputter chamber where Argon ion milling was first performed to get rid of the native SiO_2 on the p-Si device layer, however, some (1.8 nm) native oxide was still there. Argon mill was

followed by deposition of 1.8 nm of MgO layer (to eliminate Ni or Fe diffusion into p-Si and act as a tunnel barrier) and 25 nm of $Ni_{80}Fe_{20}$ layer. At the end, 1 nm Pd was deposited to prevent the $Ni_{80}Fe_{20}$ layer from oxidizing (Figure 4.2(f)). A representative device structure is shown in Figure 4.4. There are four independent Hall junctions (eight terminals) named as J1, J2, J3 and J4. The width of the central beam was ~15 µm and that of the electrodes was ~9 µm. The center to center length of the sample was ~100 µm. Applied magnetic field is rotated in yx plane (in plane).

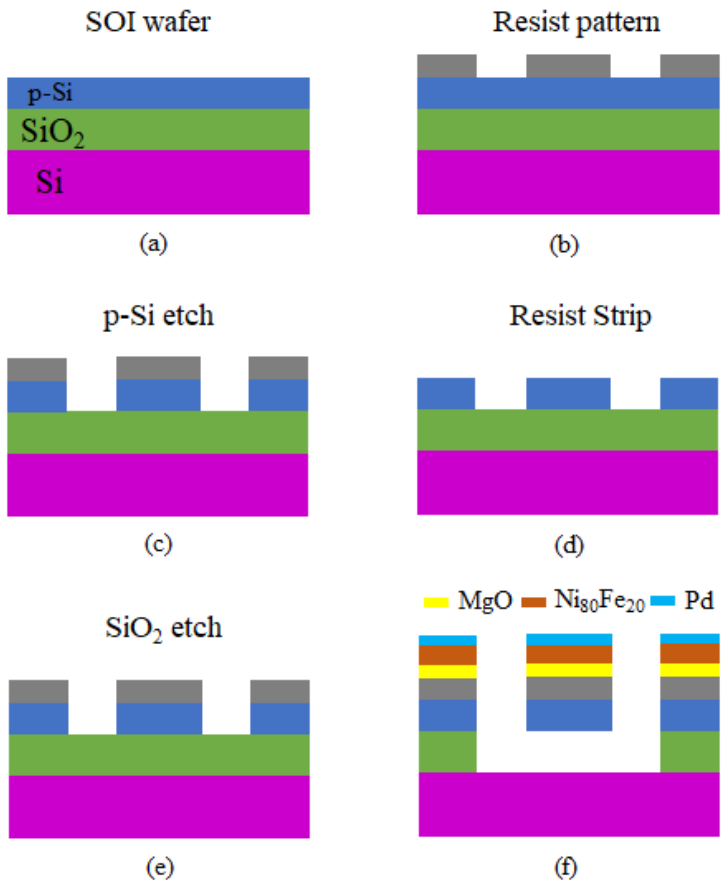

Figure 4.2. Fabrication procedure of SOI hall bar device for SNE experiment.

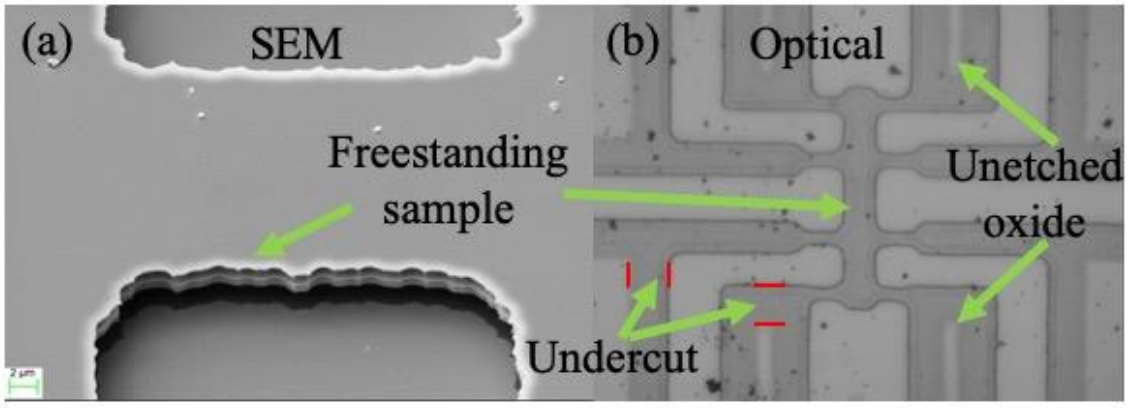

Figure 4.3. (a) & (b) SEM micrographs that proves the existence of a freestanding device structure. Scale bar is 2 μm in (a).

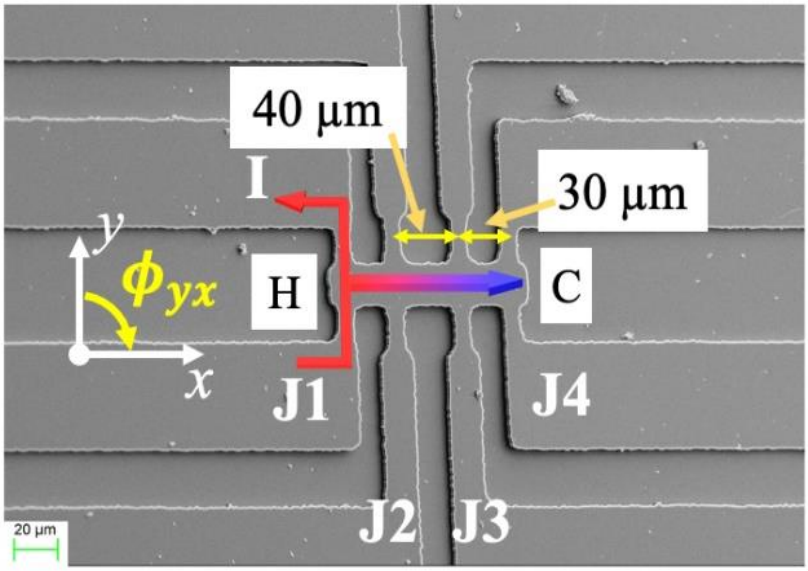

Figure 4.4. A representative scanning electron microscope image showing the structure of the experimental device, its dimensions, and experimental scheme. Scale bar is 20 μm.

Heating one of the Hall junctions would create a temperature gradient across the length of the sample as shown in Figures 4.5 (a & b). Junctions J1 and J4 were heated to have temperature gradient flow in +x and -x directions, respectively. Then, angle dependent transverse thermal response across the three Hall junctions were measured and used to

identify SNE response. Transverse thermal response measurements were performed inside the Quantum Design's Physical Properties Measurement System (PPMS) at 300 K. The measurements were acquired using Keithley 6221 (current source) and Stanford Research System SR830 lock-in amplifier. In the experimental measurement, an alternating current (I) of 2 mA across the (heater) junction J1 was applied to create a temperature gradient, $+\nabla T_x$, along the specimen length (x-axis) as shown in Figure 4.5 (a). To minimize thermal fluctuations and thermal drift, wait times were set for 90 minutes after applying current and 30 minutes after switching on the magnetic field, before finally acquiring the data. Transverse $V_{2\omega}$ responses were recorded at the other three junctions (J2, J3 and J4) while the specimen was rotated under a constant applied magnetic field of 1 T in the *yx*-plane. The measurement was then repeated by heating junction J4 and acquiring transverse $V_{2\omega}$ responses at the other three junctions (J1, J2 and J3) (Figure 4.5 (b)).

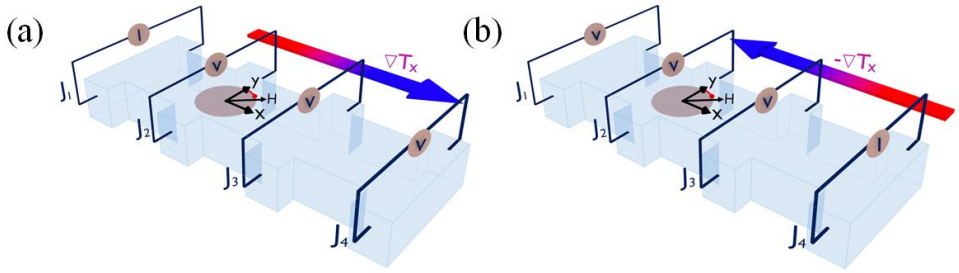

Figure 4.5. The schematic of angle-dependent magneto-thermal transport characterization. (a) Schematic showing the heating (I) junction J1 and measurement ($V_{2\omega}$) at junctions J2, J3 and J4. (b) Schematic showing the heating junction J4 and measurement at junctions J1, J2 and J3.

4.3 Results

The acquired transverse $V_{2\omega}$ responses for junctions J2, J3 and J4 are shown in Figure 4.6. Sin 2θ contributions were extracted and the resulting line fit (red) is also shown.

Similarly, the acquired transverse $V_{2\omega}$ responses for junctions J1, J2 and J3, while junction J4 is heated, and their corresponding line fit are shown in Figure 4.7. The $V_{2\omega}$ response data was processed to filter out any base second harmonic voltage response arising in the sample as shown in Figures 4.8 (a) and (b). The amplitudes of the $\sin 2\theta$ angular dependence arising from PNE and SNE contributions are listed in Table 4.1.

A control device was fabricated by inserting 25 nm of SiO_2 in between p-Si and $Ni_{80}Fe_{20}$ layers. After performing the experiments identical to the one performed in Figures 4.6 and 4.7, the resulting PNE responses were recorded as shown in Figures 4.9 and 4.10 and their amplitudes are also listed in Table 4.1. The PNE behavior in $Ni_{80}Fe_{20}$ thin films has been well characterized [113, 129, 130] and the PNE coefficient for $Ni_{80}Fe_{20}$ is reported to be 66-75 nV/K [38, 131, 132]. Using this information, it was found that the PNE response in the control sample were larger than that expected for $Ni_{80}Fe_{20}$. This behavior was attributed to the additional response from self-induced SNE at SiO_2 interface, a behavior similar to self-induced SHE [133, 134]. However, the thermal responses in the $Ni_{80}Fe_{20}$/MgO/p-Si sample are an order of magnitude larger than the control sample, which means these responses are almost three orders of magnitude larger than that expected for PNE behavior. Another control sample with only 2 μm p-Si was fabricated and measured. The resulting V_{2w} response demonstrated a $\cos\theta$ symmetry behavior which corresponds to ordinary Nernst effect (ONE) as shown in Figure 4.11. This proves that the observed PNE response in the $Ni_{80}Fe_{20}$/MgO/p-Si sample are originating due to interactions between $Ni_{80}Fe_{20}$ and p-Si layer and not from $Ni_{80}Fe_{20}$ or Si.

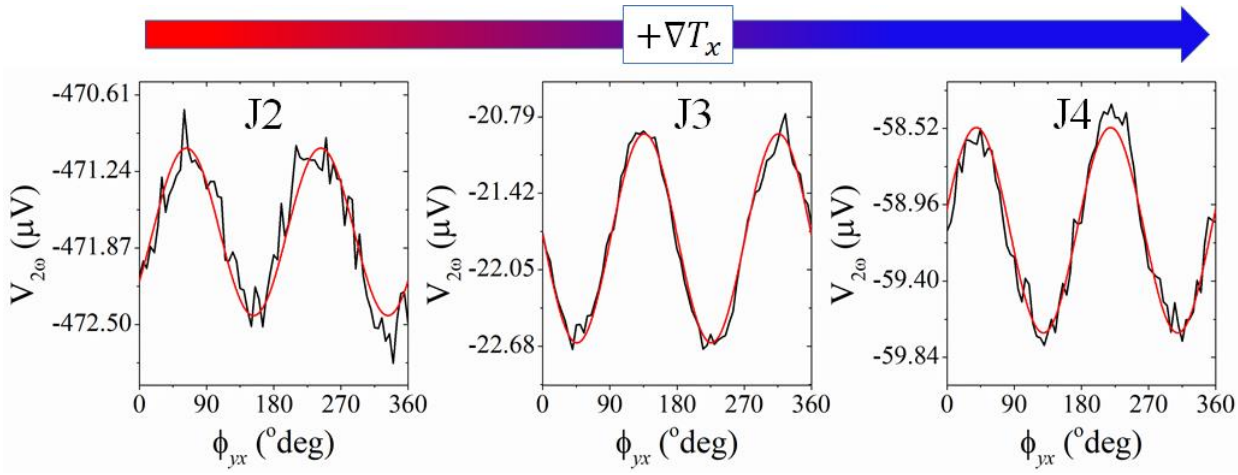

Figure 4.6. The angle-dependent magneto-thermal transport measurement and the line fit (red) at junctions J2, J3 and J4 in the yx-plane at an applied magnetic field of 1 T when junction J1 is heated, giving rise to $+\nabla T_x$.

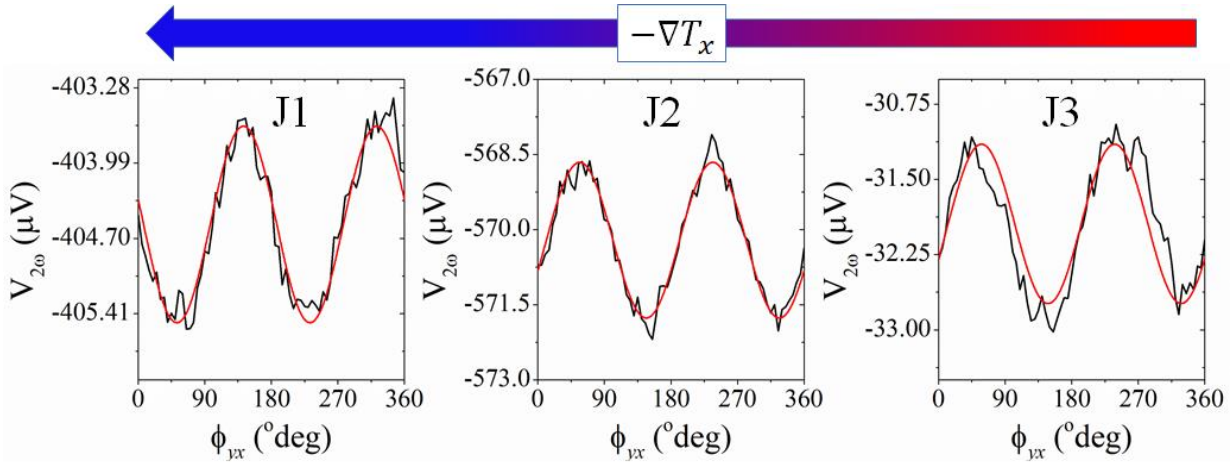

Figure 4.7. The angle-dependent magneto-thermal transport measurement and the line fit (red) at junctions J1, J2 and J3 in the yx-plane at an applied magnetic field of 1 T when junction J4 is heated, giving rise to $-\nabla T_x$.

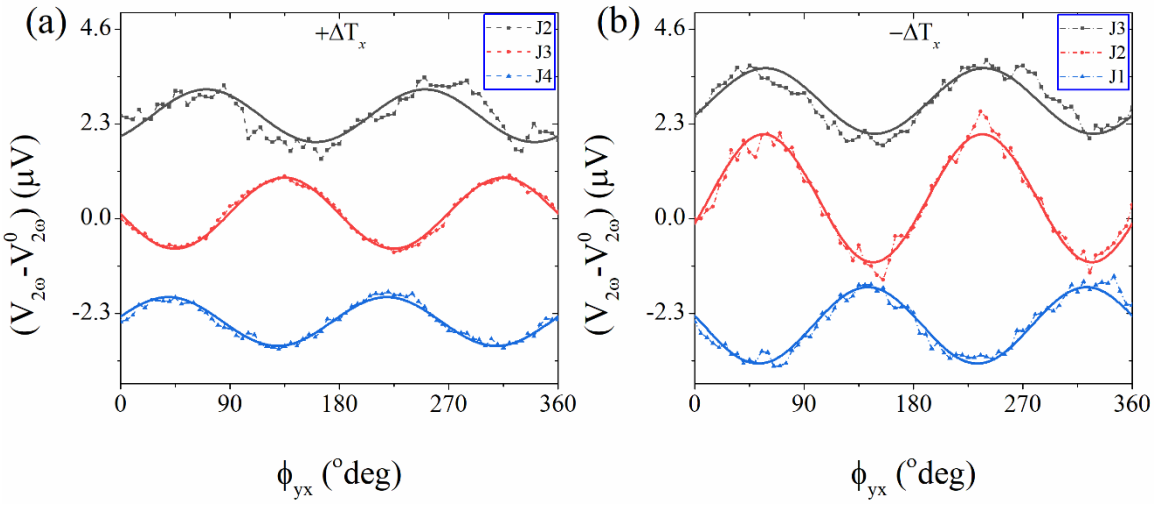

Figure 4.8. The net angle-dependent transverse $V_{2\omega}$ response arising from the in $Ni_{80}Fe_{20}$(25 nm)/MgO (1.8 nm)/ SiO_2 (native)/p-Si (2 μm) sample in the yx-plane at an applied magnetic field of 1 T (a) when junction J1 is heated and (b) when junction J4 is heated.

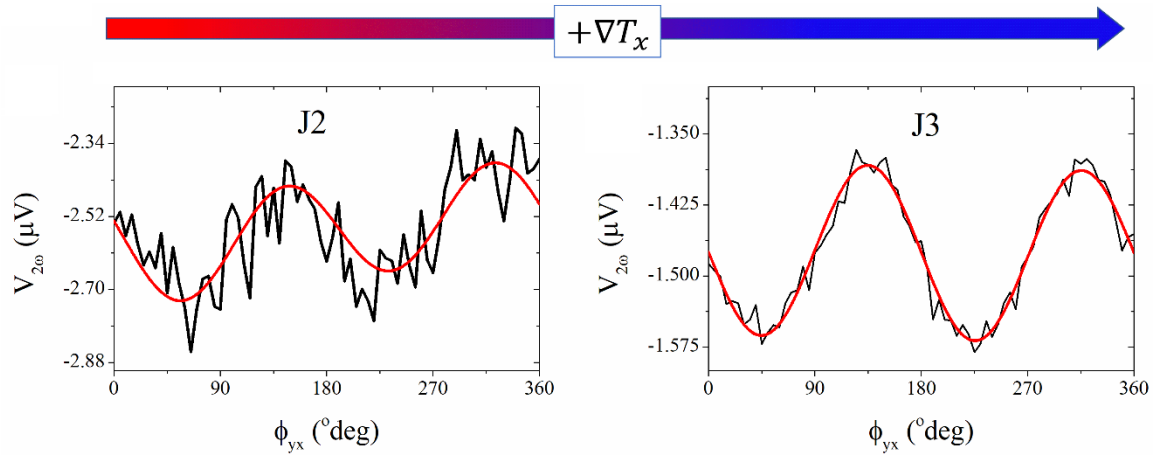

Figure 4.9. The angle dependent transverse thermal response behavior in $Ni_{80}Fe_{20}$ (25 nm)/SiO_2 (25 nm)/p-Si (2 μm) control sample showing the PNE behavior when heating the J1 junction and response measurement at J2 and J3.

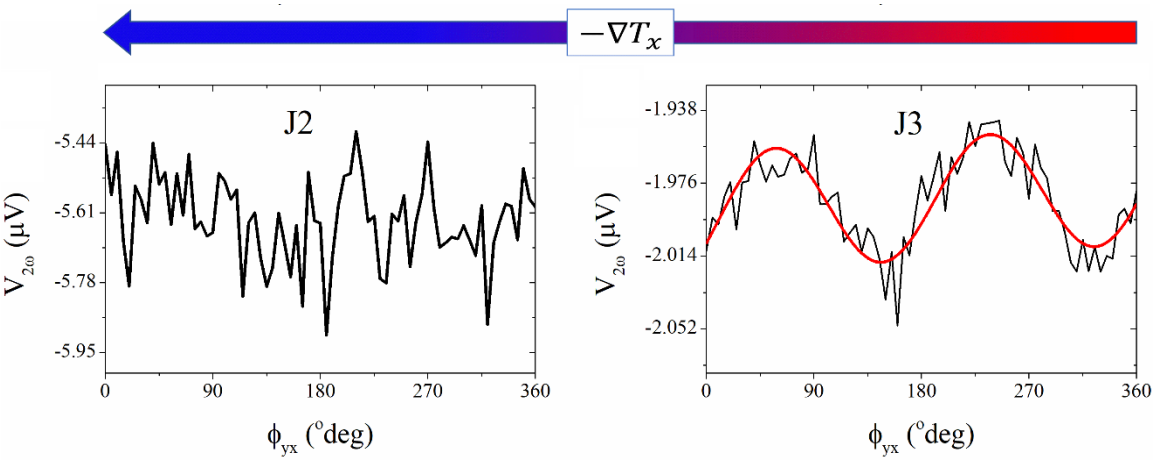

Figure 4.10. The angle dependent transverse thermal response behavior in $Ni_{80}Fe_{20}$ (25 nm)/SiO_2 (25 nm)/p-Si (2 μm) control sample showing the PNE behavior when heating the J1 junction and response measurement at J2 and J3.

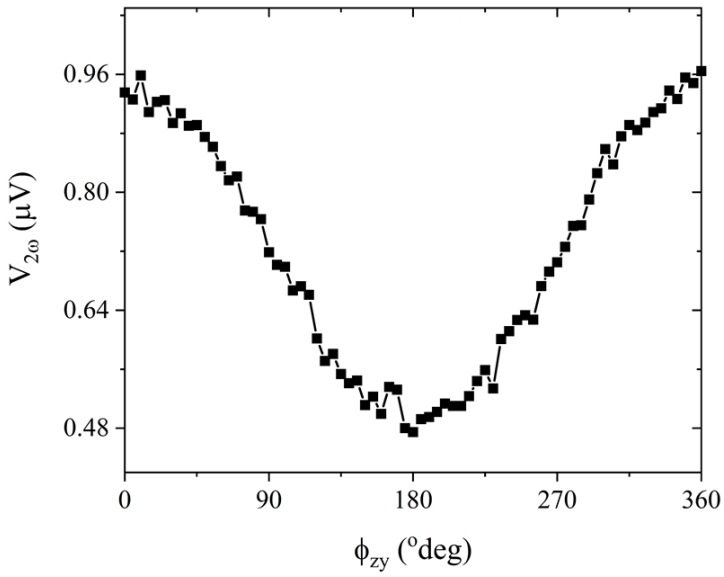

Figure 4.11. The angle dependent transverse thermal response behavior in 2 μm p-Si control sample showing the ordinary Nernst effect behavior when J3 was heated and response was measured at J2.

Table 4.1. The magnitude of the angular modulation in the transverse $V_{2\omega}$ response for direction-dependent thermal transport and the resulting symmetry behavior of the $V_{2\omega}$

Specimen	**Junction**	**J1**	**J2**	**J3**	**J4**
$Ni_{80}Fe_{20}$/MgO/p-Si	Thermal response	Heater ($+\nabla T_x$)	0.5584 µV	-0.859 µV	0.579 µV
	Symmetry		Not PNE	PNE	Not PNE
	Magnitude of Coefficient		3.51 µV/K	16.54 µV/K	36.79 µV/K
	Thermal response (µV)	-0.896 µV	1.427 µV	0.714 µV	Heater ($-\nabla T_x$)
	Symmetry	Not PNE	PNE	PNE	
	Magnitude of Coefficient	45.4 µV/K	27.5 µV/K	5.63 µV/K	
<u>Control</u> $Ni_{80}Fe_{20}/SiO_2$ (25 nm)/p-Si	Response (µV)	Heater ($+\nabla T_x$)	-0.12 µV	-0.085 µV	Not measured
	Symmetry		PNE	PNE	
	Response (µV)	Not measured	negligible	0.0293 µV	Heater ($-\nabla T_x$)
	Symmetry		PNE	PNE	

In addition, the sign of $\sin 2\theta$ symmetry is not constant through the length of the sample. For example, the amplitude of transverse thermal response measured at J2 was 0.5584 µV and 0.579 µV at J4, whereas it was -0.8598 µV at J3 (Table 4.1). If these responses were to originate from $Ni_{80}Fe_{20}$ layer, then all three of them should have a negative sign. Moreover, the amplitude should have decreased at J3 and J4 since they were farther from the heat source. Similar behavior was observed when the sample was heated at J4: the magnitude at J2 was larger than that of J3, which was closer to the heat source

and had larger temperature gradient. A COMSOL model was set up to replicate the experiments. Current of 2 mA was applied at junction J1 as shown in Figure 4.12 (a) and the resulting temperature gradients were recorded as shown in Figure 4.12 (b). The temperature gradients from the heat source were estimated to be 10.59 K/mm, 3.46 K/mm and 1.05 K/mm between junctions J1-J2, J2-J3 and J3-J4, respectively. The COMSOL model was verified using infra-red (IR) thermal imaging. In the IR imaging the sample did not show any temperature increase for 2 mA of current as shown in Figure 4.13 (a), which was attributed to heat loss to air. So, in place of that, a $Ni_{80}Fe_{20}$ (25 nm)/MgO (1.8 nm)/p-Si (2 µm) composite sample device (fabricated with procedures described in Section 2.2) with back side etched was used. The heat loss to air in this sample will be insignificant because there was no heat sink underneath the sample (handle layer etched) (Figure 4.13 (b)). Thermal conductivity was estimated to be 90-100 W/mK using finite element model in COMSOL, which is consistent with values reported over the years and helped us to verify the model. Hence, the temperature distribution predicted using finite element model in Figure 4.12 is correct. Using the temperature gradients, the transverse thermopower coefficient was estimated using $S_{xy} = \frac{\Delta V_{xy}}{\mathrm{w}\cdot\nabla \mathrm{T}_x}$, where S_{xy}, ΔV_{xy}, w and $\nabla \mathrm{T}_x$ were transverse thermopower coefficient, amplitude of transverse thermal voltage, width and temperature gradient, respectively. These values lie between 3.5 µV/K to 45.4 µV/K as shown in Table 4.1. In comparison, the spin-Nernst coefficient estimated for Tungsten (W) is 0.3 µV/K [43]. The measured transverse thermopower coefficient values were also larger than the Seebeck coefficient of $Ni_{80}Fe_{20}$ (-7.8 µV/K [135] to -20 µV/K [17]). Hence, this behavior

could not occur in the $Ni_{80}Fe_{20}$ layer. Whereas, the Seebeck coefficient in doped Si thin films can be ~800 µV/K [136] and might give rise to these responses.

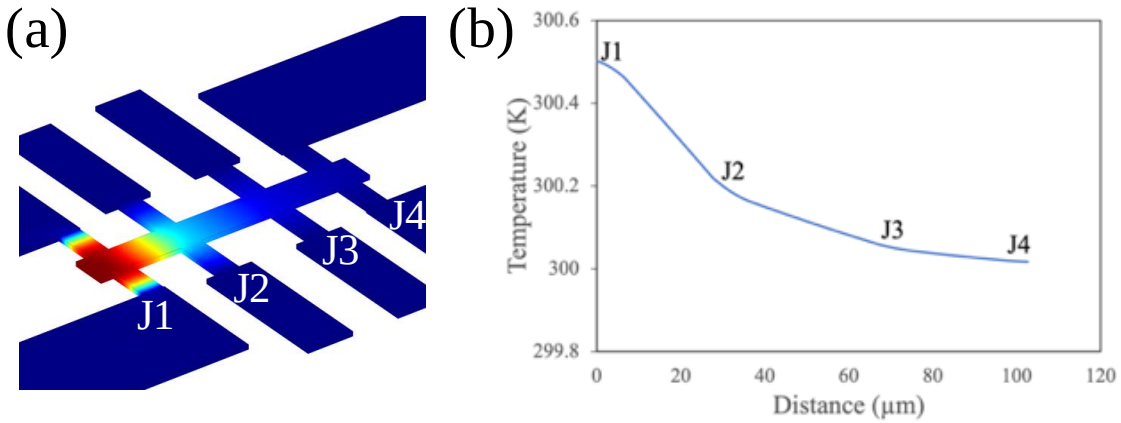

Figure 4.12. (a) The expected temperature distribution across the length of the specimen estimated using COMSOL simulation at 2 mA of current and (b) longitudinal temperature profile for an applied heating current of 2 mA.

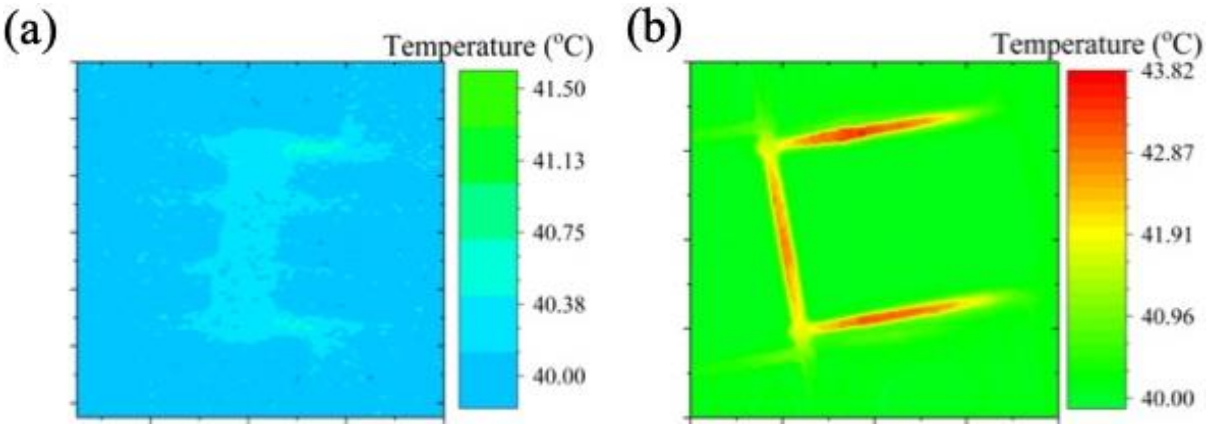

Figure 4.13. The infra-red thermal imaging microscope image showing the temperature profile (a) for 2 mA of longitudinal current in the p-Si hall bar sample, and (b) 2 mA of longitudinal current in a $Ni_{80}Fe_{20}$ (25 nm)/MgO (1.8 nm)/p-Si (2 µm) composite sample.

Among the known mechanisms for the transverse SNE response are spin-dependent electron-phonon scattering, interlayer magnon-phonon coupling [137], and chiral phonons [138]. All of these mechanisms require either bulk inversion asymmetry (BIA) or structural inversion asymmetry (SIA). Diamond cubic Si is centrosymmetric, which makes this

observation of spin dependent thermopower surprising. For such a phenomenon to arise in centrosymmetric Si, there should be an asymmetry between spin relaxation of spin-up and spin-down charge carriers. Si has no magnetic moment and magnetic field dependent behavior could not arise from Si layer. Hence, interlayer coupling with the $Ni_{80}Fe_{20}$ layer was also essential for angle dependent behavior. Before attempting to explain the observed magneto-thermal response, I will discuss additional experiments that were undertaken to uncover the asymmetry in spin relaxation and interlayer coupling.

First, the angle dependent transverse and longitudinal $V_{2\omega}$ responses were measured in yx-plane as a function of magnetic field as shown in Figure 4.14 (a-d). The transverse $V_{2\omega}$ response displayed $\sin 2\theta$ symmetry for junctions J2 and J3 as shown in Figures 4.14 (a) & (b) respectively, but the longitudinal $V_{2\omega}$ response for junctions J23 and J34 displayed a symmetry behavior corresponding to the anisotropic magneto thermopower as shown in Figures 4.14 (c) & (d), respectively. This behavior demonstrated that the p-Si layer is coupled to $Ni_{80}Fe_{20}$ layer because observed $\sin^2\theta$ [39] symmetry cannot arise from p-Si layer only. The angle dependent thermopower was measured to be 1.11×10^{-2}, which was two orders of magnitude larger than spin-Nernst magneto thermopower reported in Pt/YIG system [46]. Similar to the transverse thermopower, this longitudinal measurement also demonstrated the efficiency of spin-phonon coupling and resulting spin current. The measured longitudinal thermal response reduced as the magnetic field was reduced. It suggested that magnons could be the underlying cause of interlayer spin-heat coupling.

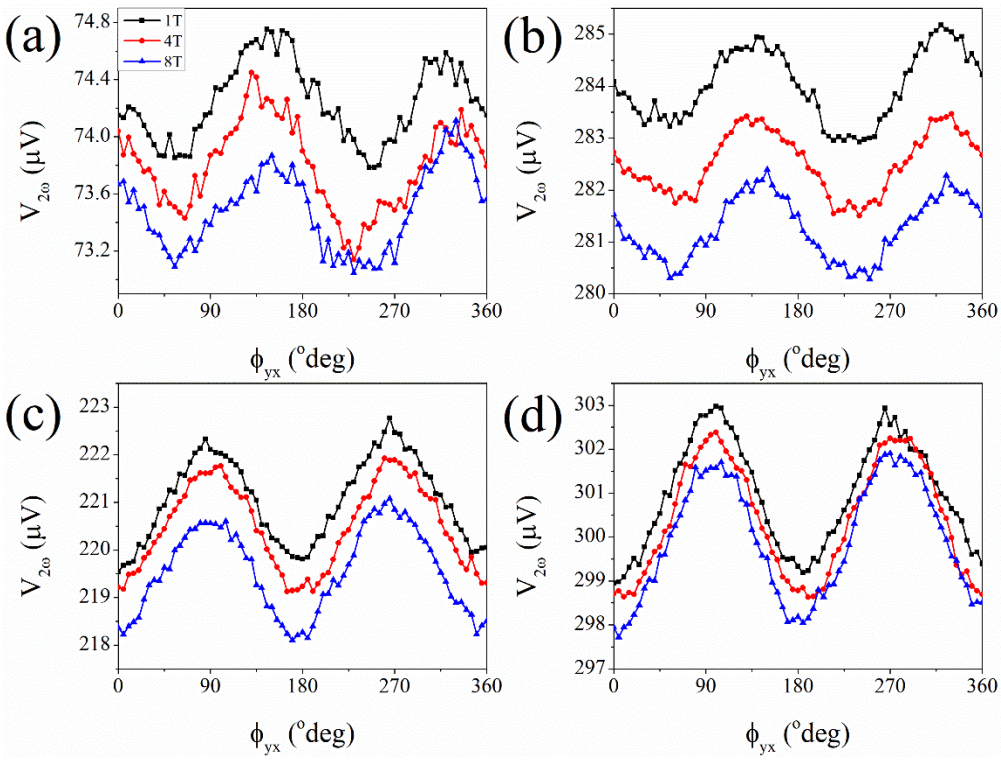

Figure 4.14. (a) The angle dependent longitudinal magneto-thermopower response in yx-plane at 1 T, 4 T and 8 T in the composite p-Si sample for junctions (a) J2, (b) J3, (c) J23, and (d) J34.

To further explore the interlayer coupling and its relationship to strain (as hypothesized), Hall effect measurements were undertaken as a function of current as shown in Figure 4.15. From these measurements, the anomalous Hall resistances (R_{AHE}) were estimated to be 10.81 mΩ, 7.98 mΩ and 6.9 mΩ at 0.5 mA, 5 mA and 10 mA, respectively as shown in Table 4.2. The temperature rise due to 10 mA of current was not expected to be more than 25 K. The decrease in R_{AHE} while increasing the applied current is intriguing. There are three known mechanisms through which the anomalous Hall effect arises [41]: Intrinsic deflection, which is dependent on the band structure and comes from the Berry phase; Side jump scattering, which comes from deflection of electrons in opposite direction due to opposite electric field experienced before and after the site of an impurity; and skew

scattering which originates from impurity scattering due to effective spin orbit coupling. If the conductivity of a FM metal ranges from 10^4 – 10^6 S/m, then intrinsic mechanism is the dominant mechanism for AHE. The conductivity of $Ni_{80}Fe_{20}$ employed in this work falls in that range. We hypothesized that by bringing p-Si in contact with $Ni_{80}Fe_{20}$, we are introducing interlayer spin-phonon coupling. The sign of anomalous Hall effect coming from the intrinsic mechanism is positive whereas that from skew scattering mechanism is negative [139]. We hypothesized that as the current increases, the thermal expansion mismatch will increase the strain gradient in the freestanding sample. This would change the spin-phonon interactions and lead to increase in skew scattering part which is responsible for decrease in R_{AHE} from 10.81 mΩ to 6.9 mΩ as shown in Table 4.2. Similar change in sign of AHE has been observed in Mn_xSi_{1-x}, when it was brought near n-Si which was attributed Rashba spin orbit coupling between Mn_xSi_{1-x} and n-Si layers [140]. The applied strain in Si sample would also change the mobility (μ) of charge carriers. The increased strain was confirmed from decrease in transverse resistance [141-143] as shown in Figure 4.15. This strain mediated behavior was also confirmed by the increase in Hall resistance (R_H) and, in turn, increase in mobility $\left(\mu = \frac{R_H}{\rho}, \rho - resistivity\right)$ as a function of current, as shown in Table 4.2. The $Ni_{80}Fe_{20}$ resistivity is $\rho_{Ni_{80}Fe_{20}} = \sim 6.4 \times 10^{-7}$ Ωm and p-Si is $\rho_{p-Si} = \sim 5 \times 10^{-5}$ Ωm [124, 126]. As hypothesized, the strain and strain gradient should also break the symmetry of spin-up and spin-down charge carriers' relaxation due to asymmetric spin-phonon relaxation. We observed that the R_H for the up-spin $\left(R_H^{\uparrow}\right)$(slope at positive magnetic field) and down-spin $(R_H^{\downarrow})$(slope at negative magnetic field) charge carriers was asymmetric as shown in Table 4.2. The difference was

approximately ten percent. This difference could only arise due to asymmetric spin-phonon relaxation, which is believed to be the cause of spin accumulation and reduced R_{AHE} as a function of current. Thus, the Hall effect measurements confirmed the existence of interlayer coupling and asymmetric spin-phonon coupling.

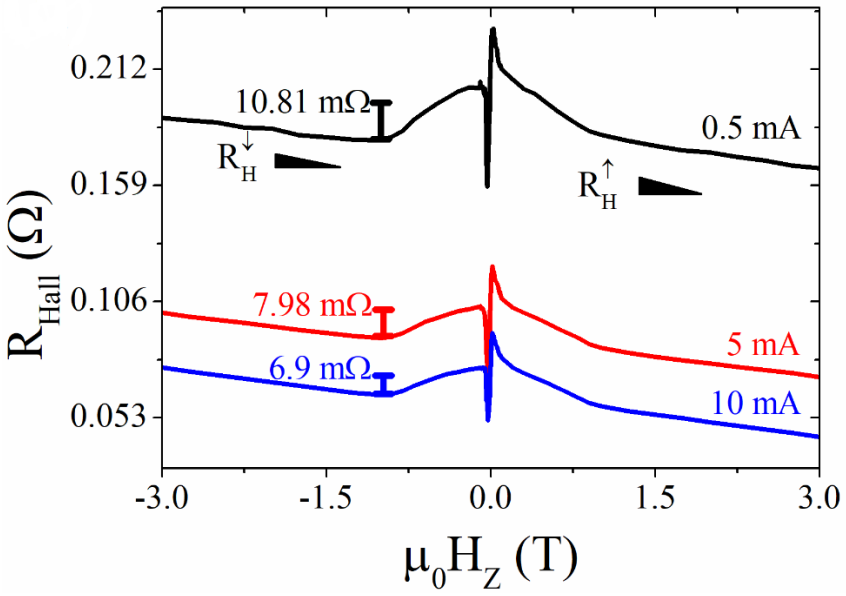

Figure 4.15. Hall effect measurement w.r.t applied out of plane magnetic field and as a function of applied current having a magnitude of 0.5 mA, 5 mA and 10 mA.

Table 4.2. The anomalous Hall resistance and Hall coefficients for up-spin and down-spin charge carrier in the composite p-Si sample as a function of current.

Applied current (mA)	$R_{AHE}(m\Omega)$	$R_H^{\uparrow}\left(\frac{n\Omega m}{T}\right)$	$R_H^{\downarrow}\left(\frac{n\Omega m}{T}\right)$
0.5	10.81	-12.508 ± 0.506	-11.008 ± 0.820
5	7.98	-13.284 ± 0.239	-12.129 ± 0.291
10	6.9	-13.841 ± 0.172	-12.998 ± 0.263

To get an additional unambiguous proof of longitudinal spin distribution, we measured the Hall effect at junctions J2 and J3 for an applied magnetic field of -3 T to 3 T

at 300 K as shown in Figure 4.16. We utilized the slope for positive and negative magnetic field to estimate the charge carrier concentration for up-spin and down-spin charge carriers as shown in Table 4.3. The estimated charge carrier density suggested that the up-spin charge carrier density increased from left to right while the opposite was true for down-spin charge carrier as shown in Table 4.3. The schematic of the expected longitudinal spin gradient is shown in Figure 4.16. It needs to be stated that the longitudinal resistance measurement did not show any difference between positive and negative magnetic field, which could be due to change in mobilities. The Hall measurement clearly showed that a longitudinal spin gradient arose along the length of the sample.

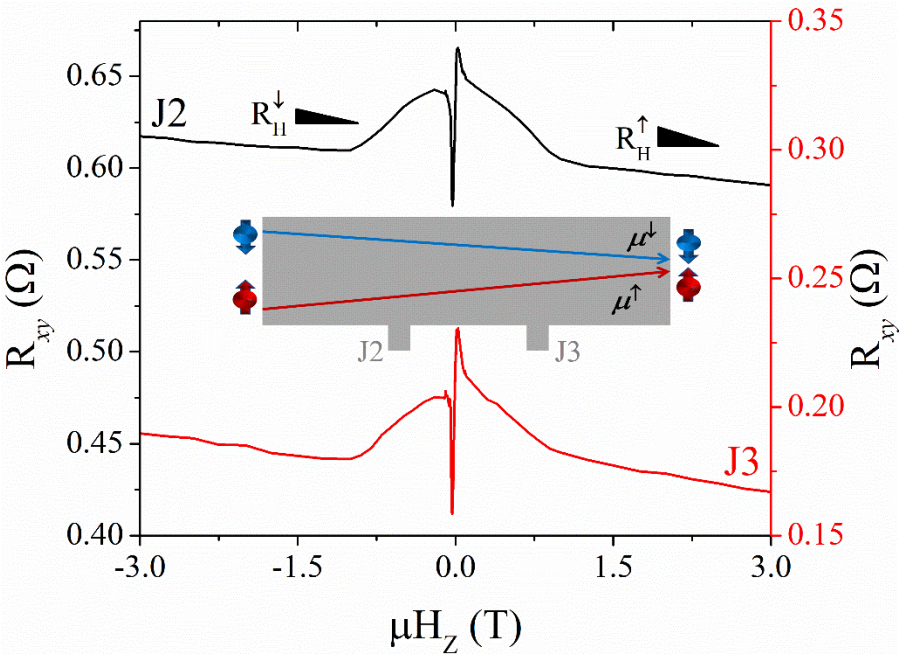

Figure 4.16. Hall effect measurement w.r.t applied out of plane magnetic field for junctions J2 and J3. Inside showing the schematic of longitudinal spin gradient.

Table 4.3. The Hall slope, resistance and carrier concentration estimated for positive and negative magnetic fields at junctions J2 and J3.

Measurement	J2		J3	
	Positive μH_z	Negative μH_z	Positive μH_z	Negative μH_z
Hall slope (Ω/T)	-7.58×10^{-3}	-5.03×10^{-3}	-6.18×10^{-3}	-5.30×10^{-3}
Hall resistance (Ωm/T)	-1.53×10^{-8}	-1.02×10^{-8}	-1.25×10^{-8}	-1.07×10^{-8}
Carrier concentration (cm^{-3})	4.07×10^{20}	6.14×10^{20}	4.99×10^{20}	5.82×10^{20}

As stated earlier, Lou et al. [124] reported anisotropic thermal transport in p-Si having layered structure similar to this study. The in-plane thermal conductivity of p-Si sample (*l*-170 µm, *w*-9 µm and *t*-2 µm) was measured at 300 K using self-heating 3ω-method as a function of out of plane magnetic field for additional insights using experimental setup described in Section 2.2 [65]. According to the equation (2.8) in Section 2.2, the in-plane thermal conductivity can be expressed in terms of the third harmonic voltage $V_{3\omega}$ in the low frequency limit by

$$\kappa \approx \frac{4I^3 R_o R' L}{\pi^4 V_{3\omega} S}$$

Where R_0, R', L, S and I are initial electrical resistance of the sample, temperature derivative of the resistance $\left(R' = \left(\frac{dR}{dT}\right)_{T_o}\right)$, sample length, cross section area and rms value of heating current, respectively. The thermal conductivity behavior as a function of magnetic field from 3T to -3T is shown in Figure 4.17. The measurement was carried out at 0.9 mA of heating current with a frequency of 8 Hz and the R' is 0.203 $^{\Omega}/_{K}$ [124]. The thermal conductivity showed a peak at saturation magnetization (M_S) as shown in Figure

4.17 similar to the results reported by Lou et al. [124]. The thermal conductivity of 2 µm Si ($\kappa = \sim 80\ Wm/k$) [144] is expected to be 4 times larger than that of $Ni_{80}Fe_{20}$ ($\kappa = \sim 20\ Wm/k$) [145] layer. We estimated that the 2 µm p-Si is 6000 times more thermally conducting than the 25 nm $Ni_{80}Fe_{20}$ layer, which means bulk of thermal transport would occur through Si layer. Hence, the thermal conductivity information would be primarily from Si layer, which is supported by the zero-field thermal conductivity value of 59.21 W/mK for the composite sample. And, the thermal conductivity for up spin was 0.4% larger than down spin as shown in Figure 4.17. This measurement showed an anisotropic thermal transport, which was a function of $Ni_{80}Fe_{20}$ layer magnetization. The anisotropic thermal transport behavior might arise due to interlayer exchange interactions and spin dependent electron phonon scattering in Si layer.

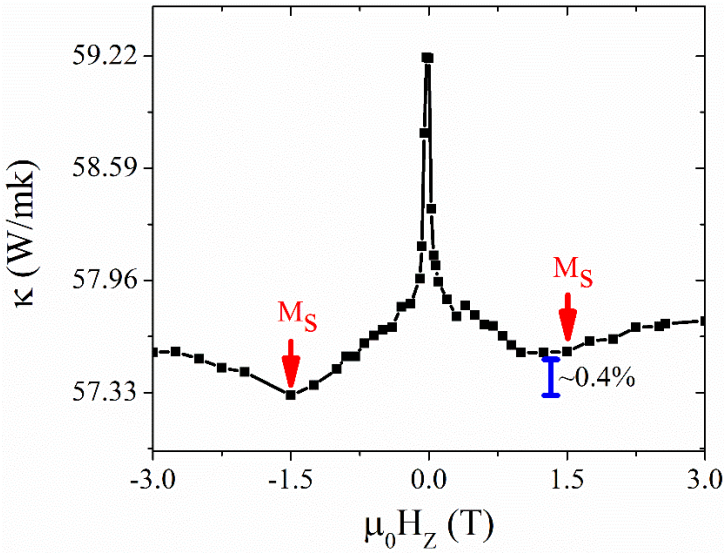

Figure 4.17. For Pd(1 nm)/$Ni_{80}Fe_{20}$ (25 nm)/MgO(1.8 nm)/SiO_2 (native)/p-Si (2 µm) composite sample the in-plane thermal conductivity measured using self-heating 3ω-method as a function of out of plane magnetic field of 3 T to -3.

The existence of spin dependent electron-phonon scattering was further verified using angle dependent magnetoresistance (ADMR) measurement shown in Figure 4.18 (a). The symmetry of the longitudinal ADMR response was similar to the expected symmetry for spin-Hall magnetoresistance (SMR) as opposed to out of plane anisotropic magnetoresistance (AMR) of the $Ni_{80}Fe_{20}$ layer as shown in Figure 4.18 (b). The magnitude of the SMR was $\sim 7 \times 10^{-4}$, which is of the same order as Pt thin films in spite of ~64% of the current shunting across the $Ni_{80}Fe_{20}$ layer in this sample. However, the spin-Hall angle could not be estimated since thickness dependent data is unavailable. Unlike heavy metals, charge transport and thermal transport in p-Si are holes and phonon mediated, respectively. The observation of both SNE and SMR indicated that thermal and charge transport behavior in p-Si layer was spin dependent. Hence, the spin, charge carrier and phonons must be coupled to affect both thermal and charge transport.

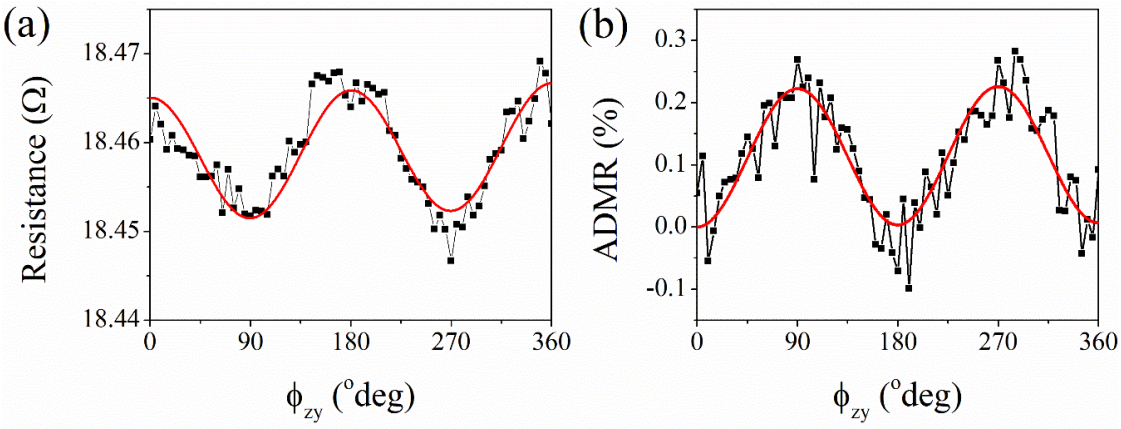

Figure 4.18. For Pd(1 nm)/$Ni_{80}Fe_{20}$ (25 nm)/MgO(1.8 nm)/SiO_2 (native)/p-Si (2 µm) composite sample (a) the angular dependence of resistance for an applied magnetic field of 4T in out of plane showing spin-Hall magnetoresistance behavior, where red line is data fit, and (b) The out of plane anisotropic magnetoresistance (AMR) in 25 nm $Ni_{80}Fe_{20}$ thin film measured by angular rotation in zy-plane which is opposite to the symmetry of SMR in (a).

To ascertain the contribution of strain gradient, a set of devices with no ferromagnetic and/or oxide layer were fabricated. Non-local resistance and the longitudinal resistance were measured in a p-Si sample on the substrate without any ferromagnetic or oxide layer. The magnitude of the non-local resistance was similar to estimates using van der Pauw's theorem. The temperature dependent non-local resistance behavior was the same as the longitudinal resistance as shown in Figure 4.19 (a). This suggests that the non-local resistance was due to leakage current and no spin current existed in the homogeneous p-Si sample. To induce strain gradient, 10 nm of MgO on top of the p-Si sample was deposited [146]. The non-local resistance then increased as the temperature decreased; the opposite behavior to that of the longitudinal resistance as shown in Figure 4.19 (b). The observed non-local resistance cannot be explained by the spin diffusion equation [146]. Instead, it, most likely, arose from the strain gradient mediated spin-phonon coupling.

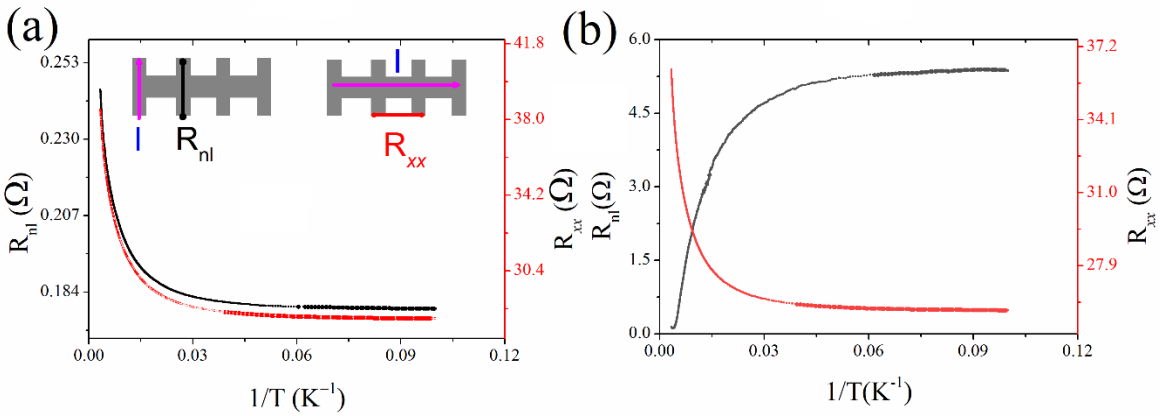

Figure 4.19. Non-local (R_{nl}) and longitudinal (R_{xx}) resistance measurement as a function of temperature (a) in p-Si (2 µm) and (b) in MgO (10 nm)/p-Si (µm) samples. Schematic of non-local and longitudinal resistance measurement setup in (a).

4.4 Discussion

In centrosymmetric Si, the relaxation rate of spin-up and spin-down charge carriers was the same. But the strain gradient led to asymmetry in the spin-phonon interactions; for example, the scattering rate of phonons with down-spin charge carriers was higher than that that of the up-spin. This behavior is supported by the Hall resistance, thermal conductivity and SMR measurements. These asymmetric spin-phonon interactions led to phonon mediated redistribution of spin chemical potential through-out the length of the sample. The phonon mediated spin redistribution drove a longitudinal as well as a transverse chiral spin current in the p-Si layer. This spin current in the p-Si layer, when coupled with the magnetization of ferromagnetic layer, gave rise to the phononic SNE as observed in the transverse magneto-thermal transport measurements presented in Figures 4.6 - 4.8 as well as SHE as shown in Figure 4.18 (a). The chiral nature of the spin current was supported by the change in the sign of the SNE along the length of the sample. The helicity of spin current was further supported by difference in hall resistances of up spin and down spin electrons at junctions J2 and J3 which resulted in career densities for up-spin electrons and down-spin electrons to increase and decrease, respectively, along the length of the sample. The transverse spin Nernst responses are found to be smaller for J1 heating than J4 heating. The resistances of the junctions J1 and J4 were 494.5 Ω and 559.7 Ω respectively, which would lead to difference in input heating power and responses. In addition, the strain distribution was different because of heating and could cause the resulting difference in observed responses. A careful observation of thermopower coefficients, presented in Table 4.1, showed that the Hall junction closer to the heat source

(30 μm) had the highest temperature gradient but the smallest coefficient. Whereas the junction farthest (100 μm) from the heat source behaved completely opposite. This suggested that the long wavelength phonons coupled to spin the most and the short wavelength phonons the least. In a recent work, Rückriegel and Duine [147] showed that magnetoelastic coupling can lead to long range phonon spin transport. The centrosymmetric Si lattice will not have magnetoelastic coupling, but strain gradient, in conjunction with interlayer coupling, can induce it in Si layer. While the structure used in their theoretical study differed, their hypothesis was clearly supported by the thermal transport behavior in our study. We showed that the phononic SNE was driven primarily by the coupling of spin to long wavelength acoustic phonons.

4.5 Conclusion

An observation of transverse phononic spin-Nernst effect in Si is shown. This behavior is expected to arise due to asymmetric spin-phonon interactions and interlayer coupling between p-Si and $Ni_{80}Fe_{20}$ layers. The interlayer exchange coupling behavior is supported by observation of spin-Hall magnetoresistance and magnetoresistance as a function of crystallographic orientation of Si layer. The interlayer exchange interactions can arise due to flexoelectric polarization from strain gradient especially at the interface from the residual stresses and buckling of freestanding specimen. This study also demonstrates that the spin-Nernst magneto thermopower coefficient can be as large as 45.4 μV/K for long wavelength acoustic phonons, which is larger than the Seebeck coefficient of most spintronics materials. The anomalous Hall resistance reduces as the current is increased which showed that the strain gradient due to thermal stress is causing the

scattering mechanism to change its sign. This study challenges the rules of spintronics that revolve around spin-orbit coupling. The spin-phonon coupling can provide a better alternative to spin current generation, detection and manipulation because it can be controlled by strain gradient.

Chapter 5 Spin Phonon Coupling in Silicon

Discovery of hidden spin polarization in centrosymmetric materials [148-150] have given a new direction to spintronics materials research. Hidden Rashba and Dresselhaus spin splitting arise due to site (local) asymmetries instead of global asymmetry. The predicted hidden spin polarization has been experimentally reported for a number of centrosymmetric materials using spectroscopy techniques. However, consequences of hidden spin polarization on transport behavior is not well understood, which is essential for the device applications. Among all the centrosymmetric materials, Zhang et al. [148] also predicted hidden Dresselhaus spin splitting in Si. Si is the premier material in semiconductor electronics and experimental discovery of hidden spin polarization in Si can make the Si spintronics a reality. However, no direct experimental evidence of hidden spin polarization Si has been reported. Recently, Lou et al. has reported large spin-Hall effect (SHE) [151] and spin-Seebeck effect in Si, which they attributed to the strain gradient mediated spin-phonon coupling. Similarly, Wang et al. [152] reported large flexoelectric effect from charge separation due to strain gradient. We hypothesized that SHE and spin-phonon coupling might arise due to hidden spin polarization, which could be uncovered using strain gradient. This motivated us to experimentally study the hidden spin polarization in Si using strain gradient mediated symmetry breaking. In this study, we present the first experimental evidence of hidden spin polarization and magnetic moment along the <111> directions in diamond cubic Si lattice. The magnetic moment was experimentally observed using Anomalous Hall effect (AHE) measurement. Due to weak

spin-orbit coupling (SOC), the spin is found to be coupled to longitudinal acoustic phonons, which give rise to spin phonon coupling and spin-Hall effect.

To uncover the hidden spin polarization in Si, we fabricated an experimental setup having a freestanding p-Si hall bar sample (similar to as shown in Figure 4.2 (f) and 4.4 in chapter 4). The residual stresses in the p-Si layer are expected to be small. To induce large strain gradient, we deposited 1.8 nm of MgO and 25 nm Pt on top of p-Si layer. The melting point of Pt is very high as compared to Si and thin film deposition using e-beam evaporation will lead to large residual thermal mismatch stresses. These stresses would cause the buckling of the composite (25 nm Pt/ 1.8 nm MgO/ 2 μm p-Si) sample and, as a consequence, strain gradient and flexoelectric polarization would arise in p-Si.

To uncover the hidden spin polarization, we analyzed the angle dependent magnetoresistance (ADMR) behavior. The ADMR was measured by applying the current between junctions J1 and J4 and measuring the 2ω resistance between J2 and J3, while rotating the sample in yz plane in the presence of applied magnetic field. The (longitudinal) $R_{2\omega}$ angular modulations at 300 K corresponding to 4 T and 8 T are shown in Figure 5.1 (a). We observed that the ADMR showed lower resistances corresponding to ~55° and 125° from the vertical direction. Similarly, higher resistances were observed corresponding to 235° and 305°. In the single crystal Si wafer vertical direction point towards [001] direction. Consequently, the $[1\bar{1}1]$ and $[1\bar{1}\bar{1}]$ directions will have an angle of ~54.7° with [001] direction. When the magnetic field was aligned parallel along the $[1\bar{1}1]$ and $[1\bar{1}\bar{1}]$ directions, we observe low resistance state and the anti-parallel configuration gave rise to higher resistance state. This ADMR behavior could be considered anisotropic

magnetoresistance (AMR), which necessitated magneto crystalline anisotropy and magnetic moment in p-Si aligned along $[1\bar{1}1]$ and $[1\bar{1}\bar{1}]$ directions. The magneto crystalline anisotropy arises due to SOC, which is negligible in Si. In addition, the SOC based magneto crystalline anisotropy should give rise to easy axis along [100] direction and hard axis along the [111] direction in the cubic lattice as opposed to observed symmetry. The <111> directions in Si also represent the direction of tetrahedral bonding. Hence, the magnetic moment in Si layer was aligned along the Si-Si covalent bond. A careful analysis of the crystallography in Si tetrahedron suggested magnetic moment pointed outwards from the center of tetrahedron in $[1\bar{1}\bar{1}]$ direction and pointed inwards along the $[1\bar{1}1]$ direction as shown in Figure 5.1 (b). This behavior clearly showed broken inversion symmetry and resulting hidden spin polarization. Zhang et al. [148], in their work on hidden polarization, showed spin contribution from one sector of the tetrahedron being opposite of other sector, which led to no net spin polarization in Si. The transverse resistance measurements, presented in Chapter 4, did not show any switching behavior, which meant that there is no net magnetization in the sample and Si layer. Hence, the spin polarization along $[11\bar{1}]$ should point inwards and along $[111]$ should be outwards as shown in Figure 5.1 (b). This behavior replicated the theoretical calculations reported by Zhang et al [148].

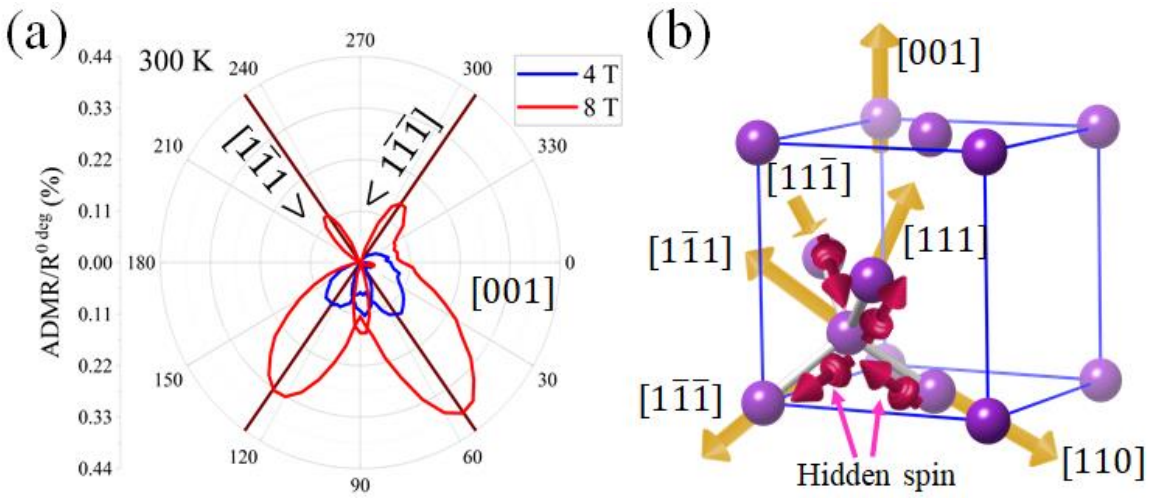

Figure 5.1. (a) Angle dependent magnetoresistance modulation in yz plane at 300K in Pt/p-Si sample, (b) diamond cubic crystal structure of Si showing the hidden spin polarization.

The angle dependent longitudinal resistance across multiple p-Si and n-Si devices with $Ni_{80}Fe_{20}$ top layer were also measured. In some Py/p-Si devices, we observed an angle dependent response that was summation of AMR behavior of Py and cosine behavior attributed to the giant magnetoresistance (GMR) as shown in Figure 5.2 (a). The observed GMR behavior (current in plane-CIP configuration) was intriguing since it meant that there was a net magnetic moment in the Si layer. Not only that, the net magnetic moment was oriented out of plane, which was consistent with the ADMR response observed in Pt/p-Si composite sample. We also measured the angle dependent (zy-plane) longitudinal $R_{2\omega}$ response in the Hall device having GMR response to uncover any non-reciprocal/unidirectional response [153] or spin-phonon coupling mediated behavior as shown in Figure 5.2 (b). The symmetry behavior in angle dependent $R_{2\omega}$ response was similar to the ADMR response in Pt/p-Si composite sample presented in Figure 5.1 (a). The $R_{2\omega}$ response was lowest for magnetic field pointed along $[1\bar{1}\bar{1}]$ and larger when the

magnetic field was pointed along [1$\bar{1}$1] and [$\bar{1}$11]. Hence, when the magnetic moment of $Ni_{80}Fe_{20}$ was pointed in the -z–direction, then the resistance was lowest. Whereas it was highest when the magnetic field was pointed along +z–direction as shown in Figure 5.2 (b). This behavior explains the GMR response as well since it also shows a parallel configuration for -z–direction and antiparallel configuration for +z–direction as shown in Figure 5.2 (a). Hence, the angle dependent $R_{2\omega}$ response was attributed to the unidirectional GMR behavior.

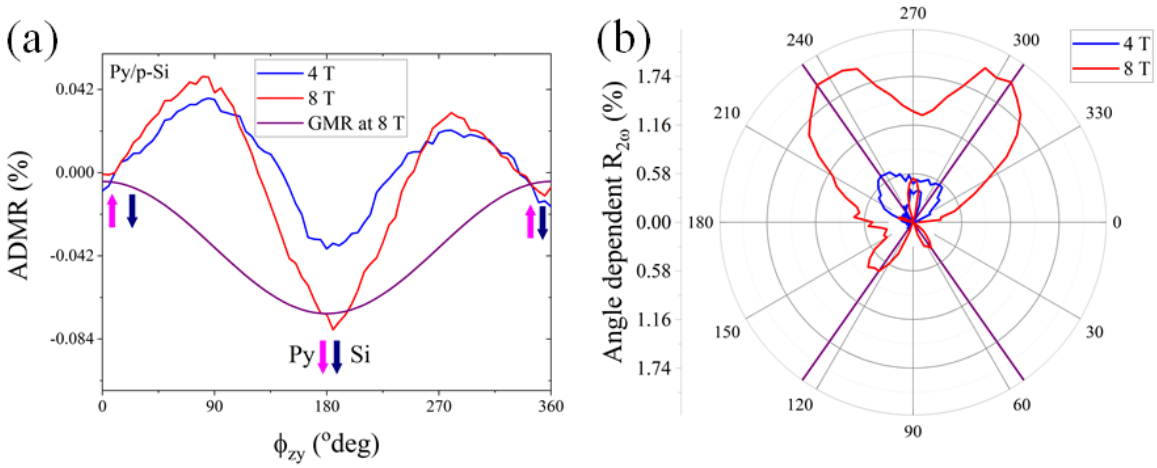

Figure 5.2. Angle dependent longitudinal resistance in Py/p-Si sample showing the AMR and GMR behavior, (b) Crystallographic ADMR modulation of the Py/p-Si sample.

Since the magnetic moment in Si layer was aligned along <111> family of directions, the transport behavior should change if the longitudinal orientation of the Si layer was changed. All the samples (both n-Si and p-Si) were aligned along the [110] direction. We fabricated a set of Py/p-Si samples with the orientation of the Si layer along [110] and [100] as shown in Figure 5.3. The magnetoresistance (MR) measurement for current applied along <110> and <100> directions are shown in Figure 5.4 (a). The negative MR measured in the composite sample could only arise due to Py layer. However,

the qualitative difference between the shape of the MR plot confirmed existence of interlayer spin dependent coupling between Py and p-Si since MR was a function of crystallographic orientation ([110] & [100]) of Si layer.

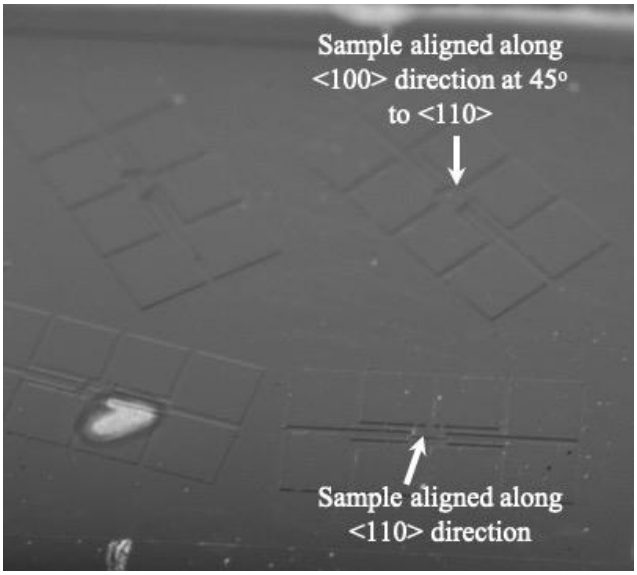

Figure 5.3. Optical image showing two device structure corresponding to sample orientation along <110> and <100> direction in p-Si layer for Py/p-Si.

The next step was to ascertain the role of p-Si layer. Crystallography dependent longitudinal $V_{2\omega}$ response was recorded as a function of applied out of plane magnetic field. The $V_{2\omega}$ response were experimentally studied in samples oriented along <110> and <100> direction of Si lattice as shown in Figure 5.4 (b). The measured $V_{2\omega}$ responses clearly demonstrated anisotropic magneto thermopower behavior in both samples. However, their magnetic field dependence was opposite to each other even though both samples exhibited magnetic saturation expected from Py thin film. This measurement clearly supported interlayer spin-phonon interactions in the p-Si and Py layers. In case of longitudinal axis along [110], the two independent <111> directions are in the cross-sectional plane of the sample as shown in Figure 5.4 (c), which might give rise to the

magnetic moment in the vertical direction. Whereas in case of <100> longitudinal axis, all the four independent <111> directions are oriented at an angle out of plane from cross-sectional plane [Figure 5.4 (d)], which might give rise to no net magnetic moment. This difference would change the resulting MR response as observed experimentally.

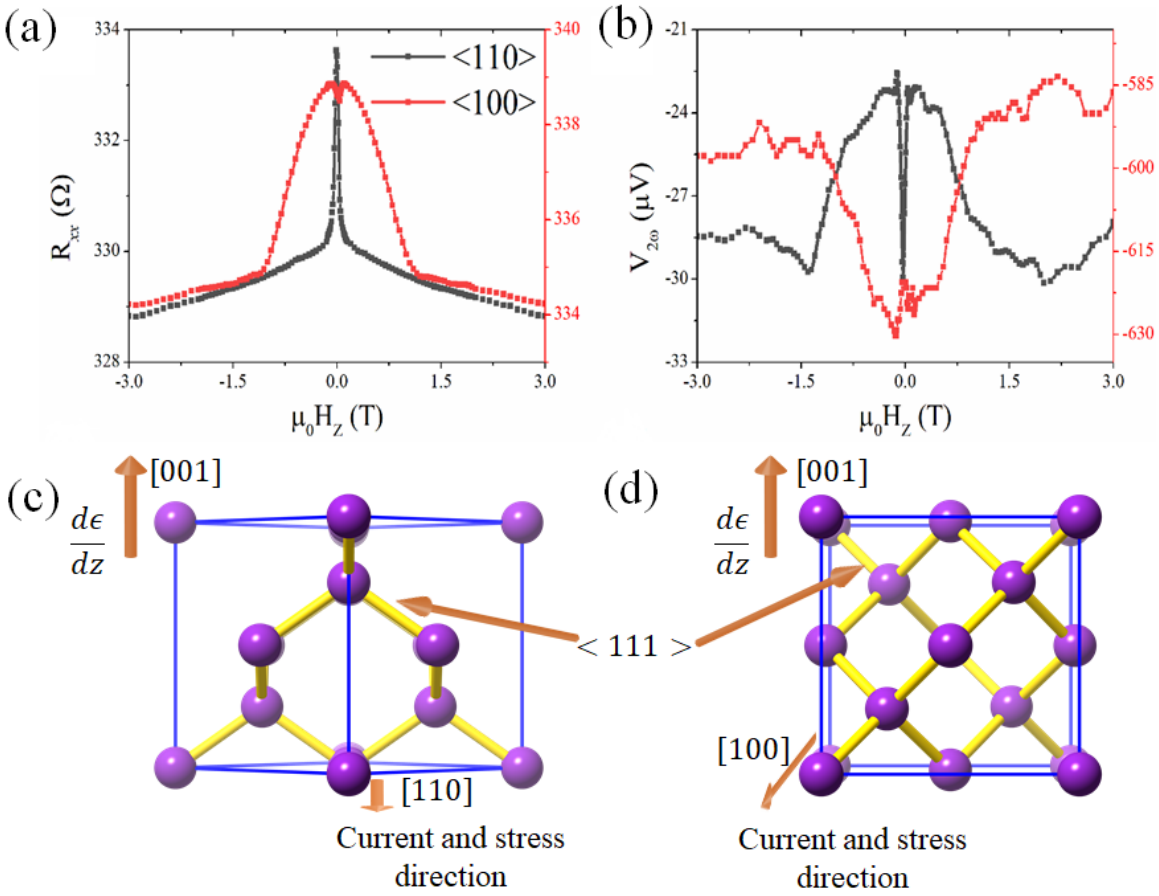

Figure 5.4. For Py/p-Si sample: crystallographic direction dependent (a) magnetoresistance and (b) longitudinal $V_{2\omega}$ response as a function of out of plane magnetic field for a current applied along <110> direction and <100> direction of the p-Si layer. (c) & (d) <111> cross sectional planes for [110] & [100] directions, respectively. $d\epsilon/dz$ is the strain gradient.

Chapter 6 Summary & Future Work

6.1 Summary

We have studied magneto-thermal transport behavior in nanoscale metallic (Au) and semiconductor (Si) films using the self-heating 3-omega thermal transport characterization technique.

Spin polarization, when induced in a non-ferromagnetic material, can change the underlying material behavior especially if the spin diffusion length is of the same order as the sample dimension such as thickness. We experimentally demonstrated thermal hysteretic behavior induced by spin polarization in $Ni_{80}Fe_{20}$ (10 nm)/Au (100 nm) bilayer freestanding sample. The thermal hysteresis behavior was uncovered using magneto thermal characterization based on self-heating 3ω method. The third harmonic voltage showed diverging behavior and thermal hysteresis during cooling and heating of the sample under an applied magnetic field, which was attributed to the spin accumulation. The spin accumulation and thermal hysteresis in Au occurred due to ferromagnetic proximity polarization from $Ni_{80}Fe_{20}$ layer. The observed hysteresis behavior was also attributed to freestanding thin film structure and absence of substrate effects leading to longer spin diffusion length. This study demonstrated experimental evidence of ferromagnetic proximity polarization and resulting changes in thermal transport behavior in Au thin films.

Silicon's weak intrinsic spin-orbit coupling, and centrosymmetric crystal structure are a critical bottleneck to the development of Si spintronics, because they lead to an insignificant spin-Hall effect (spin current generation) and inverse spin-Hall effect (spin

current detection). We undertook crystallography dependent magnetoresistance and magneto-thermal transport measurements to study crystallography dependent spin polarization in freestanding Si thin films. We observed 4% strain at Si interface from HRTEM studies. We observed that the magnetoresistance behavior of the sample was dependent on direction of the applied current. We performed DFT studies on Si with 4% strain applied at different crystallography direction and we saw distinct change in the band structure of the Si. One explanation of this behavior could be the spin dependent coupling between $Ni_{80}Fe_{20}$ and p-Si layers. The macroscopic origin of the spin-phonon coupling could be large strain gradients that can exist in the freestanding Si films. This discovery in a light, earth abundant and centrosymmetric material opens a new path of strain engineering to achieve spin dependent properties in technologically highly developed materials.

Due to its weak intrinsic spin orbit coupling, Si is widely regarded as an inefficient material for spin generation and detection. But efforts are going on to change this destiny. We present an experimental proof of spin-phonon coupling and thermal spin current generation using phononic thermal transport in Si thin films in spite of having insignificant intrinsic spin-orbit coupling. The strain gradient acted as an external switch that broke the symmetry of spin relaxation behavior and modify the spin-phonon interactions. The spin-phonon interactions led to a phonon-driven redistribution of spin potential and spin current. The phonon-driven spin current gave rise to a phononic spin-Nernst effect due to interlayer coupling of Si with $Ni_{80}Fe_{20}$ thin film. The coefficient of spin-Nernst magneto-thermopower was estimated to be an order of magnitude larger than heavy metals (W). The

primary heat carrier in Si are phonons and resulting spin-Nernst effect was expected to arise due to spin dependent electron-phonon scattering, which was also supported by spin-Hall magnetoresistance and Hall resistance measurement. Observation of phononic spin-Nernst effect puts spotlight back on Si for spintronics and spin caloritronics applications.

6.2 Future Work

We have demonstrated thermal hysteretic behavior in $Ni_{80}Fe_{20}$/Au. This behavior occurred due to spin accumulation in Au triggered by ferromagnetic proximity polarization. However, concrete understanding of origin of this spin accumulation needs to be done. The results in our experiments show a potential use of our system in applications such as magnetic cooling and refrigeration applications. To realize this, large reduction in thermal gradient or increase in net cooling effect is required. One way could be to have this system arranged in series (multi-layer structures of $Ni_{80}Fe_{20}$/Au) which may result in an amplified cooling effect. The thickness of the individual layers in the system studied here was 10 nm $Ni_{80}Fe_{20}$ and 100 nm Au. It will be interesting to see the relationship between the thicknesses of $Ni_{80}Fe_{20}$ and Au, and to what extent the observed interactions are dependent on their thicknesses. We would like to try this experiment with different normal metal such as W, Pt or Ta etc. We also should implement cheaper, earth abundant material into our system and explore the possibility of introducing materials that could replace current products in the market which are either expensive or require complex material synthesis.

Silicon can be a promising material for spintronics due to its long spin diffusion length at room temperature. But insignificant intrinsic spin-orbit coupling leads to very small

inverse spin-Hall effect, which is a bottleneck for the realization of Si spintronics. Effective manipulation of spin current in Si system is, therefore, of utmost importance. Spin-dependent interactions between $Ni_{80}Fe_{20}$ and p-Si induced spin polarization happened only when current is passed in the preferred <110> direction. Future study needs to happen to get an in-depth understanding of the behavior. First, the thickness of the Si layer was 2 μm. Si thickness dependent study needs to be performed to have a holistic picture of the observed effects. Second, $Ni_{80}Fe_{20}$ layer thickness should also be varied as it can provide insights on strain gradient dependent studies. A tiny probe may also be used to induce controlled strain gradient. Third, we qualitatively studied the current direction dependency on spin polarization in Si. The immediate work that follows is to observe this behavior at different length of the Si beam and quantify the polarization. The MR measurement was observed for an out of plane field rotation. In order to quantify the MR or spin-hall magneto resistance (SMR) behavior in the crystallography sample, we need to conduct experiments for field rotation on all three principal planes. Magneto thermal transport studies needs to be conducted as well on this system for quantifying thermal properties such as thermal conductivity (κ), specific heat (C_p) etc.

The observation of spin-phonon coupling and resulting spin Nernst response is crucial in advancing Si based spintronics research. We observed SNE in the p-Si sample. Next follows n-Si and even bare Si. We need to repeat all experiments, that we did for p-Si, for n-Si and bare Si and see the nature of effects that would arise. Also thickness dependent studies of Si and Py should also be undertaken to study the dependence of response on the overall thickness of the system.

References

1. Bandyopadhyay, S. and M. Cahay, *Introduction to spintronics*. Second edition. ed. 2016, Boca Raton: CRC Press. xxi, 636 pages.

2. Baibich, M.N., et al., *Giant magnetoresistance of (001)Fe/(001)Cr magnetic superlattices.* Phys Rev Lett, 1988. **61**(21): p. 2472-2475.

3. Binasch, G., et al., *Enhanced magnetoresistance in layered magnetic structures with antiferromagnetic interlayer exchange.* Phys Rev B Condens Matter, 1989. **39**(7): p. 4828-4830.

4. Joshi, V.K., *Spintronics: A contemporary review of emerging electronics devices.* Engineering Science and Technology-an International Journal-Jestech, 2016. **19**(3): p. 1503-1513.

5. Niemier, M.T., et al., *Nanomagnet logic: progress toward system-level integration.* J Phys Condens Matter, 2011. **23**(49): p. 493202.

6. Wunderlich, J., et al., *Spin Hall effect transistor.* Science, 2010. **330**(6012): p. 1801-4.

7. Boona, S.R., R.C. Myers, and J.P. Heremans, *Spin caloritronics.* Energy & Environmental Science, 2014. **7**(3): p. 885-910.

8. Bauer, G.E.W., A.H. MacDonald, and S. Maekawa, *"Spin Caloritronics".* Solid State Communications, 2010. **150**(11-12): p. 459-460.

9. Bauer, G.E.W., E. Saitoh, and B.J. van Wees, *Spin caloritronics.* Nature Materials, 2012. **11**(5): p. 391-399.

10. Bauer, G.E.W., *Spin Caloritronics.* Spin Current, 2nd Edition, 2017. **22**: p. 143-159.

11. Prando, G., *Spin Caloritronics Spin Nernst Effect.* Nature Nanotechnology, 2017. **12**(12): p. 1115-1115.

12. Yu, H.M., S.D. Brechet, and J.P. Ansermet, *Spin caloritronics, origin and outlook.* Physics Letters A, 2017. **381**(9): p. 825-837.

13. Idzuchi, H., Y. Fukuma, and Y. Otani, *Spin transport in non-magnetic nano-structures induced by non-local spin injection.* Physica E-Low-Dimensional Systems & Nanostructures, 2015. **68**: p. 239-263.

14. Bychkov, Y.A. and E.I. Rashba, *Properties of a 2d Electron-Gas with Lifted Spectral Degeneracy.* Jetp Letters, 1984. **39**(2): p. 78-81.

15. Bihlmayer, G., O. Rader, and R. Winkler, *Focus on the Rashba effect.* New Journal of Physics, 2015. **17**.

16. Rojas Sanchez, J.C., et al., *Spin-to-charge conversion using Rashba coupling at the interface between non-magnetic materials.* Nature Communications, 2013. **4**(2944).

17. Uchida, K., et al., *Observation of the spin Seebeck effect.* Nature, 2008. **455**(7214): p. 778-781.

18. Okamoto, S., *Spin injection and spin transport in paramagnetic insulators.* Physical Review B, 2016. **93**(6).

19. Rudner, M.S. and J.C. Song, *Self-induced Berry flux and spontaneous non-equilibrium magnetism.* Nature Physics, 2019. **15**(10): p. 1017-1021.

20. Foa Torres, L., *A sudden twist.* 2019.

21. Valenzuela, S.O., *Nonlocal Electronic Spin Detection, Spin Accumulation and the Spin Hall.* International Journal of Modern Physics B, 2009. **23**(11): p. 2413-2438.

22. Niimi, Y. and Y. Otani, *Reciprocal spin Hall effects in conductors with strong spin-orbit coupling: a review.* Reports on Progress in Physics, 2015. **78**(12).

23. Dyakonov, M.I. and V.I. Perel, *Possibility of Orienting Electron Spins with Current.* Jetp Letters-Ussr, 1971. **13**(11): p. 467-&.

24. Hirsch, J.E., *Spin Hall effect.* Physical Review Letters, 1999. **83**(9): p. 1834-1837.

25. Sinova, J., et al., *Spin Hall effects.* Reviews of Modern Physics, 2015. **87**(4): p. 1213-1259.

26. Chen, Y.T., et al., *Theory of spin Hall magnetoresistance (SMR) and related phenomena.* Journal of Physics-Condensed Matter, 2016. **28**(10).

27. Nakayama, H., et al., *Spin Hall magnetoresistance induced by a nonequilibrium proximity effect.* Physical review letters, 2013. **110**(20): p. 206601.

28. Xiao, J., et al., *Theory of magnon-driven spin Seebeck effect.* Physical Review B, 2010. **81**(21).

29. Adachi, H., et al., *Theory of the spin Seebeck effect.* Reports on Progress in Physics, 2013. **76**(3).

30. Jaworski, C.M., et al., *Giant spin Seebeck effect in a non-magnetic material.* Nature, 2012. **487**(7406): p. 210-213.

31. Jaworski, C.M., et al., *Observation of the spin-Seebeck effect in a ferromagnetic semiconductor.* Nature Materials, 2010. **9**(11): p. 898-903.

32. Uchida, K., et al., *Observation of longitudinal spin-Seebeck effect in magnetic insulators.* Applied Physics Letters, 2010. **97**(17).

33. Uchida, K., et al., *Longitudinal spin Seebeck effect in various garnet ferrites.* Physical Review B, 2013. **87**(10).

34. Avery, A.D., M.R. Pufall, and B.L. Zink, *Observation of the Planar Nernst Effect in Permalloy and Nickel Thin Films with In-Plane Thermal Gradients.* Physical Review Letters, 2012. **109**(19).

35. Wesenberg, D., et al., *Relation of planar Hall and planar Nernst effects in thin film permalloy.* Journal of Physics D-Applied Physics, 2018. **51**(24).

36. Pu, Y., et al., *Anisotropic thermopower and planar nernst effect in Ga1-xMnxAs ferromagnetic semiconductors.* Physical Review Letters, 2006. **97**(3).

37. Meier, D., et al., *Influence of heat flow directions on Nernst effects in Py/Pt bilayers.* Physical Review B, 2013. **88**(18).

38. Yin, S.L., et al., *Hybrid anomalous and planar Nernst effect in permalloy thin films.* Physical Review B, 2013. **88**(6).

39. Reimer, O., et al., *Quantitative separation of the anisotropic magnetothermopower and planar Nernst effect by the rotation of an in-plane thermal gradient.* Scientific Reports, 2017. **7**.

40. Bui, C.T., et al., *Planar Nernst effect and Mott relation in (In, Fe)Sb ferromagnetic semiconductor.* Journal of Applied Physics, 2018. **123**(17).

41. Nagaosa, N., et al., *Anomalous Hall effect.* Reviews of Modern Physics, 2010. **82**(2): p. 1539-1592.

42. Sultan, R., et al., *Thermal conductivity of micromachined low-stress silicon-nitride beams from 77 to 325 K.* Journal of Applied Physics, 2009. **105**(4).

43. Sheng, P., et al., *The spin Nernst effect in tungsten.* Science Advances, 2017. **3**(11).

44. Kim, D.J., et al., *Observation of transverse spin Nernst magnetoresistance induced by thermal spin current in ferromagnet/non-magnet bilayers.* Nature Communications, 2017. **8**.

45. Bose, A., et al., *Direct detection of spin Nernst effect in platinum.* Applied Physics Letters, 2018. **112**(16).

46. Meyer, S., et al., *Observation of the spin Nernst effect.* Nature Materials, 2017. **16**(10): p. 977-+.

47. Sumiyama, A., et al., *Meissner effect in Au induced by the proximity effect in the clean limit.* Czechoslovak Journal of Physics, 1996. **46**: p. 739-740.

48. Narikiyo, O. and H. Fukuyama, *Proximity Induced Meissner Effect in Dirty Normal Metals.* Journal of the Physical Society of Japan, 1989. **58**(12): p. 4557-4568.

49. Yokoyama, T., Y. Tanaka, and N. Nagaosa, *Anomalous Meissner Effect in a Normal-Metal-Superconductor Junction with a Spin-Active Interface.* Physical Review Letters, 2011. **106**(24).

50. Flokstra, M.G., et al., *Remotely induced magnetism in a normal metal using a superconducting spin-valve.* Nature Physics, 2016. **12**(1): p. 57-U87.

51. Lou, P.C. and S. Kumar, *Spin-Driven Emergent Antiferromagnetism and Metal–Insulator Transition in Nanoscale p-Si.* physica status solidi (b), 2017: p. 1700545.

52. Lou, P.C., W.P. Beyermann, and S. Kumar, *Spin mediated magneto-electro-thermal transport behavior in Ni80Fe20/MgO/p-Si thin films.* Journal of Applied Physics, 2017. **122**(12): p. 123905.

53. Lou, P.C. and S. Kumar, *Spin-Hall effect and emergent antiferromagnetic phase transition in n-Si.* Journal of Magnetism and Magnetic Materials, 2018. **452**: p. 129-133.

54. Goodman, P., *Current and future uses of gold in electronics.* Gold Bulletin, 2002. **35**(1): p. 21-26.

55. Yamamoto, Y., et al., *Direct observation of ferromagnetic spin polarization in gold nanoparticles.* Physical Review Letters, 2004. **93**(11).

56. Wu, C.M., et al., *Quantum spins in Mackay icosahedral gold nanoparticles.* Journal of Nanoparticle Research, 2010. **12**(1): p. 177-185.

57. Nealon, G.L., et al., *Magnetism in gold nanoparticles.* Nanoscale, 2012. **4**(17): p. 5244-5258.

58. Qu, D., et al., *Self-consistent determination of spin Hall angles in selected 5d metals by thermal spin injection.* Physical Review B, 2014. **89**(14): p. 140407.

59. Isasa, M., et al., *Temperature dependence of spin diffusion length and spin Hall angle in Au and Pt.* Physical Review B, 2015. **91**(2): p. 024402.

60. Johnson, M., *Spin accumulation in gold films.* Physical Review Letters, 1993. **70**(14): p. 2142-2145.

61. Wenner, F. and United States., *A method of measuring earth resistivity*. 1915, Washington,: Govt. print. off. p. 469-478 incl. diagrs 26 cm.

62. Smits, F.M., *Measurement of Sheet Resistivities with the 4-Point Probe.* Bell System Technical Journal, 1958. **37**(3): p. 711-718.

63. Ryan, M.A. *Image Reversal with AZ5214E Photoresist for Etch and Liftoff*. in *Journal of the Microelectronic Engineering Conference*. 1987.

64. Dames, C., *Measuring the thermal conductivity of thin films: 3 omega and related electrothermal methods.* Annual Review of Heat Transfer, 2013. **16**.

65. Lu, L., W. Yi, and D.L. Zhang, *3 omega method for specific heat and thermal conductivity measurements.* Review of Scientific Instruments, 2001. **72**(7): p. 2996-3003.

66. Idzuchi, H., Y. Fukuma, and Y. Otani, *Spin transport in non-magnetic nano-structures induced by non-local spin injection.* Physica E: Low-dimensional Systems and Nanostructures, 2015. **68**: p. 239-263.

67. Ku, J., et al., *Spin injection in NiFe/Au/NiFe spin valves.* Journal of Magnetism and Magnetic Materials, 2006. **304**(1): p. E273-E275.

68. Franz, R. and G. Wiedemann, *Ueber die Wärme-Leitungsfähigkeit der Metalle.* Annalen der Physik, 1853. **165**(8): p. 497-531.

69. Cahill, D.G., *Thermal conductivity measurement from 30 to 750 K: the 3 omega method.* Review of Scientific Instruments, 1990. **61**(2): p. 802-808.

70. Liu, J., et al., *Giant magnetocaloric effect driven by structural transitions.* Nature Materials, 2012. **11**: p. 620.

71. Nascimento, F.I.F., et al., *Thermal hysteresis of ferromagnetic/antiferromagnetic compensated bilayers.* Physical Review B, 2009. **80**(14): p. 144407.

72. Gutfleisch, O., et al., *Mastering hysteresis in magnetocaloric materials.* Philosophical Transactions of the Royal Society A: Mathematical, Physical and Engineering Sciences, 2016. **374**(2074).

73. Dan'kov, S.Y., et al., *Magnetic phase transitions and the magnetothermal properties of gadolinium.* Physical Review B, 1998. **57**(6): p. 3478-3490.

74. Tishin, A.M., K.A. Gschneidner, and V.K. Pecharsky, *Magnetocaloric effect and heat capacity in the phase-transition region.* Physical Review B, 1999. **59**(1): p. 503-511.

75. Shen, B.G., et al., *Recent Progress in Exploring Magnetocaloric Materials.* Advanced Materials, 2009. **21**(45): p. 4545-4564.

76. Brooker, S., *Spin crossover with thermal hysteresis: practicalities and lessons learnt.* Chemical Society Reviews, 2015. **44**(10): p. 2880-2892.

77. Reich, S., G. Leitus, and Y. Feldman, *Observation of magnetism in Au thin films.* Applied Physics Letters, 2006. **88**(22): p. 222502.

78. Hori, H., et al., *Diameter dependence of ferromagnetic spin moment in Au nanocrystals.* Physical Review B, 2004. **69**(17): p. 174411.

79. Prusty, S., et al., *Unusual ferromagnetic behaviour of embedded non-functionalized Au nanoparticles in Bi/Au bilayer films.* RSC Advances, 2016. **6**(108): p. 106584-106590.

80. Singh, R., *Unexpected magnetism in nanomaterials.* Journal of Magnetism and Magnetic Materials, 2013. **346**: p. 58-73.

81. Tuboltsev, V., et al., *Magnetism in Nanocrystalline Gold.* ACS Nano, 2013. **7**(8): p. 6691-6699.

82. Laczkowski, P., et al., *Enhancement of the spin signal in permalloy/gold multiterminal nanodevices by lateral confinement.* Physical Review B, 2012. **85**(22): p. 220404.

83. Stejskal, O., et al., *Optimization of spin injection and spin detection in lateral nanostructures by geometrical means.* Journal of Magnetism and Magnetic Materials, 2016. **414**: p. 132-143.

84. Emmanouil, M., et al., *Modulation of spin accumulation by nanoscale confinement using electromigration in a metallic lateral spin valve.* Nanotechnology, 2016. **27**(9): p. 095201.

85. Johnson, M., *Spin polarization of gold films via transported (invited).* Journal of Applied Physics, 1994. **75**(10): p. 6714-6719.

86. Zhang, W., et al., *Spin pumping and inverse Rashba-Edelstein effect in NiFe/Ag/Bi and NiFe/Ag/Sb.* Journal of Applied Physics, 2015. **117**(17).

87. Lv, Y., et al., *Unidirectional spin-Hall and Rashba−Edelstein magnetoresistance in topological insulator-ferromagnet layer heterostructures.* Nature Communications, 2018. **9**(1): p. 111.

88. Vdovichev, S.N., et al., *High magnetocaloric efficiency of a NiFe/NiCu/CoFe/MnIr multilayer in a small magnetic field.* Physical Review B, 2018. **98**(1): p. 014428.

89. Jansen, R., *Silicon spintronics.* Nature Materials, 2012. **11**(5): p. 400-408.

90. Ando, K. and E. Saitoh, *Observation of the inverse spin Hall effect in silicon.* Nature Communications, 2012. **3**.

91. Jansen, R., et al., *Silicon spintronics with ferromagnetic tunnel devices.* Semiconductor Science and Technology, 2012. **27**(8).

92. Sinova, J., et al., *Spin Hall effects.* Reviews of Modern Physics, 2015. **87**(4): p. 1213-1260.

93. Kato, Y.K., et al., *Observation of the Spin Hall Effect in Semiconductors.* Science, 2004. **306**(5703): p. 1910-1913.

94. Bernevig, B.A. and S.-C. Zhang, *Spin splitting and spin current in strained bulk semiconductors.* Physical Review B, 2005. **72**(11): p. 115204.

95. Crooker, S.A., et al., *Imaging Spin Transport in Lateral Ferromagnet/Semiconductor Structures.* Science, 2005. **309**(5744): p. 2191.

96. Xiao, D., M.-C. Chang, and Q. Niu, *Berry phase effects on electronic properties.* Reviews of Modern Physics, 2010. **82**(3): p. 1959-2007.

97. Xiao, D., et al., *Polarization and Adiabatic Pumping in Inhomogeneous Crystals.* Physical Review Letters, 2009. **102**(8): p. 087602.

98. Wu, Z., J.B. Neaton, and J.C. Grossman, *Charge Separation via Strain in Silicon Nanowires.* Nano Letters, 2009. **9**(6): p. 2418-2422.

99. Zubko, P., G. Catalan, and A.K. Tagantsev, *Flexoelectric Effect in Solids.* Annual Review of Materials Research, 2013. **43**(1): p. 387-421.

100. D., N.T., et al., *Nanoscale Flexoelectricity.* Advanced Materials, 2013. **25**(7): p. 946-974.

101. Yudin, P.V. and A.K. Tagantsev, *Fundamentals of flexoelectricity in solids.* Nanotechnology, 2013. **24**(43): p. 432001.

102. Pyatakov, A.P., et al., *Spin flexoelectricity and chiral spin structures in magnetic films.* Journal of Magnetism and Magnetic Materials, 2015. **383**: p. 255-258.

103. Yang, M.-M., D.J. Kim, and M. Alexe, *Flexo-photovoltaic effect.* Science, 2018.

104. Schiaffino, A., et al., *Metric wave approach to flexoelectricity within density functional perturbation theory.* Physical Review B, 2019. **99**(8): p. 085107.

105. Blöchl, P.E., *Projector augmented-wave method.* Physical Review B, 1994. **50**(24): p. 17953-17979.

106. Ernzerhof, M. and G.E. Scuseria, *Assessment of the Perdew–Burke–Ernzerhof exchange-correlation functional.* The Journal of Chemical Physics, 1999. **110**(11): p. 5029-5036.

107. Perdew, J.P., K. Burke, and M. Ernzerhof, *Generalized Gradient Approximation Made Simple.* Physical Review Letters, 1996. **77**(18): p. 3865-3868.

108. Kresse, G. and J. Hafner, *Ab initio molecular dynamics for open-shell transition metals.* Physical Review B, 1993. **48**(17): p. 13115-13118.

109. Kresse, G. and J. Furthmüller, *Efficient iterative schemes for ab initio total-energy calculations using a plane-wave basis set.* Physical Review B, 1996. **54**(16): p. 11169-11186.

110. Grimme, S., *Semiempirical GGA-type density functional constructed with a long-range dispersion correction.* Journal of Computational Chemistry, 2006. **27**(15): p. 1787-1799.

111. Bir, G.L. and G.E. Pikus, *Symmetry and strain-induced effects in semiconductors.* 1974.

112. Lou, P.C., et al., *Spin phonon interactions and magneto-thermal transport behavior in p-Si.* Solid State Communications, 2018. **283**: p. 37-42.

113. Avery, A.D., M.R. Pufall, and B.L. Zink, *Observation of the Planar Nernst Effect in Permalloy and Nickel Thin Films with In-Plane Thermal Gradients.* Physical Review Letters, 2012. **109**(19): p. 196602.

114. Schmid, M., et al., *Transverse Spin Seebeck Effect versus Anomalous and Planar Nernst Effects in Permalloy Thin Films.* Physical Review Letters, 2013. **111**(18): p. 187201.

115. Sheng, P., et al., *The spin Nernst effect in tungsten.* Science Advances, 2017. **3**.

116. Zhang, L. and Q. Niu, *Angular Momentum of Phonons and the Einstein--de Haas Effect.* Physical Review Letters, 2014. **112**(8): p. 085503.

117. Bose, A., et al., *Direct detection of spin Nernst effect in platinum.* Applied Physics Letters, 2018. **112**(16): p. 162401.

118. Meyer, S., et al., *Observation of the spin Nernst effect.* Nature Materials, 2017. **16**: p. 977.

119. Kim, D.-J., et al., *Observation of transverse spin Nernst magnetoresistance induced by thermal spin current in ferromagnet/non-magnet bilayers.* Nature Communications, 2017. **8**(1): p. 1400.

120. Gorini, C., U. Eckern, and R. Raimondi, *Spin Hall Effects Due to Phonon Skew Scattering.* Physical Review Letters, 2015. **115**(7).

121. Sheng, L., D.N. Sheng, and C.S. Ting, *Theory of the Phonon Hall Effect in Paramagnetic Dielectrics.* Physical Review Letters, 2006. **96**(15): p. 155901.

122. Strohm, C., G.L.J.A. Rikken, and P. Wyder, *Phenomenological Evidence for the Phonon Hall Effect.* Physical Review Letters, 2005. **95**(15): p. 155901.

123. Qin, T., J. Zhou, and J. Shi, *Berry curvature and the phonon Hall effect.* Physical Review B, 2012. **86**(10): p. 104305.

124. Lou, P.C., et al., *Spin phonon interactions and magneto-thermal transport behavior in p-Si.* Solid State Communications, 2018. **283**: p. 37-42.

125. Lou, P.C., W.P. Beyermann, and S. Kumar, *Spin mediated magneto-electro-thermal transport behavior in Ni80Fe20/MgO/p-Si thin films.* Journal of Applied Physics, 2017. **122**(12).

126. Lou, P.C., et al., *Large spin Hall effect in Si at room temperature.* Physical Review B, 2020. **101**(9).

127. Lou, P.C. and S. Kumar, *Spin-Driven Emergent Antiferromagnetism and Metal-Insulator Transition in Nanoscale p-Si.* Physica Status Solidi B-Basic Solid State Physics, 2018. **255**(4).

128. Dash, S.P., et al., *Electrical creation of spin polarization in silicon at room temperature.* Nature, 2009. **462**(7272): p. 491-494.

129. Wesenberg, D., et al., *Relation of planar Hall and planar Nernst effects in thin film permalloy.* Journal of Physics D: Applied Physics, 2018. **51**(24): p. 244005.

130. Madon, B., et al., *Anomalous and planar Righi-Leduc effects in Ni80Fe20 ferromagnets.* Physical Review B, 2016. **94**(14): p. 144423.

131. Avery, A.D., M.R. Pufall, and B.L. Zink, *Observation of the planar Nernst effect in permalloy and nickel thin films with in-plane thermal gradients.* Phys Rev Lett, 2012. **109**(19): p. 196602.

132. Avery, A.D., M.R. Pufall, and B.L. Zink, *Determining the planar Nernst effect from magnetic-field-dependent thermopower and resistance in nickel and permalloy thin films.* Physical Review B, 2012. **86**(18).

133. Miao, B.F., et al., *Inverse Spin Hall Effect in a Ferromagnetic Metal.* Physical Review Letters, 2013. **111**(6).

134. Tsukahara, A., et al., *Self-induced inverse spin Hall effect in permalloy at room temperature.* Physical Review B, 2014. **89**(23).

135. Anwar, M.S., B. Lacoste, and J. Aarts, *Anisotropic magnetothermoelectric power of ferromagnetic thin films.* Journal of Magnetism and Magnetic Materials, 2017. **441**: p. 542-547.

136. Salleh, F., et al., *Seebeck Coefficient of Ultrathin Silicon-on-Insulator Layers.* Applied Physics Express, 2009. **2**(7).

137. Zhang, X.O., et al., *Thermal Hall Effect Induced by Magnon-Phonon Interactions.* Physical Review Letters, 2019. **123**(16).

138. Zhu, H.Y., et al., *Observation of chiral phonons.* Science, 2018. **359**(6375): p. 579-581.

139. Ishizuka, H. and N. Nagaosa, *Spin chirality induced skew scattering and anomalous Hall effect in chiral magnets.* Science Advances, 2018. **4**(2).

140. Yang, A.C., et al., *Rashba spin-orbit coupling enhanced anomalous Hall effect in MnxSi1-x/SiO2/Si p-i-n junctions.* Rsc Advances, 2016. **6**(61): p. 55930-55935.

141. Cho, C.-H., R.C. Jaeger, and J.C. Suhling, *Characterization of the Temperature Dependence of the Piezoresistive Coefficients of Silicon From ${-} 150\,^{\circ} $ C to ${+} 125\,^{\circ} $ C.* IEEE Sensors Journal, 2008. **8**(8): p. 1455-1468.

142. Kanda, Y., *A graphical representation of the piezoresistance coefficients in silicon.* IEEE Transactions on electron devices, 1982. **29**(1): p. 64-70.

143. Smith, C.S., *Piezoresistance effect in germanium and silicon.* Physical review, 1954. **94**(1): p. 42.

144. Asheghi, M., et al., *Thermal conduction in doped single-crystal silicon films.* Journal of applied physics, 2002. **91**(8): p. 5079-5088.

145. Avery, A.D., et al., *Thermal and electrical conductivity of approximately 100-nm permalloy, Ni, Co, Al, and Cu films and examination of the Wiedemann-Franz Law.* Physical Review B, 2015. **92**(21).

146. Lou, P.C. and S. Kumar, *Generation and detection of dissipationless spin current in a MgO/Si bilayer.* Journal of Physics-Condensed Matter, 2018. **30**(14).

147. Ruckriegel, A. and R.A. Duine, *Long-Range Phonon Spin Transport in Ferromagnet-Nonmagnetic Insulator Heterostructures.* Physical Review Letters, 2020. **124**(11).

148. Zhang, X., et al., *Hidden spin polarization in inversion-symmetric bulk crystals.* Nat Phys, 2014. **10**(5): p. 387-393.

149. Riley, J.M., et al., *Direct observation of spin-polarized bulk bands in an inversion-symmetric semiconductor.* Nat Phys, 2014. **10**(11): p. 835-839.

150. Yuan, L., et al., *Uncovering and tailoring hidden Rashba spin–orbit splitting in centrosymmetric crystals.* Nature Communications, 2019. **10**(1): p. 906.

151. Lou, P.C., et al., *Large spin Hall effect in Si at room temperature.* Physical Review B, 2020. **101**(9): p. 094435.

152. Wang, L., et al., *Flexoelectronics of centrosymmetric semiconductors*. Nature Nanotechnology, 2020.

153. Tokura, Y. and N. Nagaosa, *Nonreciprocal responses from non-centrosymmetric quantum materials.* Nature Communications, 2018. **9**(1): p. 3740.